Spring 2016

Cable shovel dipper stress and fatigue failure modeling in formation excavation engineering

Muhammad Azeem Raza

Department: Mining and Nuclear Engineering

CABLE SHOVEL DIPPER STRESS AND FATIGUE FAILURE MODELING IN FORMATION EXCAVATION ENGINEERING

by

MUHAMMAD AZEEM RAZA

A DISSERTATION

Presented to the Faculty of the Graduate School of the

MISSOURI UNIVERSITY OF SCIENCE AND TECHNOLOGY

In Partial Fulfillment of the Requirements for the Degree

DOCTOR OF PHILOSOPHY

in

MINING ENGINEERING

2016

Approved by:

Samuel Frimpong, Advisor

Kwame Awuah-Offei

K . Chandrashekhara

Grzegorz Galecki

Maochen Ge

ABSTRACT

Large capacity shovels are used to achieve economic bulk production in surface mining operations. The suspended payload combined with dipper weight and formation resistive forces results in severe stress loading of the shovel front-end assembly. Material flaws, high stresses and harsh excavation conditions can initiate cracks in the dipper-teeth assembly. High stresses can cause these cracks to propagate to critical lengths resulting in fatigue failure, unscheduled downtimes, costly unplanned repairs, and downstream processing circuit problems. The literature reveals that dipper-related problems significantly reduce shovel up-time. This research is a pioneering effort towards developing a solid frame work for stress profiling, and fatigue fracture failure modeling of the shovel dipper-teeth assembly.

Kinematic and dynamic models of the shovel front-end assembly have been built using the Newton-Euler iterative algorithm and incorporate the dynamic formation resistive and payload forces. A numerical simulator is designed to solve these models. A virtual P&H 4100XPC shovel prototype is built in ANSYS (R15) software for stress and fatigue failure modeling studies. It is found that maximum stress varies cubically with formation density and linearly with cutting resistance. The maximum von-Misses stress on the dipper of 282 MPa exceeds the lower limits of the yield stresses for low, medium and high carbon steels. Crack propagation simulation studies show that a 100 mm crack-length is the critical crack-length for the dipper-teeth assembly. A 75 mm bottom-plate crack can propagate to the critical length in 16 days. This new knowledge provides the basis for new shovel dipper designs for different applications in surface mining operations.

ACKNOWLEDGMENTS

I am greatly thankful to my research advisor, Dr. Samuel Frimpong, for his patience, continuous support and guidance, and encouragement throughout my PhD studies which made this dissertation possible. I feel lucky to have an advisor who cares for his students and provides plenty of opportunities to learn and grow. I am greatly thankful to my committee members, Drs. Kwame Awuah-Offei, K. Chandrashekhara, Grzegorz Galecki, and Maochen Ge, for their feedback and support.

I am thankful to Dr. Saima Ghazal, my loving and caring wife, who supported me throughout my journey. She is an amazing lady who completed her PhD studies alongside me, without compromising her family duties. I am thankful to my two lovely kids, Adil and Ashar, who watched me work patiently and gave me the joy of life with their innocent talks.

I am grateful to the friendly staff members of the Department of Mining and Nuclear Engineering who provide a home-like environment for the international students. I am thankful to Mr. Scott Hamilton (IT Research Support) who helped me set-up on high performance cluster to run my simulations.

I am thankful to the University of Engineering & Technology, Lahore, Pakistan, the Higher Education Commission of Pakistan, and the Department of Mining and Nuclear Engineering of Missouri S&T for providing me funding for the PhD studies.

TABLE OF CONTENTS

Page

LIST OF ILLUSTRATIONS

Page

LIST OF TABLES

Page

NOMENCLATURE

Symbol	Description
τ	Shear strength
c	Cohesion
φ	Internal friction angle of the soil
C	Material constant for Paris Law
C_a	Coefficient of adhesion between soil and tool
C_o	The number of impacts required to sink a cylindrical tip in a standardized test by 10 cm.
ρ	The angle that the rupture surface makes with the horizontal
s	Thickness of side plate of bucket
V, μ	Coefficients dependent upon the cutting conditions for (Zelenin et al., 1985) model
β	Constant inclination of dipper from crowd-arm
β'	Tool cutting angle for Zelenin model
q	Surcharge pressure acting vertically on soil surface
d	Tool working depth
w	Width of tool
γ	Bulk density
N_γ', N_c', N_q'	N-Coefficients for Terzaghi's model. Valued depend upon the internal friction angle (φ)
$N\gamma$, Nc, N_a, N_{ca}, N_q	N-factors in the Universal Earthmoving Equation
z	Coefficient for teeth configuration in the Zelenin model

Q_u	Ultimate bearing capacity of rock, as defined in Terzaghi's Equation
B	Width of foundation
FEM	Finite element modeling
DEM	Discrete or distinct element modeling
μ_1	Coefficient of friction between material and bucket
N'	Normal force
ε	Coefficient of resistance to filling of the bucket and movement of the drag prism of soil
q_n	Ratio of the volume of the drag prism ahead of bucket to the volume of the bucket
B_v	Volume of bucket
k_n	Ratio of the volume of the drag prism ahead of bucket to the volume of the bucket
k	Specific cutting resistance of soil
k_{ep}	Coefficient of earth pressure at-rest
P_1	Cutting resistance of the blade
P_2	Additional resistance due to wear of the edge
P_3	Resistance offered by the two sides
P_4	(Resistance due to friction of the sides
K_{comp}	Specific resistance of the given stratum to longitudinal compression, (N/cm^2)
F	Stratum cross-section (w*d)
g	Gravitational acceleration (m/sec^2)
q_1	Volume of drag prism (m^3)
γ	Density of soil (kg/m^3)

f_1	Force required to overcome the weight of the loaded material in and above the bucket.
f_2	Resultant of forces of resistance for material moving towards the bucket.
f_3	Force due to the friction between the bucket walls and the soil material sliding into the bucket.
f_4	Resistance to cutting and/or penetration acting at the tip of the bucket and side walls.
f_5	Inertia force of the material inside and above the bucket.
f_6	Force required to move the empty bucket (modeled as part of f_1)
A	Cross-sectional area swept by the dipper up to failure plane
α	Bench face angle (for area and force f_1 calculations)
f(x)	Function defining the failure plain (curve)
w	Dipper width
d	Depth of tool (dipper) into the bench
da/dN	Crack growth rate per cycle as defined by Paris Law
a	Crack length
N_f	Number of cycles to failure
K	Stress intensity factor
m	Material constant for Paris Law
σ	Remote stress
σ_{ij}	Stress distribution near crack tip (stress tensor)
ϵ_{ij}	Strain tensor
(r,ϕ)	Polar coordinate system parameters
f(g) or f_{ig}	Correction factor depending upon the material and crack geometry

a_i, a_f	Initial and final/critical known/assumed crack length
$C(\Theta,\dot{\theta})$	Generalized Coriolis and centripetal torque
$D(\Theta)$	Generalized inertia matrix
$G(\Theta)$	Generalized gravity torque
m_1, m_2	Mass of crowd-arm and dipper, respectively
β	Constant inclination of link 3 from link 2 (inclination of X_4 from X_3)
θ_e	Inclination of coordinate frame {4′} from coordinate frame 3.
l_1	Length of crowd-arm from pivotal point to connection point between arm and dipper
l_2	Length between dipper tip and connect point of arm and dipper
s_i, c_i	$\sin\theta_i$ and $\cos\theta_i$, respectively
di	Offset distance of the gravity center in link i
I_{zz} , I_{zz2}	Moment of inertias of crowd-arm & dipper
F_n, F_t	Normal & tangential cutting resistive forces on dipper tip
F'	Cable shovel breakout force
$F_{load}(F_n, F_t)$	Formation resistive forces
${}^{i+1}T_i$	Transformation matrix to transfer the coordinates from i to i+1
${}^{i+1}R_i$	Rotational matrix, extracted from ${}^{i+1}T_i$
c_i, s_i	$\cos(\theta_i)$, and $\sin(\theta_i)$
$[K_i]$	Stiffness-matrix at i^{th} iteration
$[F^{app}]$	Vector of applied loads
$[u_i]$	Displacement vector at i^{th} iteration
$[\Delta u]$	Displacement difference
T	Traction vector

1. INTRODUCTION

Material excavation is a primary activity in the mining industry and shovel excavators are primary production equipment in surface mining operations. Cable shovels are the preferred equipment for excavating larger production capacities economically over its economic life. The capital investment in cable shovels can be as high as $25 million. The overall efficiency of truck-shovel surface mining operations is largely dependent on shovel efficiency. The active population of cable shovels is about 2400 units around the world out of which 1700 are 20 mt or larger capacity (parkerbaymining.com). Joy Global (P&H), Caterpillar (formerly under Bucyrus) and OMZ (OOO IZ-KARTEX) are the largest electric shovel original equipment manufacturers (OEM) around the world. The excavating capacities of the shovels have seen an increasing trend over the years. The increase in size brings in a whole lot of different challenges related to shovel stress modeling and life estimation. This research is conducted to address some of the challenges associated with the stress and fatigue failure of cable shovel dipper-teeth assembly. This section gives the background of this research identifying the problem and its importance and impact on shovel operating practice and efficiency. It covers the problem statement, objectives and scope of the study and research methods utilized to address the problem. The expected scientific and industrial contributions are also listed, as well as the structure of the dissertation report.

1.1. BACKGROUND OF RESEARCH PROBLEM

There is a trend in the mining industry towards excavating and loading more tons per scoop to achieve the economies of scale and reduce the unit cost associated with

excavation and haulage. The electric shovel saw the biggest jump as the capacity improved from 5yd^3 in 1960 to 44+ yd^3 today. Modern day mining cable shovels have payload capacities of 100+ tons per scoop (Caterpillar, 2012; P&H Mining, 2011). The excavation of 100+ tons per scoop, combined with the weight of the dipper, and diggability variation of the formation result in varying mechanical energy inputs and stress loading of the boom and dipper-and-tooth assembly across working bench. Furthermore, the repeated loading and unloading cycles of the shovel induce fatigue stresses in shovel components. The induced stresses over time may exceed the yield strength of steel/material of the shovel leading to fatigue failure, teeth losses, and boom and handle cracks. Stress development and fatigue failure in shovel front-end assembly cause unplanned downtimes resulting in reduced efficiency and increased production costs.

Haulage cost is an important and significant cost center in surface mining operations. At Syncrude's Aurora mine the excavation and haulage cost constitute about 40% of the total costs with excavation comprising 14% of this percentage (Syncrude, 1996). Haulage cost probably provides the biggest potential to reduce the costs as well. Dipper and teeth assembly is a critical component of the cable-shovel.

Majority of the shovel downtime is dipper related. Roy et al. (2001) reported the dipper related problems to be the second largest contributor towards shovel breakdown time as shown in Figure 1.1. The data also show that dipper related breakdowns were the most frequent among all the breakdowns as shown in Figure 1.2. These frequent breakdowns result in increased shovel downtime, reduced efficiency, higher repair costs, and increased production costs.

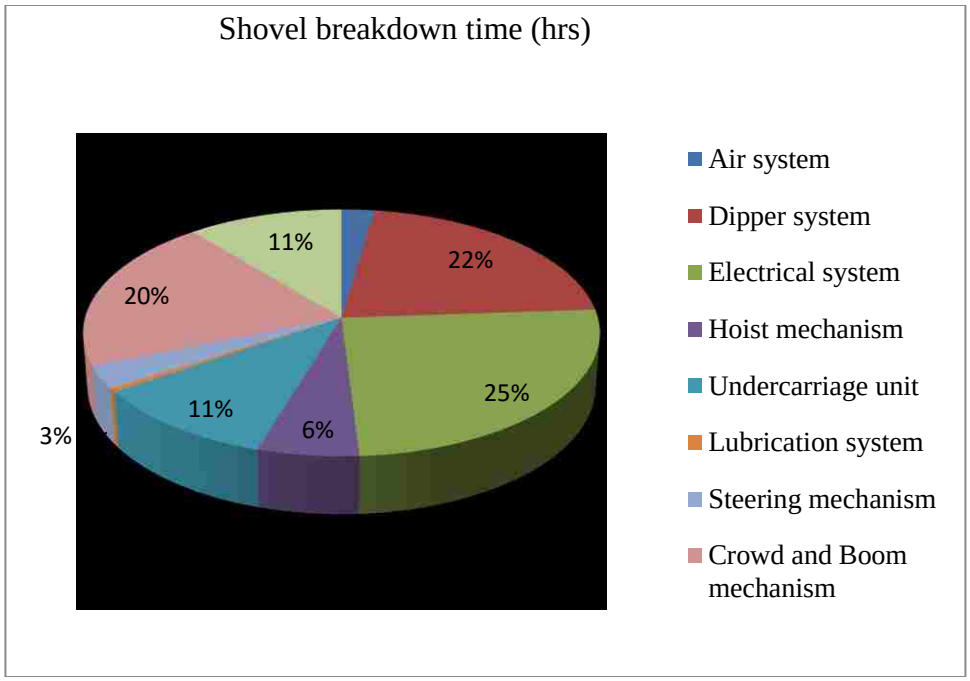

Figure 1.1. Percentage of shovel breakdown time

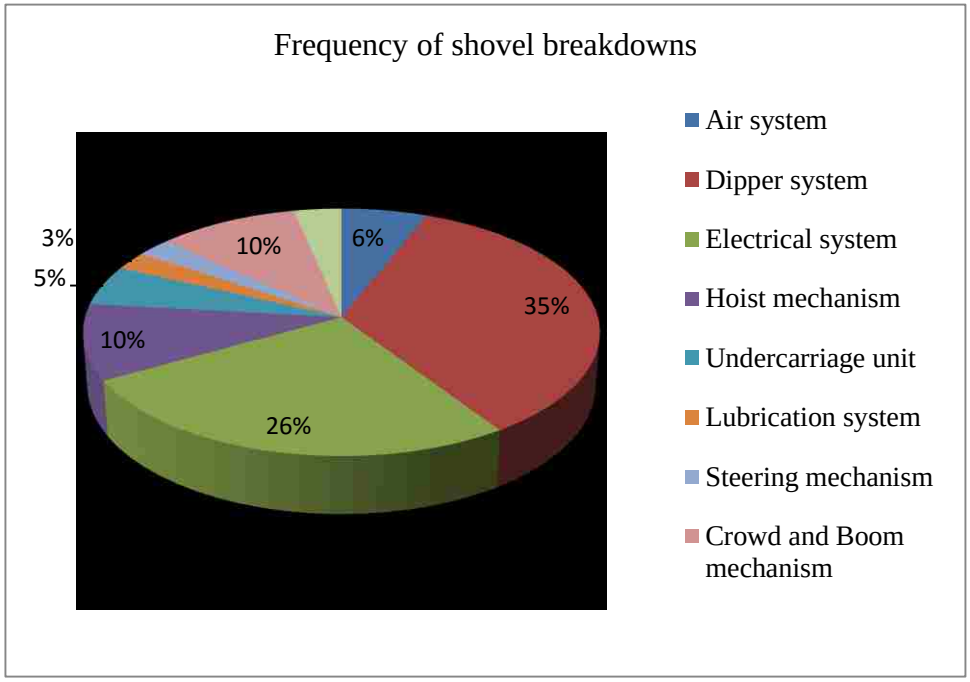

Figure 1.2. Frequency of shovel breakdowns

The current practice for the shovel front-end assembly repair is generally experience and history based rather than science based. This leads to frequent and costly shovel breakdowns. A dynamic model that can incorporate the dynamic forces on the dipper-teeth assembly is essentially required to estimate the true nature of stresses on dipper front-end assembly. This research is a pioneering effort towards reliability studies of the shovel front-end assembly incorporating the dynamic forces during the excavation.

This research is an attempt towards understanding the failure mechanism and a quantitative assessment of the fatigue life of the shovel dipper to overcome the shovel excavation challenges.

1.2. CABLE SHOVEL NOMENCLATURE

Figure 1.3 illustrates a schematic view of a cable shovel. A cable shovel consists of three major mechanisms: - the lower, upper and the front-end assembly. The lower assembly consists of the propel drive and crawler systems and provides a solid and stable base for the excavator. This helps excavator propel, positioning and relocation during its operation. The shovel's upper assembly is a roller and center-pin system mounted on the lower mechanism. The upper assembly consists of multiple decks with housing for the hoist and swing machinery and electronic control cabinet on the lower deck; and the operator's cab on the upper deck. Additionally the upper assembly provides a platform boom attachment and the counter weight for the dipper. The front-end consists of the boom, crowd machinery, dipper-handle, dipper and ropes.

The primary motions of a cable shovel include propel, swing, hoist and crowd/retract. The shovel uses the propel function to tram from one digging site to another and to position itself against the face. Shovel swing motion, between excavation

face and haulage equipment, is controlled through multiple swing gears, pinions and electric circuits. Dipper, dipper teeth, crowd-arm and ropes are the important components of shovel front-end assembly. In this study only the dipper-teeth assembly is considered as only these engage directly with the formation.

1.3. OBJECTIVES AND SCOPE OF STUDY

The primary objective of this research is to provide knowledge that can help extend the economic life of cable shovel's dipper-teeth assembly with corresponding reductions in maintenance costs associated with the dipper components. This objective is achieved by modeling the stress profile and estimating the life of fatigue cracks on the dipper-teeth assembly during formation excavation. The elements of this primary objective include the following:

- Formulate appropriate kinematic model for shovel front-end assembly
- Formulate appropriate dynamic formation resistive-force models for the shovel dipper, establishing their point of application, and formulation of dynamic models of the shovel dipper-teeth assembly
- Develop numerical simulation model for solving the dynamic model
- Develop virtual prototype simulation for shovel dipper for stress analysis
- Model the fatigue life expectancy of dipper-teeth assembly at high stressed regions of the dipper

During the digging operation, only the dipper moves through the muck pile and no shovel swing and propel motions are involved. This research, therefore, is restricted to the dynamic modeling and simulation of the digging operation of the shovel digging cycle only. The dipper stress profile and fracture life estimation is performed by creating

a virtual prototype of shovel dipper-teeth assembly in ANSYS R15 software environments. No direct and extensive field testing is done for this research.

1.4. RESEARCH METHODOLOGY

The research started with a detailed and critical evaluation of the literature establishing the current research frontier in shovel excavation and fatigue failure studies. The survey also established the suitability and selection of the resistive force models for cable shovel excavator; and provided a base for developing the cable shovel dynamic model. The resistive force model as proposed by Hemami (1994) is selected for this research. Suitable kinematic and dynamic models for cable shovel front end assembly are developed for capturing 2D motions. A numerical simulation model is created in MATLAB and SIMULINK to solve the dynamic models. The model uses shovel dimensions and material characteristics as inputs and computes dynamic resistive forces, crowd force, and torque as the shovel dipper moves through the bank.

A virtual prototype for P&H 4100 XPC is created in ANSYS workbench R(15) for stress and fatigue analysis using numerical simulations. ANSYS has computationally efficient routines for finite element based stress computations. The stresses are compared with the material properties of shovel to indicate the critical stress points for failure against yield strength. The model also establishes the basis for fatigue failure and life-expectancy analysis of shovel dipper-teeth assembly. Pre-defined semi-elliptical cracks are introduced in the simulation process at selected locations. The fracture mechanics approach is used to estimate the stress intensity factors (SIFs) at the tip of these cracks. SIF vs crack length relationships are established for the cracks. These relationships are used to generate the crack-propagation curves and to estimate the life of dipper

components. Simulation experiments are analyzed to draw conclusions and the necessary recommendations.

1.5. STATEMENT OF THE PROBLEM

Material excavation is a primary activity in surface mining operations and constitutes a significant cost component. Current shovels are equipped with dippers with capacities exceeding 100 tons pay loads. During a normal excavation duty cycle, the teeth and front lip engage directly with the formation and experience the dynamic resistive, impact, and fatigue forces, whereas the dipper experiences the dynamic weight forces and the impact forces. These forces result in tooth-loss and failures which may be attributed due to crack initiation and propagation. These forces can no longer be ignored because of the size of the dipper and quantity of material excavated. The diggability variation of the formation is another important contributor to the severe stress loading of the shovel components, especially the dippers (Frimpong and Hu, 2008).

Roy et al. (2001) found dipper related downtimes of the shovel to be the second largest, in terms of downtime hours, and most frequent amongst all the shovel related downtimes (Figure 1.2 and Figure 1.1). Knights (2009) reported a teeth set interval time of four days at the Morenci Mine, costing around US$3,000 per set replacement. The cost of unplanned change-out of tooth set was estimated at US$41,368 during the study period of approximately a year. Pearson et al. (2004) reported the sudden breaking down of the boom of a large barge mounted hydraulic excavator due to fatigue cracks reaching the critical length.

Many times the broken teeth of the excavator end-up in the crushers resulting in crusher breakdown and increased repair costs. Understanding and estimating the stresses

on teeth and dipper assembly is, therefore, very critical towards estimating the economic life of these components and avoid the costly downtimes and related problems. This knowledge of shovel stress profiles and fatigue resulting in crack initiation and propagation will allow operators to design drill-blast systems to ensure good fragmentation and reduce severe dipper stresses and fatigue.

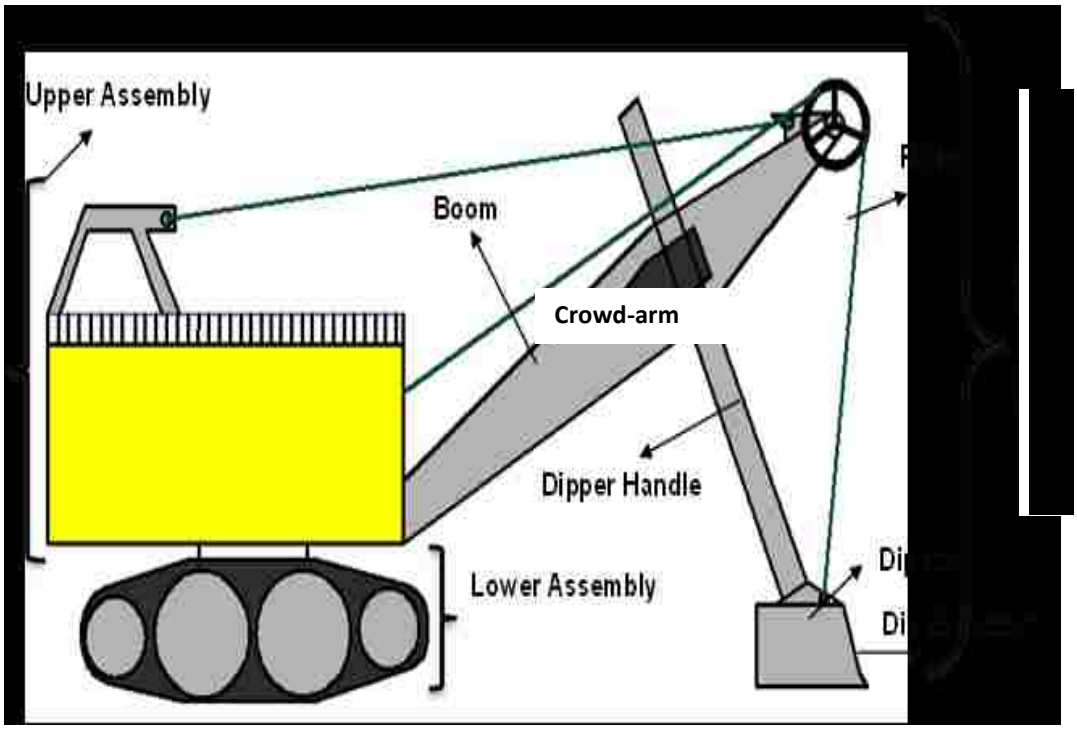

Figure 1.3. Nomenclature of a cable shovel

1.6. SCIENTIFIC AND INDUSTRIAL CONTRIBUTIONS

This research contributes to the existing body of knowledge on health and longevity of the cable shovel dipper-teeth assembly. The research is expected to advance shovel reliability, maintainability, and availability, which will influence surface mining

productivity. It is expected that the research will help formulate mathematical models for improved efficiency and lower maintenance costs for the cable shovel operations.

This research is a pioneering effort for developing the cable shovel dipper stress analysis incorporating the dynamic resistive and payload forces. Previous research attempts generally ignored the dynamic forces due to the weight of the dipper and payload. Given the size of current large-scale shovels (+100 tons per pass) these forces can no longer be ignored. The models created in this research give a detailed force and torque information for various joints and links of the shovel front-end.

This research is also the first attempt to model the fatigue life of the shovel dipper-teeth assembly. Research shows that dipper related break downs are among the highest for shovel excavation down times (Roy et al., 2001). The current practice for the shovel front end repair is experienced-based rather than-scientifically based. This research is expected to lay a foundation of the scientific understanding for the shovel dipper-teeth stress and fatigue failure studies. The life expectancy of the shovel components should help reduce the operating costs of the shovel excavation. The models are expected to help in the production of the next generation of shovel dippers for the surface mining industry.

1.7. STRUCTURE OF THE DISSERTATION

The dissertation is organized into eight sections for ease of comprehension and relevancy. Section 1 gives the background and problem statement for this research, along with the expected scientific and industrial contributions. Section 2 contains a critical review of the literature relevant to this research. The section is three fold with sub-sections on formation resistive forces, kinematic and dynamic modeling aspects, and fatigue fracture mechanics literature relevant to this research. Section 3 discusses the

modeling philosophy to carry out this research. Section 4 details the step-by-step dynamic mathematical modeling done for the shovel front-end. Numerical simulator details of the kinematic and dynamic model, and virtual prototype simulation details are discussed in Section 5. Section 6 gives a detailed discussion on experimental design and experimentation conducted for this research. Section 7 contains the analysis and discussions of the results. Section 8 discusses the necessary conclusions drawn out of this research and gives recommendations for further work.

2. LITERATURE REVIEW

This section includes a comprehensive review of the literature that focuses on shovel formation interaction modeling, stress modeling, and fatigue failure modeling. The review is three-fold addressing three important topics: resistive forces on the shovel, both the kinematic and the dynamic modeling of the shovel, and fatigue failure modeling of the shovel's components. The symbols, signs, and abbreviation used in this section are defined in the nomenclature section.

2.1. SHOVEL RESISTANCE FORCES AND MODELING

Excavation processes conducted with a tool can be categorized as penetration, cutting, and scooping processes (Blouin et al., 2001; Lipsett and Moghaddam, 2011). In general, penetration is the insertion of a tool into a medium, and cutting is the lateral movement of a tool, typically conducted at a constant depth. Resistive force and soil failure theories date back to the studies conducted by Coulomb (1776) and Mohr (1914) that result into simpler mathematical formulation for shear failure of soil. Significant developments occurred in soil failure theories during the nineteenth century, particularly those relating to soil cutting tools, and 2D and 3D failure models were developed using empirical and numerical techniques.

Soil-tool interactions and resistive forces each depend on a number of tool, soil and operating parameters. Hemami and Hassani (2003) listed 32 parameters related to tools, mediums, operations, environments, and tool-medium interactions, that various researchers included in the cutting and excavation models. In that research the high frequency tool parameter was the tool width (w), while high frequency soil parameters

included cohesion (c), angle of internal friction (φ) and bulk density (γ); and high frequency operating parameters included cutting angle (α), tool velocity (v), depth of cut (d), and surcharge (q) (Blouin et al., 2001). The basic assumptions in nearly all of the models include homogeneity, continuity, and isotropy of the medium in front of the tool (Balovnev, 1983; McKyes, 1985; Thakur and Godwin, 1990; Zelenin et al., 1985). In general the variation in homogeneity and continuity is low in mined rocks and therefore, blasted or fragmented rock (as found in many mining operations) can be considered as a homogeneous and continuous material when excavated with narrow tools (Fowkes et al., 1973).

Terzaghi (1943) presented a theory for the bearing capacities of soils in shallow foundations. This theory is based on passive earth pressure theory (equation (2.1)). The model is important as it provided a basis for the universal earthmoving equation (UEE).

$$Q_u = 0.5\ \gamma\ B\ N_\gamma' + c\ N_c' + q\ N_q' \qquad (2.1)$$

Values of the N-coefficients N_γ', N_c', N_q' are functions of the angle of internal friction.

Osman (1964) and Reece (1965) based their excavation models (upon realizing the similarities between the two) on Terzaghi's (1943) bearing capacity model. Reece (1965) first introduced the fundamental equation for earthmoving, or UEE as equation (2.2).

$$P = \left(\gamma g d^2 N_\gamma + c d N_c + q d N_q + C_a d N_{ca}\right) w \qquad (2.2)$$

The most complete form of the UEE is summarized by McKyes (1985) and is given as equation (2.3).

$$P = \left(\gamma g d^2 N_\gamma + c d N_c + C_a d N_{ca} + q d N_q + \gamma v^2 d N_a\right) w \qquad (2.3)$$

Here a dynamic term is used to account for speed of the tool. The N-factors are dependent on the soil's properties, tool's geometry, and the tool-soil's interface. These factors can be determined analytically for simple cases.

The 2-D models, equations (2.1) to (2.3), are either based on passive earth pressure theory or limit equilibrium techniques. These models assume an instantaneous failure, which is true for most plastic soils. A soil's failure (e.g. cohesive soils) can be progressive failure as well. Yong and Hana (1977) applied finite element modeling (FEM) techniques to analyze the soil cutting for the progressive failure of soil at the tool tip. This model is a 2-D model that uses plane strain conditions. The experimental results closely matched the predicted results under the experimental conditions.

The FEM techniques assume the material as a continuum. In contrast, soil and fragmented rocks are discontinuous medium and undergo larger displacements at pre-defined planes. Cundall and Strack (1979) introduced a discrete, or distinct element model (DEM) to analyze discrete particle assemblies. This DEM assumes that the medium is an assembly of discrete particles connected through a spring to represent the medium's elastic/in-elastic properties. The DEM has been used to model soil cutting by different tools and in different cutting conditions (Mak et al., 2012; Momozu et al., 2003; Oida and Momozu, 2002; Tanaka et al., 2000; Ting et al., 1989). The DEM analyses are typically limited to small scale studies. The actual soil cutting process consists of billions of particles that require large computational resources for real simulation experiments. The particles and contacts are generally simpler while the actual grain geometries and contacts are complex. Digging with a cable shovel dipper is 3D in nature. The side plates also take part in excavation. There exist few three-dimensional extensions of two-dimensional soil cutting models (Boccafogli et al., 1992; McKyes, 1985; Swick and Perumpral, 1988).

2.2. FORMATION RESISTIVE FORCES

A cable shovel dipper has teeth at its front end that serve as the cutting tools; the teeth penetrate the formation/muckpile, and the lip is the actual cutting tool. The excavation process is a combination of penetration, cutting, and scooping (bucket filling). When cutting by a blade, the cutting force is typically decomposed into its orthogonal components: - the tangential and normal. The tangential force component acts along the blade surface and the normal force acts perpendicular to the blade surface. For excavation with a dipper, dipper-teeth, lip, and side plates all take part in the digging process and these all experience soil's resistance acting on these components. Excavation models are based on these resistive forces offered by soil on the cutting tool. The resistive forces that act on a shovel's dipper during the digging operation are a combination of cutting forces at a dipper's teeth and lip and the excavation forces due to material movement along, ahead, and inside the dipper. The forces acting on a dipper (or a bucket-type) excavator are complex in nature and thus are difficult to model. Both the experimental and analytical models are built to model these resistive forces.

Dombrovskii and Pankratov (1961) proposed that the tangential force to the digging of soil (P) is the sum of three component forces: a soil's resistance to cutting, the tool's frictional resistance with soil, resistance to movement of the drag prism ahead of the tool, and the soil movement inside the bucket (Alekseeva et al., 1985) given in equation (2.4).

They proposed an additional simplified model as given in equation (2.5). Here, k_1, unlike k, includes not only cutting but all other resistances. The values for k and k_1 were calculated experimentally for different types of soil.

$$P = \mu_1 N' + \varepsilon(1 + q_n) B_v k_n + kwd \qquad (2.4)$$

$$P = k_1 wd \tag{2.5}$$

Balovnev (1983) extended the UEE and the passive earth pressure theory to model the forces on a bucket by dividing the forces into its individual constitutive components (side walls, front blade, back of bucket). Balovnev (1983) proposed that the total excavating effort is the sum of all of the forces on individual parts. The four individual forces were identified as f_1 (the blade's cutting resistance), f_2 (additional resistance due to wear of the edge), f_3 (the resistance offered by the two sides), and f_4 (the resistance due to friction of the sides).

After extensive experimentation on cutting frozon soils, Zelenin et al. (1985) created the following empirical model (equation (2.6)) for the cutting resistance (P) of unfrozen soil, with a bucket without teeth.

$$P = 10C_o d^{1.35}(1 + 2.6w)(1 + 0.0075\beta')(1 \pm s)V\mu \tag{2.6}$$

They postulated that if a bucket with teeth cuts the soil then the teeth eliminate the participation of side plates during cutting. Therefore, the cutting force for a bucket with teeth is modified as equation (2.7).

Where 'z' is the coefficient that takes into account the blade's impact on cutting force. Zelenin et al. (1985) produced a graph that can be used to calculate z values. These values are dependent upon both the 'w' and the 'd'. The information in Table 2.1 can be approximated from that graph where 'z' values were computed for d=25cm to d=50cm. The 'z' values increase as the 'd' values decrease. The coefficient 'z' is also dependent on the ratio a/b (where 'a' is the spacing between the teeth and 'b' is the width of the tooth). The multiplying factors for z based on ratio a/b are listed in Table 2.2. Zelenin et al. (1985) developed the model further for the forces that occur during the excavation

process as given in equation (2.8). In this model they divided these excavation forces into two categories: The forces due to the longitudinal compression of soil chips (R), and the forces due to movement of a drag prism ahead of the bucket (P_n).

$$P = 10C_o d^{1.35}(1 + 2.6w)(1 + 0.0075\beta')z \tag{2.7}$$

Table 2.1. Dependence of 'z' on 'd' and 'w'

Length of horizontal surface (w, meters)	0.25-0.50	0.50-0.75	0.75-1.00	1.00-1.25
Coefficient z	0.55-0.75	0.63-0.78	0.69-0.8	0.71-0.82

Zelenin et al. (1985) suggested that these forces are present for buckets with teeth for graders and draglines. They are absent, however, for a bucket that has teeth (dipper) for a cable shovel. For the bucket with teeth (dipper) the teeth disintegrate the soil in front of the bucket and there is no drag prism is present. Therefore, the total excavation force for the shovel bucket with teeth (dipper) is as given in equation (2.7). These empirical results were gathered from a large number of experiments with smaller buckets. Present day dippers are larger in size and have higher payload capacities.

Wu (1995) used Rowland (1991) resistance model to model resistive forces acting on the dragline. In this model, the forces on the dipper were divided into four components: payload weight, friction forces on the teeth, friction forces on the lip, and four frictional forces on the dipper's surfaces (outer dipper bottom, inner dipper bottom, outer surfaces

$$W = R + P_n = FK_{comp} + gq\gamma\tan\rho \tag{2.8}$$

of side plates, and inner surfaces of the side plates). The frictional forces of the bottom, inner and outer surfaces were modeled on the total payload (which increased linearly with position). The passive earth pressure theory on a wall was used to calculate the frictional forces that occur on the side plates (inner and outer). The teeth and lip forces were modeled using the model proposed by Hettiaratchi and Reece (1974). The payload weight was modeled as the maximum payload capacity of the dipper. All these forces were considered as static forces acting at the tip of the dipper.

Table 2.2. Dependence of z on a/b (Zelenin et al., 1985)

Ratio a/b	a=b	a=2b-3b	a=4b	a=5b
z	1.2	1	1.1	1.25

Hemami (1994) attempted to automate the LHD loading and proposed a model consisting of six component forces (f_1 - f_6), which must be overcome, on a dipper during excavation as shown in Figure 2.1. All of the forces, except f_6, are dynamic forces. The six forces acting on the dipper, from the initial to the end point on trajectory, identified consisted of the following:

f_1: The force required to overcome the payload weight in and above the bucket.

f_2: The resultant of resistive forces due to material movement towards the bucket.

f_3: The force due to the friction between the bucket's walls and the soil's material as it slides into the bucket.

f_4: The resistance to the cutting and/or penetrating that acts at the bucket's tip and side walls.

f_5: The material's inertia force both inside and above the bucket.

f_6: The force required to move the empty bucket (modeled as part of f_1).

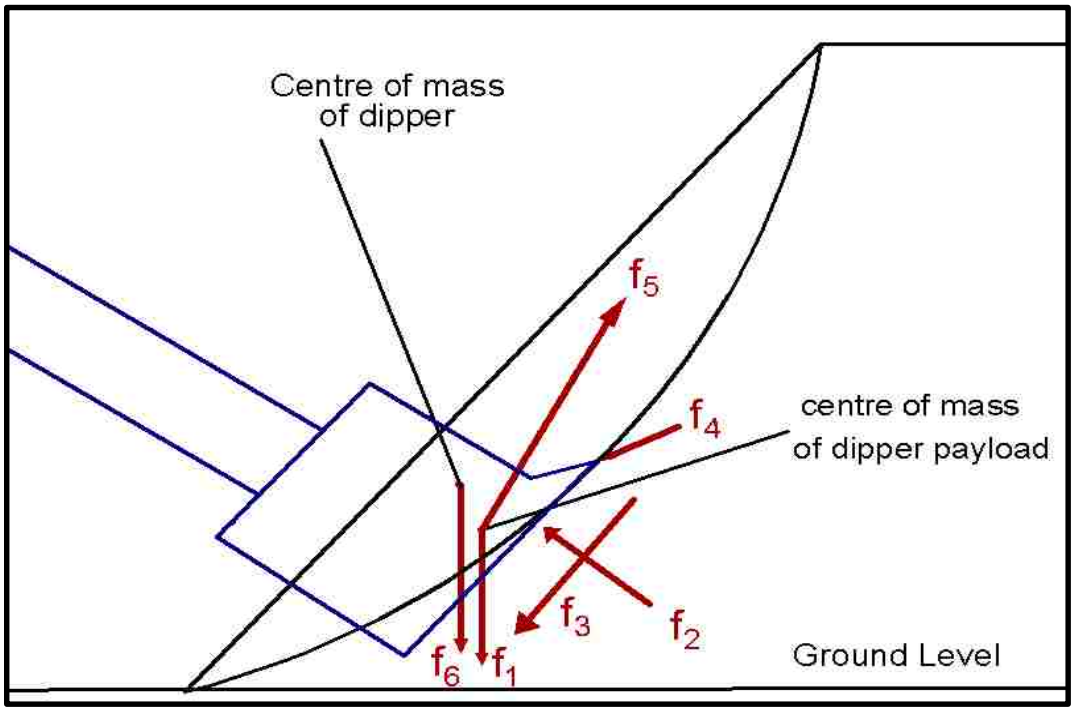

Figure 2.1. Forces on a dipper during excavation (after Hemami (1994))

Hemami (1994) defined the f_1 and f_5 as the dynamic forces, where f_1 changes both in magnitude and the point-of-application, and f_5 depends on the bucket's acceleration. Force f_6 was originally defined as a part of f_1 and f_5. It cannot be made a part of either force as the point of application is not concentric. Hemami (1994) used geometric configuration, velocity, position and orientation of the bucket to model f_1. The geometric assumptions for the calculation of the center of mass of material inside the bucket may

not be valid for the shovel dipper as the bucket considered had a triangular shape while the modern shovel dipper is more of a rectangle in shape.

Takahashi et al. (1999) used a similar description for the resistive forces (f_1 - f_5) on the bucket of an LHD. Force f_6 was ignored because it was modeled as part of f_1. The forces f_1 and f_3 were calculated geometrically using the bucket orientation and soil properties. Force f_4 was calculated by solving the force balance equations using the static earth pressure on the "soil" particles. A small-scale model was used to compare the experimental results with the calculated forces. The model, however, was not tested either with the larger buckets or at higher penetration rates.

Awuah-Offei et al. (2009) proposed a model based on the Balovnev (1983) excavation model using the same six forces as proposed by Hemami (1994). The researchers modeled the forces f_1 as a dynamic force and is given as equation (2.9).

The cross-sectional area (A) was calculated as in equation (2.10).

Where x_0, y_0 are the initial co-ordinates of the dipper tip when it comes in contact with the material, and 'x_t' is the X co-ordinate after a time 't'. The integral in the equation (2.10) defines the area under the trajectory curve and is numerically calculated once the points on the trajectory of the curve are known. Force f_2 was set to zero based on geometric considerations proposed by Hemami (1994). Forces f_3 and f_4 were modeled using Balovnev (1983) model based on the passive earth pressure theory. A numerical model was created to calculate the forces on the dipper as it moved through the muck pile. The model, however, did not calculate the forces for the individual shovel joints and links. These forces are important to compute for the strength, yield, and fatigue behavior modeling of the shovel components.

$$A = \frac{1}{2}(x_t - x_0)^2 \tan\alpha - \int_{x_0}^{x_t} f(x)dx \quad (2.10)$$

$$f_1 = A\omega\rho g \quad (2.11)$$

This model proposed by Hemami (1994) is by far the most comprehensive model for shovel excavation resistive forces. Out of the six forces in the mode, two (f_2 and f_5) can be set to zero by selecting a proper bench geometry and moving the dipper with a constant speed through the face. The three important component forces of this model are the dipper payload (f_1), dipper self-weight (f_6), and cutting forces (f_3). The dipper payload force (f_1) is the dominant force for the large capacity dippers (Awuah-Offei et al., (2009), Hemami, 1994), Takahasi et al., (1999)).

2.3. KINEMATIC AND DYNAMIC MODELING OF SHOVEL

Early studies that focused on excavator's mechanics were primarily qualitative. One of the early studies on the excavator kinematics, automatic or semiautomatic backhoe, is described in Seward et al. (1988). In that study both forward and reverse kinematic relations were developed between the joint angles and the dipper position. This work was based on the geometric relationships that exist between the different links.

Koivo (1989) described the principles and strategies related to both the kinematic and dynamic design of robotic manipulators. He later, used the Denavit-Hartenberg notation (Denavit and Hartenberg, 1955) to present a detailed kinematic model for backhoe excavator. Koivo (1994) provided a detailed description of the scheme needed for both the coordinate frame assignment and the estimation of structural kinematic parameters. Newton-Euler formulations were used to develop the forward and reverse kinematic equations for the backhoe.

Vaha and Skibniewsky (1993) used Newton-Euler equations of motion to produce a dynamic model of the excavator. They preferred the Newton-Euler motion equations over the Lagrange energy equations because the former offers a computational ease (for being recursive in nature) and efficiency. This dynamic model did not, however, consider the external resistive forces that are a very important aspect to model the complete dynamics of an excavator.

Koivo et al. (1996) extended the earlier work done by Koivo (1994) and presented a dynamic model for the excavators (backhoe). This model used Newton-Euler recursive techniques to present a detailed kinematic and dynamic equations for the backhoe. Simulation studies completed in C-language programming environment were used to compute the desired trajectories. The resistive forces developed based on Alekseeva et al. (1985) were also included in the study.

Hendricks et al. (1993) used Lagrangian formulations to develop a kinematic model, a dynamic model, and a simulator of the cable shovel to improve the shovel's productivity. The researchers didn't include the formation resistive forces. Daneshmend et al. (1993) later applied the iterative Newton-Euler formulation to the same kinetic model and developed a dynamic model. This later approach is considered better because it is iterative and is easier for computer implementation. This work, however, did not include the crowd action of the shovel's arm, which is very important for a complete description of the dynamic behavior of the cable shovel. Also, this work didn't include any model predictions.

Wu (1995) used Newton-Euler equations to develop a five-link full-body dynamic model of the cable shovel. He used a resistive force model of Rowland (1991) (developed

for dragline bucket filling) as the forces on the cable shovel dipper. The forces were assumed to be acting at the tip of the dipper as well.

Frimpong et al. (2005) used the Newton-Euler method to build a dynamic model of the cable shovel front-end assembly for shovel-formation interaction studies as given in equations (2.11). The formation resistive and breakout forces were based on the Zelenin et al. (1985) model. The breakout forces were considered to be acting at the excavator's tip. This model only considered the shovel breakout forces; it ignored the dynamic forces of payload, the dipper itself, and the reaction forces. Joint torque and force were calculated using a 3-seconds simulation study in that research. The model only incorporated the cutting forces and the dynamic forces of dipper and payload were ignored.

Frimpong and Li (2007) used Lagrange formulations to model the cable shovel and estimated the boom stresses for oil-sands excavation. The cable shovel was modeled as a seven bar linkage and the full multi-body simulations were created in ADAMS /NASTRAN software. No separate resistive model was used. Instead, a spring-dashpots system was used to model the in-situ digging environment for oil-sands as a continuous media. A virtual prototype was created to test the two oil-sands material digging cases. Three-second simulations revealed that the Mises stresses at three nodes of the booms were critical and might exceed the dipper's yield strength.

$$D(\Theta)\ddot{\Theta} + C(\Theta, \dot{\Theta})\dot{\Theta} + G(\Theta) = F_{load} \quad (F_t, F_n) \tag{2.11}$$

Where

$$D(\Theta) = \begin{bmatrix} m_1 + m_2 & m_2 d_2 S_{2_{c2}} \\ m_2 d_2 s_{2_{c2}} & I_{zz1} + I_{zz2} + m_1 d_1^2 + m_2\left(l_1^2 + 2 l_1 d_1 c_{2_{c2}} + d_1^2\right) \end{bmatrix}$$

$$C(\Theta, \dot{\Theta}) = \begin{bmatrix} 0 & \left(m_1 d_1 + m_2\left(l_1 + d_2 c_{2_{c2}}\right)\right)\dot{\theta}_1 \\ 2\left(m_1 d_1 + m_2\left(l_1 + d_2 c_{2_{c2}}\right)\right)\dot{\theta}_1 & 0 \end{bmatrix}$$

$$G(\Theta) = \begin{bmatrix} (m_1 + m_2) g s_1 \\ \left(m_1 d_1 c_1 + m_2\left(l_1 c_1 + d_2 c_{12_{c2}}\right)\right) g \end{bmatrix}$$

$$F_{load}(F_f, F_n) \begin{bmatrix} F_t c_{2\theta_b} & F_n s_{2\theta_b} \\ F_t(I_1 + I_2) & F_t(I_1 + I_2) c_{2\theta_b} \end{bmatrix}$$

Ying Li and Frimpong (2008) extended their research Frimpong and Li (2007) and performed rigid and flexible body analysis in ADAMS/NASTRAN and ADAMS/FLEX software packages respectively. The hybrid virtual prototype simulated the in-situ digging conditions, as had previously described by Frimpong and Li (2007) to calculate the von-Mises stresses for shovel components. Frimpong et al. (2008) advanced the shovel component stress analysis research by Li and Frimpong, (2007) and (2008) for in-situ oil-sand excavation to three different cases. They found that six nodes received the maximum stress in all three different studied cases. These stress values were critical for not-only for low-carbon but also for the lower end of the medium-carbon steel. They also suggested that the boom stresses could be used to assess the operator's efficiency and training.

Awuah-Offei (2005) utilized the Newton-Euler based vector loop equations for the dynamic modeling of the shovel's front-end. This model calculated the dipper's hoist force by incorporating the dynamic weight and excavation forces as the dipper moved through the muck pile. The vector loop equations, however, do not calculate the joint

torques and forces as the vector lengths do not exactly match the dipper's geometric lengths.

2.4. FATIGUE FAILURE MODELING OF EXCAVATORS

Cable shovel excavation is cyclic in nature. The stresses on the front-end assembly vary continuously during a cable shovel's duty cycle (Frimpong et al., 2008). This variation produces fatigue cracks on shovel components. These fatigue cracks can lead to expensive repairs, increased shovel down-times, and possible failures. Pearson et al. (2004) reported a sudden breaking down of a large barge-mounted hydraulic excavator's boom due to fatigue cracks reaching a critical length.

Environmental factors (e.g. freezing temperatures and corrosive materials) impact a metal's toughness. Thus, fatigue crack may lead to brittle fracture. The internal material flaws and welded joints may grow rapidly to undesirable lengths under cyclic loading conditions. Metal fatigue is a complex metallurgical phenomenon that is dependent on the metal's microstructure. The current practice utilized to repair these cracks is experienced-based rather than scientific. Fatigue analysis to assess the damage is important for machine longevity. The fracture growth rates at different areas of the shovel must be understood for a better shovel health and longevity.

Three common fatigue failure analysis approaches are typically used: the stress life approach, strain life approach, and fracture mechanics approach. Each has its own application with overlapping boundaries. The Stress-life approach is typically represented by a Stress vs Number of cycles to failure (S-N) curve, and was introduced by Wöhler as a result of a series of experiments on metal fatigue during the 1850s to 1870s circa. The technique is generally suitable for high cycle fatigue components where material behavior

is elastic i.e. stress-strain levels stay within elastic limits. For shovel dipper-teeth assembly the fracture mechanics approach can be applied.

The strain-life approach is best suited for high stress, low cycle fatigue, in which the stress-strain behavior is plastic. The engineering structures are typically designed to keep the stress ranges within elastic limits, however, there are generally left few notches due to internal material flaws, and welding points. The stress levels around these notches can be well above the elastic ranges and can fall into the plastic ranges. Standardized procedures and recommendations are available for testing and fatigue life predictions (ASTM, 1969; SAE, 1968) using the strain-life approach. The fracture mechanics approach is used to estimate a crack's propagation life. For this approach the initial crack lengths are either known (welds, known defects, porosities, and cracks found during non-destructive testing) or assumed. Fracture mechanics principles and theories are applied to estimate the crack propagation rates and thus the crack-propagation lives. The total fatigue life of a component can be estimated using a combination of strain-life and fracture mechanics approaches.

There are three modes defined for the fatigue failure of metals: - Mode-I, crack opening, Mode-II, in-plane shear or crack opening, and Mode-III, out-of-plane shear or crack twist. Metal failure can also be a result of mixed-mode fatigue. Mode-I fatigue research has dominated the fatigue analysis and life-expectancy field.

A typical crack growth curve is shown in Figure 2.2. Three regions can be identified on this curve: crack initiation, crack propagation, and rapid increase in crack growth leading to failure. Any distinction between the initial two phases is nearly impossible to make. The plastic behavior around the notches can be attributed to the crack-initiation phase. Fatigue life may, however, occur for a longer period of time during

the crack propagation phase as the majority of time for a crack is spent during this phase. A number of models are available to predict the crack propagation phase (the middle region on the curve). Paris and Erdogan (1963) developed an equation, (commonly known as Paris' Law) and is the most commonly used method to estimate the crack propagation. The Paris' Law is given as equation (2.12).

$$\frac{da}{dN} = C(\Delta K)^m \tag{2.12}$$

The slope of the linear region of the curve in Figure 2.2 defines the crack growth rate with every cycle. The material constants (C, m) can be found for different metals in literature or obtained using standard tests (ASTM E647). Here 'K' is the stress intensity factor (SIF).

Bannantine et al. (1989) defined SIF as given in equation (2.14). SIFs can be computed analytically and numerically (Loadkimidis and Theocaris, 1978; Raju and Newman, 1997; Sih, 1973; Tada et al., 1973). The analytical approach is typically useful for simple geometries and force environments. The advantage, however, is its wider range of applicability to crack lengths. In contrast, numerical techniques can be applied to more complicated geometrical and force systems. The downside of numerical technique is that the SIF need to be computed for every crack length. SIFs are now computed mostly using the finite element techniques and many numerical routines are developed for this purpose (MathWorks, 2012).

The stress intensity factor (SIF) 'K' defines the magnitude of local stresses around the crack's tip. The SIF can be computed analytically for simple crack geometries for simple loading and stress cases. The SIF values can also be found in literature for some simple and typical cases. Equation (2.13) is a simplified version of the SIF calculation

model. In its broader form, the equation to calculate SIF can be written as equation (2.14). This equation is the equation for the stress distribution near the crack tip.

$$K = f(g)\sigma\sqrt{\pi a} \tag{2.13}$$

The radius (r) becomes zero at the crack's tip and the stress distribution becomes infinite. This situation leads to plastic deformation of the material. This plastic zone (at the crack tip) is considered as the material's resistance to cracking. This zone must be considered very small before the linear elastic theories can be applied. This plastic zone, ahead of the crack's tip, makes the fundamentals of linear elastic fracture mechanics (LEFM) and has been a subject of fatigue studies for many years. Wilkinson and DeGennaro (2007) presented their theory for the failure of brittle materials. According to this theory, a crack will propagate only if the potential energy released due to crack growth is greater than or equal to increase in surface energy due to creation of new surfaces.

$$\sigma_{ij}(r,\varphi) = \frac{K}{\sqrt{2\pi r}} f_{ij}(\varphi) \; + \; \text{higher order terms} \tag{2.14}$$

The fatigue life can then be computed for a known crack-length by integrating the equation (2.12) resulting into equation (2.15) (Bannantine et al., 1989).

$$N_f = \int_{a_i}^{a_f} \frac{da}{C(\Delta K)^m} \tag{2.15}$$

There is no reported work for fatigue life estimation of cable shovel dipper. The only reported work was done by Yin et al. (2007) and (2008) who estimated the fatigue life for corner cracks in the steel welded box section of the shovel boom. The researchers used finite element method to estimate the crack growth rate and metal properties were found in the lab using standard procedures.

2.5. RATIONALE FOR PHD RESEARCH

The current available dynamic models for the shovel front-end are limited as they generally ignore the dynamic weight forces of the dipper and the payload. These forces, because of the large weight capacity of shovels today, are critical for stress analysis and need proper modeling. No research work is reported to date, to the auther's knowledge, on the stress modeling of cable shovel dipper-teeth assembly in formation excavation engineering. Similarly, there is no work done on life-estimation of dipper components due to fatigue cracking. This research study focuses on these important areas of shovel dipper-teeth stress and fatigue modeling.

The cable shovel front-end kinematic and dynamic models are generally used for shovel performance evaluations in varying digging conditions. One of the key elements of these models is estimation of resistive forces acting on a shovel dipper during excavation. The current shovel dynamic models use one of the many available soil cutting and excavation models to estimate the shovel breakout forces on shovel dipper, and then compute the crowd-force and hoist-torque requirements to overcome these resistive forces. In general, the available kinematic and dynamic models assumed the forces acting at the dipper's tip and ignored the dynamic nature of the resistive forces. Further, the payload is ignored, in general. Hendricks et al. (1993) ignored the in-situ resistive forces on the shovel in their dynamic model of the shovel. Frimpong and Hu (2004) used the Zelenin et al. (1985) empirical model to estimate the cutting resistive forces, however, they ignored the dynamic weight forces of the payload. Given the larger size of the available shovels today, this force may be the largest and most dominant resistive force of all the resistive forces, and hence can not be ignored. Awuah-Offei et al. (2009) included the payload in their model and found this to be the most significant force of all

the resistive force. Their model is based on vector-loop equations and does not provide the detailed information on individual links and joints because not all the vectors represent the actual dipper components. This research would build the shovel kinematic and dynamic models using Newton-Euler equations to solve for the kinematics and dynamics of all links and joints of the shovel front-end. The research would add to the existing knowledge by building dynamic models that include the dynamic resistive cutting forces acting on the teeth, and both the dipper-load and payload.

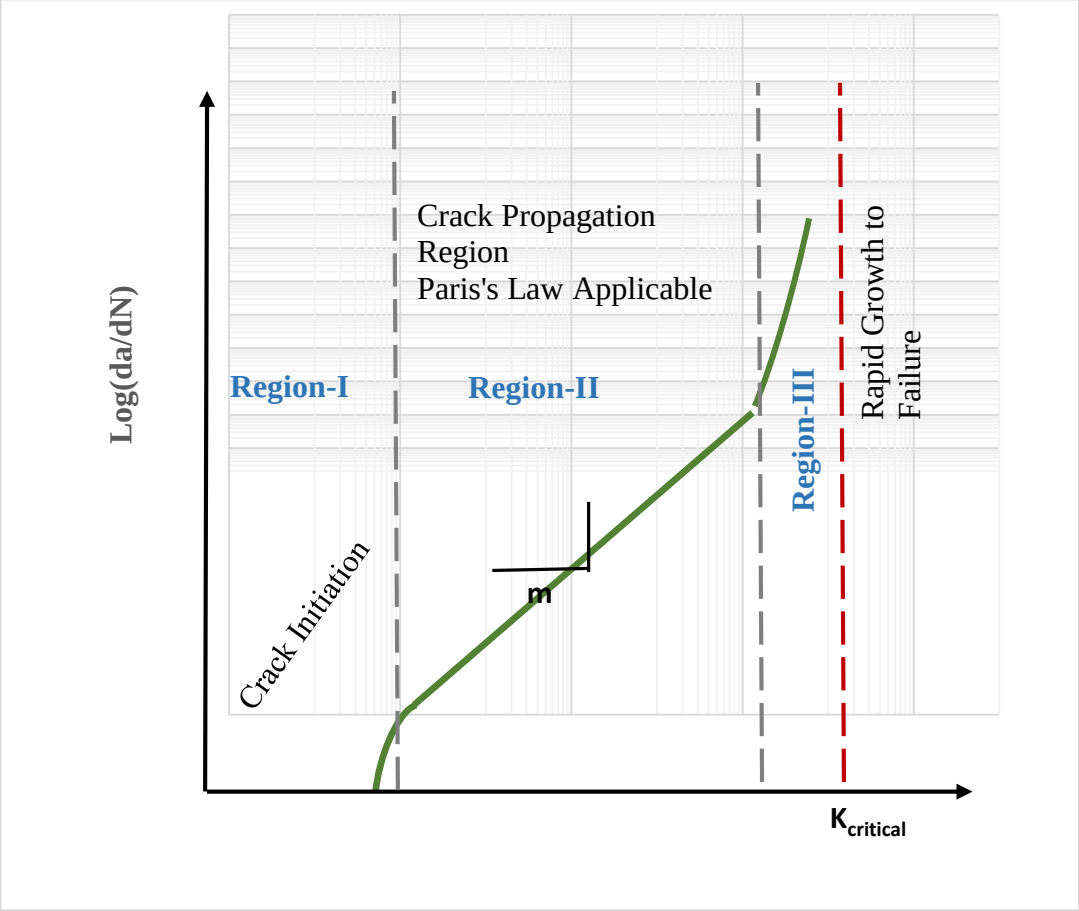

Figure 2.2. A typical crack growth curve, showing three regions

The resistive forces on shovel's dipper-teeth assembly result in stress loading of the shovel components, and for larger shovels the stress levels can be very high. So far, the there is no reported work on stress profile of dipper-teeth assembly, to the knowledge of the author. This research would act as a pioneer research to model the stress profile of dipper-teeth assembly using the dynamic models and a virtual prototype for P&H4100 XPC shovel. The dynamic resistive forces, including the payload and dipper weight, would be included in the model to estimate the stress loading of the dipper-teeth assembly.

The severe stress loading of dipper-teeth assembly can lead to initiation and propagation of cracks that can propagate to critical lengths causing failure without notice. Pearson et al. (2004) noticed that fatigue cracks on shovel boom grew to critical lengths and resulted in a sudden failure for a hydraulic excavator. Yin et al. (2007 and (2008) predicted the life of a corner crack in cable shovel boom under field conditions where the strain levels were measured using strain gauges. There is no reported work on modeling and life expectancy of dipper components due to crack propagation. This research would add to the existing knowledge on crack modeling and failure by modeling the crack propagation behavior on dipper-teeth assembly. The model would be used to predict the life expectancy of dipper components and hence to increase the longevity of dipper-teeth assembly.

2.6. SUMMARY OF LITERATURE REVIEW

A comprehensive literature review has been done for excavation and digging resistive forces, the kinematic and dynamic modeling of shovels, and fatigue/crack failure modeling and life-estimation.The resistive forces on the cable-shovel dipper are complex

in nature. Several attempts have been made to model resistive forces. Several of the recent comprehensive models were made under the following assumptions:

- The shovel excavation is a 2D process where the dipper's width can be incorporated later in calculations.
- The material failure plane is flat (Hemami, 1994; Takahashi et al., 1999).
- The material is homogenous (Hemami, 1994; Takahashi et al., 1999).
- The thickness of the bucket is negligibly small compared with the size of the rock pile (Takahashi et al. (1999).

The model proposed by Hemami (1994) consists of six forces ($f_1 – f_6$), and is by far the most comprehensive model for resistive forces acting on the shovel dipper during the excavation cycle. All of the resistive forces, but f_6, in this model are dynamic in nature. Research has shown that f_1 and f_4 are the most important and dominant forces for shovel digging (Hemami, 1994; Takahashi et al., 1999). The dynamic nature of the resistive forces, particularly those for f_1, are generally ignored in excavation research.

Force f_1 can be modeled using models proposed by either Hemami (1994) or Awuah-Offei et al. (2009). The model by Awuah-Offei et al. (2009) is better than the one developed by Hemami (1994) because it incorporates the dynamic forces. Force f_2 can be set to zero, provided the bottom of the bucket stays clear of the material and does not compress the material by selecting a proper trajectory (Hemami, 1994). Several models can be used to estimate the dipper's cutting force in soil. Only the empirical model created by Zelenin et al. (1985) considers the teeth ahead of the bucket. Force f_4 can be modeled as a part of f_3 using Zelenin et al. (1985) model (Awuah-Offei et al., 2009; Hemami, 1994). The f_5 force can be set to zero if the dipper is assumed to move at a constant speed through the muck pile. Awuah-Offei et al. (2009). Force f_6 is simply the weight of the

dipper and is a known force as it depends both on the dipper's dimensions and the excavated material.

Both Newton-Euler and Lagrange formulations are commonly used for the kinematic and dynamic modeling of a cable shovel. Newton-Euler equations, however, are preferred because of their recursive nature and ease of computer implementation. In general, the forces acting on the dipper were simplified and generally limited to cutting forces only for the dynamic modeling. Particularly, the dynamic nature of the weight and cutting forces is ignored in almost all of the available shovel dynamic models.

The shovel loading is cyclic which can lead to fatigue cracking of the shovel components. Fatigue cracks can propagate to larger lengths leading to failure. The crack life is divided into three phases: initiations, propagation, and failure. Most of the crack-life is during the propagation phase. Paris' Law (Paris et al., 1961) is most commonly used for crack-life estimation. Computation of SIF is a key parameter for life-estimation using this method. Numerical techniques are commonly adopted for complex geometries and loading conditions. No dipper related fatigue modeling and life-estimation work has been done so far.

3. MODELING PHILOSOPHY AND CONSTRAINING ENVIRONMENTS

The cable shovel excavation process must be fully understood in terms of its elements, kinematics, dynamics and resistive forces to completely profile the stresses on front-end assembly and to estimate the expected life. The analytical philosophy and procedures associated with the cable shovel dynamic model and the constraining environments are discussed in this section to provide an understanding into the fundamental basis of this research study.

3.1. CABLE SHOVEL FRONT END ASSEMBLY

A cable shovel's physical structure can be divided into three mechanisms as shown in Figure 1.3. These mechanisms are defined as lower compartment, upper housing, and front-end assembly. A shovel's front-end assembly consists of the boom, saddle block, dipper-handle, dipper and teeth, pulleys, and support and hoisting ropes and rigging. The shovel mechanism uses propel motion to position itself against the working bench; and uses the swing motion to swing the dipper towards or away from the working bench in the horizontal plane. During the digging cycle a shovel does not use propel and swing motions and only uses the crowding and hoisting motions for the dipper to traverse the trajectory. During the digging process, the front-end assembly is subjected to dynamic stress loading. The high stress loading can lead to body-cracking, rope breakage, and tooth losses. The dynamic stress loads of the boom, crowd-arm and ropes have been modeled by Li and Frimpong (2008). The dipper-teeth assembly is, however, not been studied for stresses. There is no published work available for the fatigue failure modeling and life estimation of the whole front-end assembly or for the dipper-teeth assembly.

3.2. DIPPER FORMATION INTERACTION AND RESISTIVE FORCES

The shovel dipper, comprises of the side walls, the base (bottom-plate), the lip and the teeth assembly, as the shovel's excavation tool. The shovel's breakout forces are produced to aid in the excavation process. Resistive cutting forces act on the teeth, side walls, and teeth of the dipper. The dipper is filled as it moves along the trajectory. During its movement through the formation the dynamic force of payload also comes into play. A comprehensive resistive force model incorporates all these forces. The model presented by Hemami (1994) is by far the most comprehensive model for shovel excavation that incorporates all these forces and is selected for this research. The model defines six individual forces ($f_1 – f_6$) as shown in Figure 2.1 and are discussed in section 2-2 of this report. Five out of these six forces are dynamic in nature as they change both in magnitude and direction during excavating. To fully model the stresses on the front-end of a shovel, all these forces are to be computed and incorporated in the shovel model at each time step of the digging cycle. Calculating these forces at every instance of the digging cycle is challenging as it involves defining the position of the dipper and estimating the payload at that instant. As the dipper moves through the muck pile its orientation changes continuously throughout the digging cycle with corresponding changes in the magnitude and direction of cutting forces on the teeth. A detailed dynamic model is required and is, therefore, built to capture the instantaneous position and forces on the dipper.

The weight of the dipper and the payload (f_1 and f_6) are combined as a single dynamic force to reduce the complexity of the dynamic model. This is done with the assumption that the two center of masses are close enough to be treated as concentric. Two of the six forces (f_2 and f_5) can be eliminated (set to zero) by selecting a proper bench geometry and following good excavation practices. Similarly, the impact forces, resulting

from poor operating practice e.g., operator hammering the dipper against bench, or due to the presence of large boulders are ignored.

3.3. KINEMATIC AND DYNAMIC MODELING OF CABLE SHOVEL

During the normal duty cycle of the shovel, the shovel positions itself against the working bench and excavates the material using the crowd and hoist actions of the shovel. The vertical position of the shovel is controlled by the rotation of the crowd-arm around the saddle block, while the horizontal positioning of the dipper is controlled by the crowd-arm extension. The shovel front-end mechanism uses both the rotation and the extension of the crowd-arm (simultaneously) to sweep the dipper through the bench for excavation. The kinematic model of the shovel defines these motions in local coordinate systems and then translates all these into the reference coordinate frame. Both the forward and reverse kinematic models are built for the shovel front-end assembly for this research. The forward kinematic model defines the position of the dipper-tip for a given rotation and extension of crowd-arm as input. The reverse kinematic model uses the dipper-tip position as input and calculates the required rotation and extension of the crowd-arm as outputs. The dipper position is provided in the form of a trajectory function. The motions of the shovel components result in internal dynamic forces and torques acting on the shovel components. The external resistive forces of the material also act on the dipper. Comprehensive kinematic and dynamic models of the front-end assembly are developed to model the motions and dynamic forces on the shovel front-end assembly (Section 4). The models are developed using the Newton-Euler iterative algorithms and incorporate the dynamic resistive forces. Shovel swing and propel motions are not required for this research, therefore, the motion of the front-end assembly is restricted in the vertical plane

only. The kinematics and dynamics of the cable shovel excavation process, as a result, are modeled as a 2D problem.

The front-end of the shovel is shown in Figure 1.3. The shovel crowding mechanism is modeled as a three link system: saddle, crowd-arm, and dipper. These three links are joined through three joints. The saddle is a fixed length link and is free to rotate in the vertical plane. The rotation of the saddle block controls the vertical position of the dipper. The crowd-arm is connected to the saddle block through a prismatic joint and its length varies during the crowding action of the digging operation. The length of the crowd-arm controls the horizontal position of the dipper. The crowd-arm gets the same rotation as of the saddle, while the dipper is oriented at a fixed angle (β) with the crowd-arm. The dipper is also a fixed length link. Rotation of saddle block and the length of the crowd-arm together control the position of the dipper in the vertical plane and define the trajectory. Forward kinematics define the angular velocities and displacements of the links required to place the bucket at a particular point in time and space against the working bench. Reverse kinematics do the opposite and calculates the angular accelerations, velocities and displacements while the dipper travels through the working bench.

The dynamic model of the shovel front-end assembly defines the accelerations and forces acting on the links and joints during the digging operation. The Newton-Euler iterative algorithm is used to build the dynamic model of the cable shovel. The Newton-Euler dynamic algorithm for computing the crowd force and the hoist torque comprises of two parts. First, the velocities and accelerations $(\dot{\omega}, \dot{v})$ are iteratively computed from saddle block to dipper-tip using the Newton-Euler equations. Second, the interactive forces and joint torques (F, N) are computed recursively from the dipper-tip back to the

crowd-arm. The objective of this model is to calculate the force and torque required at the first link to overcome all the resistive forces. Therefore, both of these steps are performed in the forward and reverse direction. The force and torque are computed at the center of mass of each link. Therefore, the velocity and the acceleration of the centroid of each link are also computed at the centroid of each link. This is achieved by assigning an imaginary coordinate frame Ci attached to the centroid of each link. The formation resistive forces (as external forces) are included in the dynamic model. Both the forward and revers dynamic models are developed for this research. Forward dynamics give the force transferred to the bench when a known rotation and torque is given to the first joint. Reverse dynamics calculate the forces and torques for all the links and joints when external forces (resistive forces in this case) act on the dipper. The reverse dynamic model is used to calculate the crowd-arm force and torque required to overcome the digging resistive forces at the first joint, as illustrated in Figure 3.1.

3.4. DIPPER FATIGUE LIFE ESTIMATION

Fatigue cracks appear as a result of the severe stress loading, internal material flaws, and hard excavation conditions. These cracks can propagate to critical lengths, resulting in shovel breakdowns. The fatigue life of a component under stress is composed of three stages – crack initiation, crack-propagation, and rapid growth to failure- as shown in Figure 2.2. Crack initiation can be attributed to a variety of material and environmental reasons including the material imperfections, geometry flaws and stress concentrations. Most of the crack life is spent during the crack propagation stage.

For the fatigue life, pre-defined semi-elliptical cracks of varying lengths are assumed for the teeth and high stressed regions of the dipper components. Stress intensity

factors (SIFs) are computed for all these crack-lengths using the finite element methods. The SIFs are computed indirectly by computing the J-integrals around crack-tips. SIF vs crack-length relationships are established for dipper components in two orthogonal directions. These relationships are used to estimate the residual life of the cracked components as proposed in equation (2.15).

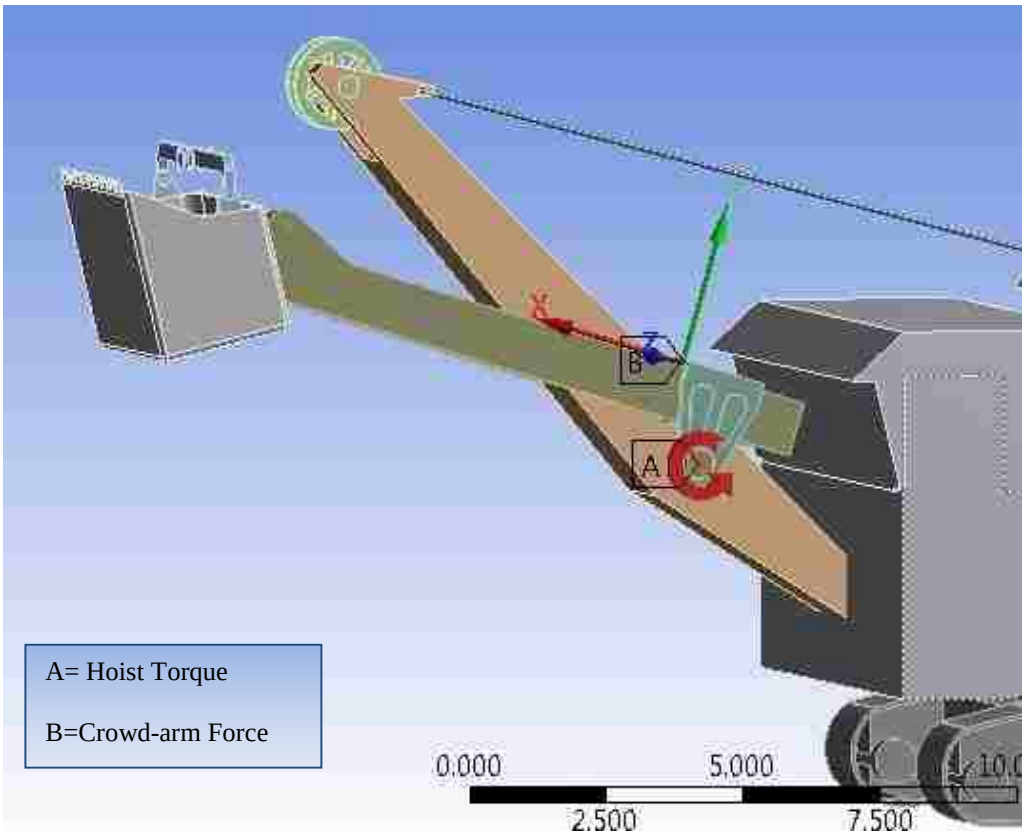

Figure 3.1. Crowd force and hoist torque for the dipper movement

3.5. VIRTUAL PROTOTYPE SIMULATION

Two different kinds of simulations are run for this research. First a numerical simulator is developed in MATLAB/SIMULINK environment. This simulation model is

programed to calculate the instant dynamic cutting and payload forces when a known trajectory is given as an input. A virtual prototype is then developed in ANSYS (R15) software environment. Simulations are run to build a stress profile of the dipper-teeth assembly under varying field conditions. The simulation experiments are conducted to estimate the fatigue life of dipper components.

For both simulations, a virtual working bench is created and a dipper trajectory is defined. The dipper-tip follows this trajectory (from toe to crest) in 3 seconds as illustrated in Figure 3.2. The 3 second simulation time was used for some earlier research (Frimpong & Li (2007), Frimpong et al., (2008)). The same simulation time is selected for a possible comparison of results. The penetration depth is selected in such a way that the dipper is completely filled when the dipper reaches the crest with no spillage of the material. The dipper follows a smooth curve and travels with a constant velocity. This assumption is made to keep the force f_5 zero and is considered as a good shovel operating practice.

In the Simulink based numerical simulator, the instantaneous orientation and position of the dipper is calculated and the resulting cutting forces are calculated. The payload is calculated based on the approach suggested by Awuah-Offei et al. (2009). The approach is 2D and uses the optimization techniques to calculate the area of a polygon to best fit inside the dipper following the material profiling suggested by (Hemami, 1994). The center of mass of this area is calculated using the routines developed by (Sommer III, 2011) and acts as the dynamic center for the payload forces (f_1 and f_6). This simulator provides the necessary input forces for the 3D virtual prototype simulations performed in ANSYS Workbench (R15). ANSYS (R15) has powerful routines to solve the finite element equations with higher accuracy and calculate the stresses on the shovel.

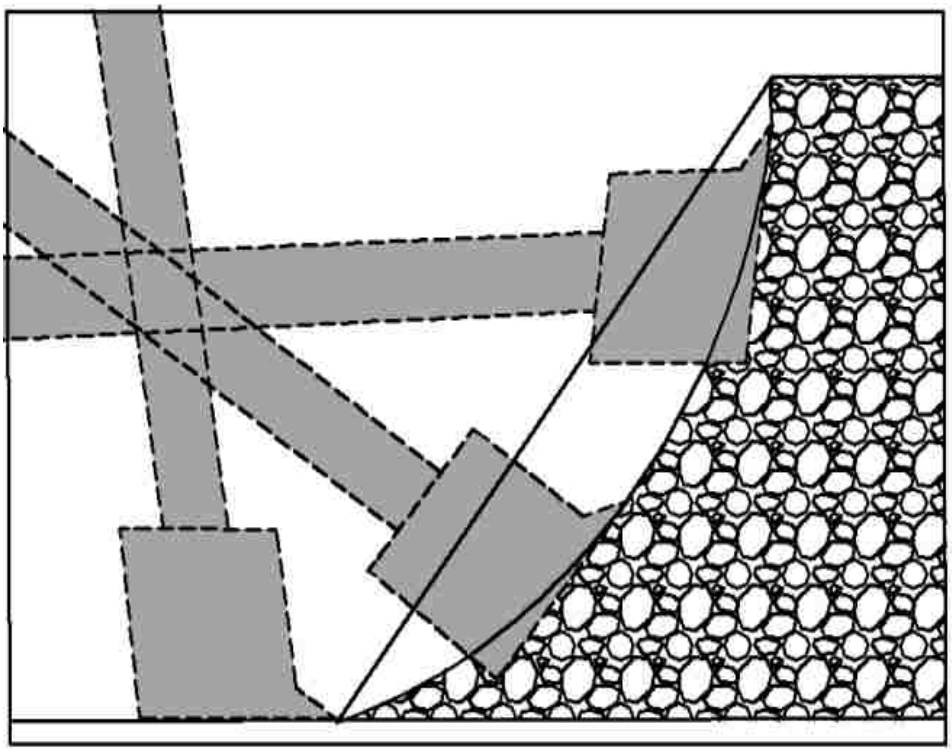

Figure 3.2. Excavation process of a cable shovel dipper

4. DYNAMIC MODEL OF CABLE SOVEL FRONT-END ASSEMBLY

A kinematic model of the shovel is required to completely describe the motions (accelerations, velocities and displacements). The kinematic model further provides a basis for the dynamic model which can be used to calculate the torques and forces on individual components. The complete excavation process of a shovel digging involves propel, crowd and swing motions. However, during the normal duty cycle of the shovel, the shovel positions itself against the working face and does not propel. In this situation only the front-end assembly moves. Further, maximum forces are involved during the excavation phase of shovel working. Therefore, a dynamic model of the front-end assembly alone can suffice to describe the normal duty cycle of cable shovel. The existing kinematic and dynamic models developed by Daneshmend et al. (1993) and Frimpong et al. (2005) are limited as these do not include the dynamic payload forces, however, these models provide a good base to extend the work. The model developed by Awuah-Offei et al. (2009) includes the dynamic payload forces and is developed using the vector loop method. This model does not provide the force and torque information on individual links and joints. The model however, sets the foundation for dynamic payload force and is used in this text as well.

In the following section, kinematic and dynamic models of the cable shovel front-end assembly are developed. The dynamic model incorporate the dynamic resistive forces of formation cutting and weight forces of the bucket and payload. The model developed here uses the dynamic model developed by Frimpong et al. (2005) as the base to build this new model. The dynamic payload force is modeled using the strategy suggested by Awuah-Offei et al. (2009).

4.1. KINEMATIC MODEL OF CABLE SHOVEL FRONT-END

A kinematic model of the shovel describes the position and motions of links and joints during the digging cycle. The front-end of the shovel is shown in Figure 4.1. The shovel front-end mechanism is modeled as a three link system: saddle, crowd-arm, and dipper – and consists of three links and three joints. The saddle is a fixed length link and is free to rotate in the vertical plane. The rotation of the saddle block controls the vertical position of the dipper. The crowd-arm is connected to the saddle block through a Prismatic joint and its length varies during the crowding action of the digging operation. The length of the crowd-arm controls the horizontal position of the dipper. The crowd-arm gets the same rotation as of the saddle, while the dipper is oriented at a fixed angle, β, to the crowd-arm. The dipper is also a fixed length link. Rotation of the saddle block and the length of the crowd-arm together control the position of the dipper in the vertical plane and thus defines the trajectory.

A kinematic scheme is required that can relate the movements of the links and translate the motions and rotations in the reference coordinate frame. The Denvit-Hartenberg (D-H) scheme (Koivo, 1989) is used here to relate the movements and rotation of the links and is a standard in the robotics industry. In the D-H scheme the movements and rotations of individual links are measured in the coordinate frames assigned at every joint location using the D-H scheme (Koivo, 1989). The lower part of the shovel is considered stationary and fixed for this analysis. The $X_oY_oZ_o$ coordinate frame, which is the reference frame, is selected with Z_o along the rotating axis of the saddle block. The coordinate frame $X_1Y_1Z_1$ coincides with the $X_oY_oZ_o$ coordinate frame and measures the rotation of the dipper-handle via the saddle block. Next the coordinate frame $X_2Y_2Z_2$ is

set at the intersection of the saddle block and the dipper-handle, with the Z_2 axis along the translation movement of the dipper-handle (joint-2 being a prismatic joint). The movement of the dipper-handle is measured along this Z_2 axis. The coordinate frame $X_3Y_3Z_3$ is set at the end point of the dipper-handle with Z_3 normal to Z_2. This frame is at a fixed angle from coordinate frame-2. And finally, the frame $X_4Y_4Z_4$ is set at the tip of the dipper with Z_4-axis parallel to Z_3. The material resistive forces acting on the shovel are defined in this frame. The coordinate frame assignments are shown in Figure 4.1.

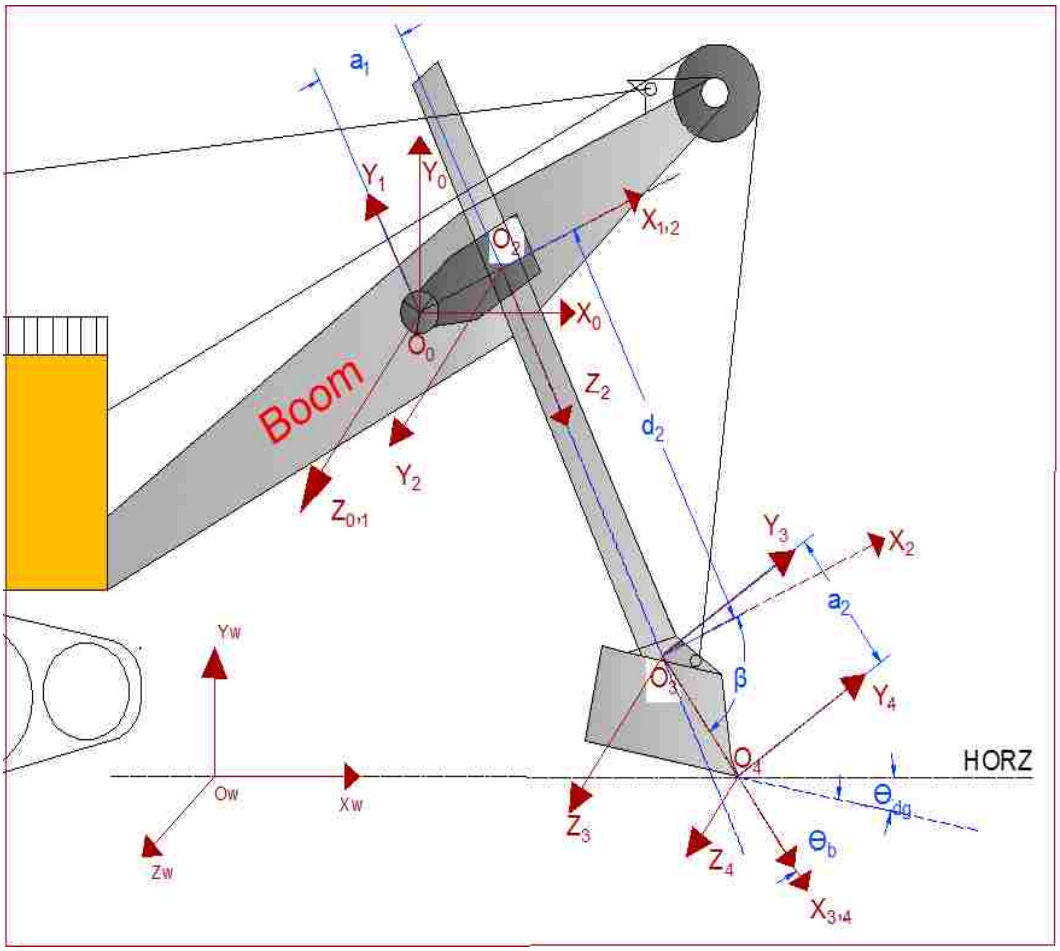

Figure 4.1. Structural kinematic parameters using the D-H procedure

The D-H scheme is used for this purpose here and is a standard in robotics. The structural kinematic parameters of the shovel using the D-H notation (Koivo, 1989) are represented in Figure 4.1 and Table 4.1. Here four values are assigned to each link following the D-H notation. The two values (a_i, d_i) are for the links and represent the constant and variable lengths of the links, while the other two (α_i, θi) are for the connection between links (i.e. joints) and thus represent the rotation of the coordinate frame and rotation of the joint respectively. For a revolute joint a_i, α_i, d_i are fixed and θ_i is a variable. On the other hand, for a prismatic joint (or translational motion) a_i, α_i, θ_i are fixed and d_i is a variable. The crowd-arm movement is via a prismatic joint.

Table 4.1. Structural Kinematic Parameters

Link i	Joint Description	α_i	a_i	d_i	θ_i
1	Saddle – Boom joint	0	0	0	θ_1
2	Saddle –Dipper-handle joint	90	a_1	0	0
3	Dipper-handle – Dipper joint	-90	0	d_2	0
4	Dipper Tip	0	L_2	0	β

4.1.1. Forward Kinematics of Cable Shovel Front-End Assembly. Forward kinematic model defines the positions and motions of the dipper when the rotation and extension of the dipper-handle are known. As described in Section 2, the external

dynamic forces act on the shovel dipper during the excavation cycle. As will be seen in the later part of this section, that the positions, motions and forces need to be transferred from one coordinate frame to the other during the kinematic and dynamic modeling process. A transformation scheme is needed to translate the coordinates of a point, and hence the forces, defined in one coordinate frame to the first coordinate frame.

The homogenous transformation matrix for transferring coordinates from *i-1* coordinate frame to *i* frame, in its general form (Koivo, 1989) for a revolute joint and for a prismatic joint are given in equations (4.1) and (4.2) respectively. The equations are fundamental equations in robotics and can easily be derived considering two links (*i-1* and *i*) connected through a revolute or prismatic joint respectively. These transformation equations are a combination of rotation and translation matrices.

$$T_i^{i-1} = \begin{bmatrix} \cos\theta_i & -\cos\alpha_i \sin\theta_i & \sin\alpha_i \sin\theta_i & a_i\cos\theta_i \\ \sin\theta_i & \cos\alpha_i \cos\theta_i & -\sin\alpha_i\cos\theta_i & a_i\sin\theta_i \\ 0 & \sin\alpha_i & \cos\alpha_i & d_i \\ 0 & 0 & 0 & 1 \end{bmatrix} \tag{4.1}$$

$$T_i^{i-1} = \begin{bmatrix} \cos\theta_i & -\cos\alpha_i \sin\theta_i & \sin\alpha_i \sin\theta_i & 0 \\ \sin\theta_i & \cos\alpha_i \cos\theta_i & -\sin\alpha_i\cos\theta_i & 0 \\ 0 & \sin\alpha_i & \cos\alpha_i & d_i \\ 0 & 0 & 0 & 1 \end{bmatrix} \tag{4.2}$$

Using these general equations (4.1) and (4.2) the individual transformation matrices $T^{i-1}{}_i$ can be formulated. These individual transformation matrices, as given by equations (4.3) through (4.6) relate the representations of a point in the two adjacent coordinate frames as shown in Figure 4.1. These individual transformation matrices can further be multiplied together to obtain a transformation matrix between any two coordinate frames as given by equations (4.7), (4.8), and (4.9). All these transformations

are required for the construction of kinematic and dynamic models of the shovel front-end assembly using the Newton-Euler procedure. The Newton-Euler procedure is iterative in nature and requires the rotations, velocities, accelerations, forces and torques be transformed from one coordinate frame to the other in both forward and reverse directions.

$$T_1^0 = \begin{bmatrix} c_1 & -s_1 & 0 & 0 \\ s_1 & c_1 & 0 & 0 \\ 0 & 0 & 1 & 0 \\ 0 & 0 & 0 & 1 \end{bmatrix} \tag{4.3}$$

$$T_2^1 = \begin{bmatrix} 1 & 0 & 0 & a_1 \\ 0 & 0 & -1 & 0 \\ 0 & 1 & 0 & 0 \\ 0 & 0 & 0 & 1 \end{bmatrix} \tag{4.4}$$

$$T_3^2 = \begin{bmatrix} 1 & 0 & 0 & 0 \\ 0 & 0 & 1 & 0 \\ 0 & -1 & 0 & d_2 \\ 0 & 0 & 0 & 1 \end{bmatrix} \tag{4.5}$$

$$T_4^3 = \begin{bmatrix} c_\beta & -s_\beta & 0 & a_2 c_\beta \\ s_\beta & c_\beta & 0 & a_2 s_\beta \\ 0 & 0 & 1 & 0 \\ 0 & 0 & 0 & 1 \end{bmatrix} \tag{4.6}$$

$$T_2^0 = \begin{bmatrix} c_1 & 0 & s_1 & a_1 c_1 \\ s_1 & 0 & -c_1 & a_1 s_1 \\ 0 & 1 & 0 & 0 \\ 0 & 0 & 0 & 1 \end{bmatrix} \tag{4.7}$$

.

$$T_3^0 = \begin{bmatrix} c_1 & -s_1 & 0 & a_1 c_1 + d_2 s_1 \\ s_1 & c_1 & 0 & a_1 s_1 - d_2 c_1 \\ 0 & 0 & 1 & 0 \\ 0 & 0 & 0 & 1 \end{bmatrix} \tag{4.8}$$

$$T_4^0 = \begin{bmatrix} c_1c_\beta - s_1s_\beta & -c_1s_\beta - s_1c_\beta & 0 & a_2c_1c_\beta - a_2s_1s_\beta + a_1c_1 + d_2s_1 \\ s_1c_\beta + c_1s_\beta & -s_1s_\beta + c_1c_\beta & 0 & a_2s_1c_\beta + a_2c_1s_\beta + a_1s_1 - d_2c_1 \\ 0 & 0 & 1 & 0 \\ 0 & 0 & 0 & 1 \end{bmatrix} \quad (4.9)$$

The transformation matrices defined in equation (4.3) through (4.9) are required to transform coordinates of a point, and hence forces, between adjacent reference frames. These transformations are important for the construction of the dynamic model of the shovel. The transformation matrix given as equation (4.9) is in particular more useful as all the material resistance forces are defined in the coordinate frame-4 (as shown in Figure 4.3) and all those forces need to be translated to be represented in the reference frame-0 for the dynamic model of the shovel.

These transformation matrices play key roles for the development of kinematic and dynamic model of cable shovel. The Newton-Euler method is utilized to analyze the kinematics and dynamics of the cable shovel. The method is an iterative method and in this method the velocities, accelerations, joint torques and forces are iteratively computed from crowd-arm to dipper in the forward direction and from dipper-tip to the saddle block in the reverse direction. It is important to note that other methods do exist for the dynamic modeling e.g., Lagrange method, however, Newton-Euler method is considered superior because of its iterative nature that makes it more suitable for computer simulations.

The propagation of angular and linear velocities from joint to joint can be expressed by the equations (4.10) through (4.13) as given by Craig (1996). These equations are very fundamental in robotics. For a rotational motion the angular and linear velocities are defined by equations (4.10) and (4.11), respectively.

$$^{i+1}\omega_{i+1} = {}^{i+1}_{i}R\ {}^{i}\omega_i + \dot{\theta}_{i+1}\ {}^{i+1}\hat{Z}_{i+1} \quad (4.10)$$

$$^{i+1}v_{i+1} = {}^{i+1}_{i}R\,(^{i}v_{i} + {}^{i}\omega_{i} \times {}^{i}P_{i+1}) \tag{4.11}$$

And for a prismatic joint (translational motion), the corresponding angular and linear velocity relations are as given by equations (4.12) and (4.13) respectively.

$$^{i+1}\omega_{i+1} = {}^{i+1}_{i}R\,{}^{i}\omega_{i} \tag{4.12}$$

$$^{i+1}v_{i+1} = {}^{i+1}_{i}R\,(^{i}v_{i} + {}^{i}\omega_{i} \times {}^{i}P_{i+1}) + \dot{d}_{i}\hat{Z}_{i} \tag{4.13}$$

As can be observed from equations (4.10) through (4.13) that all these velocity propagation equations involve a rotation matrix, R, which can be derived from the transformation matrices defined in equations (4.3) through (4.9). The transformation matrix are a combination of rotation and translation. The 3x3 matrix within a transformation matrix T^{i-1}_{i} (consisting of first three rows and first three columns) represents the corresponding rotation matrix R^{i-1}_{i}.

The forward kinematic starts from the first link, saddle block, and moves outwards toward the last link, the dipper. The objective is to determine the propagation of the joint rotation and velocities from the joint 1 to the dipper tip. Coordinate frames are already assigned at every joint location. The model uses the same start point equations and basic simplifying assumption as used by Frimpong et al. (2005); and as a result, the kinematic equations are very similar as well. However, the resulting dynamic model is different as an improved scheme for resistive forces is used for this model.

The reference frame {0} is fixed with the lower frame through the boom. The lower structure of the shovel is fixed, so its velocities and accelerations, both linear and angular, remain zero at all times during the excavation phase. These values change only during the propel motion of shovel which is not considered for this research.

$$ {}^{0}\omega_{0} = \begin{bmatrix} 0 \\ 0 \\ 0 \end{bmatrix} \tag{4.14} $$

The joint velocity can be determined taking a derivative of rotation of joint -1. Similarly, the linear velocity of the stationary lower structure of the shovel is zero.

$$ \frac{d\,{}^{0}\omega_{0}}{dt} = {}^{0}\dot{\omega}_{0} = \begin{bmatrix} 0 \\ 0 \\ 0 \end{bmatrix} \tag{4.15} $$

$$ {}^{0}\mathrm{v}_{0} = \begin{bmatrix} 0 \\ 0 \\ 0 \end{bmatrix} \tag{4.16} $$

$$ \frac{\mathrm{d}\,{}^{0}\mathrm{v}_{0}}{\mathrm{dt}} = {}^{0}\dot{\mathrm{v}}_{0} = \begin{bmatrix} 0 \\ 0 \\ 0 \end{bmatrix} \tag{4.17} $$

From equation (4.10) for the first joint (i=0), a revolute joint, the equation (4.18) is obtained. It is evident from this equation that angular velocity of the first link is only around Z-axis and is equivalent to the rate of change of angular rotation around first joint.

$$ {}^{1}\omega_{1} = {}^{1}_{0}\mathrm{R}\ {}^{0}\omega_{0} + \dot{\theta}_{1}\ {}^{1}\hat{\mathrm{Z}}_{1} = \begin{bmatrix} 0 \\ 0 \\ \dot{\theta}_{1} \end{bmatrix} \tag{4.18} $$

The propagation of linear velocity to first joint can be computed using equation (4.11). The first link experiences only the rotational motion, therefore, the linear velocity of first joint is zero.

$$ {}^{1}\mathrm{v}_{1} = {}^{1}_{0}\mathrm{R}\,({}^{0}\mathrm{v}_{0} + {}^{0}\omega_{0}\ \mathrm{X}\ {}^{0}\mathrm{P}_{1}) = \begin{bmatrix} 0 \\ 0 \\ 0 \end{bmatrix} \tag{4.19} $$

For the joint 2 (*i*=1), which is a prismatic joint, equation (4.12) is used to compute the angular velocity of the link-2 (the crowd-arm). The propagation of angular velocity to the 2nd joint, as given in equation (4.20), shows that the angular velocity of 2nd joint is dependent upon the rate of change of angular rotation of joint-1 and there is only an axis shift involved (from Z-axis to Y-axis) during the propagation.

$$ {}^{2}\omega_2 = {}^{2}_{1}R\ {}^{1}\omega_1 + \dot{\theta}_2\ {}^{2}\hat{Z}_2 = \begin{bmatrix} 0 \\ \dot{\theta}_1 \\ 0 \end{bmatrix} \tag{4.20} $$

$$ \therefore \theta_2 = 0, \quad \dot{\theta}_2 = 0, \ \ddot{\theta}_2 = 0 $$

And the linear velocity propagation to 2nd joint is calculated as equation (4.21).

$$ {}^{2}v_2 = {}^{2}_{1}R\left({}^{1}v_1 + {}^{1}\omega_1 \wedge {}^{1}P_2\right) = \begin{bmatrix} 0 \\ 0 \\ -a_1\dot{\theta}_1 \end{bmatrix} \tag{4.21} $$

Similarly, the angular and translational velocities are calculated for the 3rd joint as equation (4.22) and (4.23).

$$ {}^{3}\omega_3 = \begin{bmatrix} 0 \\ 0 \\ \dot{\theta}_1 \end{bmatrix} \tag{4.22} $$

$$ {}^{3}v_3 = {}^{3}_{2}R\,({}^{2}v_2 + {}^{2}\omega_2\ X\ {}^{2}P_3) = \begin{bmatrix} d_2\dot{\theta}_1 \\ a_1\dot{\theta}_1 \\ 0 \end{bmatrix} \tag{4.23} $$

Again, the angular velocity of joint 3 is equivalent to rate of change of angular rotation of joint 1. As there is only one rotation of the joint is involved for the front-end during the digging cycle, therefore, the angular velocity of the joint-4 is also the same as

that the angular velocity of the joint 1. Alternately, it can be stated that the whole front-end assembly gets the same rotation as of the joint-1 during the digging cycle and the angular velocity only involves the axis shift.

$$ {}^{4}v_{4} = {}^{4}_{3}R\left({}^{3}v_{3} + {}^{3}\omega_{3} \wedge {}^{3}P_{4}\right) = \begin{bmatrix} d_{2}\dot{\theta}_{1}c_{\beta} + (a_{1} + a_{2})\dot{\theta}_{1}s_{\beta} \\ -d_{2}\dot{\theta}_{1}s_{\beta} + (a_{1} + a_{2})\dot{\theta}_{1}c_{\beta} \\ 0 \end{bmatrix} \qquad (4.24) $$

The equation (4.10) through (4.24) define the forward kinematics of the shovel front-end. The angular and linear velocities of the shovel front-end components can be defined with these equation once the initial rotation and crow-arm extension is known.

4.1.2. Inverse Kinematics of Cable Shovel Front-End Assembly. The inverse kinematics of shovel determines the set of joint angles and the length for dipper-handle when the desired position and orientation of shovel dipper is known in the reference coordinate frame-0. This inverse kinematic is useful when the dipper traverses a known trajectory and the interest is to determine the joint rotation and crowd-arm extension required to achieve this trajectory. A simple approach is adopted here, similar to the one used by Wu (1995) for the reverse kinematic model of cable shovel, to determine the crowd-arm extension and rotation when the known trajectory points are known.

The inverse kinematic model can be achieved by coordinate transformations to obtain the bucket coordinate in coordinate frame-4, relative to coordinate frame-1. Using the transformation matrix equations ((4.3) to (4.6)), the equation (4.25) is obtained. Also, the same transformation matrix can be defined as equation (4.28).

$$ T_{4}^{1} = \begin{bmatrix} c_{\beta} & -s_{\beta} & 0 & a_{1} + a_{2}c_{\beta} \\ s_{\beta} & c_{\beta} & 0 & a_{2}s_{\beta} - d_{2} \\ 0 & 0 & 1 & 0 \\ 0 & 0 & 0 & 1 \end{bmatrix} \qquad (4.25) $$

$$T_1^0 T_2^1 T_3^2 T_4^3 = T_4^0 \tag{4.26}$$

$$T_2^1 T_3^2 T_4^3 = \left[T_1^0\right]^{-1} T_4^0 \tag{4.27}$$

$$T_4^1 = \left[T_1^0\right]^{-1} T_4^0 \tag{4.28}$$

$$T_4^0 = \begin{bmatrix} r_{11} & r_{12} & r_{13} & p_x \\ r_{21} & r_{22} & r_{23} & p_y \\ r_{31} & r_{32} & r_{33} & p_z \\ 0 & 0 & 0 & 1 \end{bmatrix} \tag{4.29}$$

Where the individual matrix elements are given as follows:

$$r_{11} = c_1 c_\beta - s_1 s_\beta, \qquad r_{12} = -c_1 s_\beta - s_1 c_\beta, \qquad r_{13} = 0$$
$$r_{21} = s_1 c_\beta + c_1 s_\beta, \qquad r_{22} = -s_1 s_\beta + c_1 c_\beta, \qquad r_{23} = 0$$
$$r_{31} = 0, \qquad r_{32} = 0, \qquad r_{33} = 1$$
$$p_x = a_2 c_1 c_\beta - a_2 s_1 s_\beta + a_1 c_1 + d_2 s_1$$
$$p_y = a_2 s_1 c_\beta + a_2 c_1 s_\beta + a_1 s_1 - d_2 c_1$$
$$p_z = 0$$

Here (p_x, p_y, p_z) are the coordinates of the dipper tip in the reference coordinate frame-0.

$$\left[T_1^0\right]^{-1} = \begin{bmatrix} c_1 & s_1 & 0 & 0 \\ -s_1 & c_1 & 0 & 0 \\ 0 & 0 & 1 & 0 \\ 0 & 0 & 0 & 1 \end{bmatrix} \tag{4.30}$$

The equation (4.1) can be represented by the left hand side of equation (4.31). Comparing the equations (4.25) and (4.30).

$$\begin{bmatrix} - & - & - & c_1 p_x + s_1 p_y \\ - & - & - & -s_1 p_x + c_1 p_y \\ - & - & - & p_z \\ - & - & - & 1 \end{bmatrix} = \begin{bmatrix} c_\beta & -s_\beta & 0 & a_1 + a_2 c_\beta \\ s_\beta & c_\beta & 0 & a_2 s_\beta - d_2 \\ 0 & 0 & 1 & 0 \\ 0 & 0 & 0 & 1 \end{bmatrix} \tag{4.31}$$

Now simple arithmetic and trigonometric operations can be applied to calculate the crowd-arm extension and rotation as is explained trough equation (4.32) through (4.48). Equating the (1,4), (2,4) and (3,4) elements of equation (4.31), equations (4.32), (4.33) and (4.34) are obtained.

$$c_1 p_x + s_1 p_y = a_1 + a_2 c_\beta \tag{4.32}$$

$$-s_1 p_x + c_1 p_y = a_2 s_\beta - d_2 \tag{4.33}$$

$$Pz = 0 \tag{4.34}$$

Squaring and adding both equations (4.32) and (4.33) and rearranging, the equation (4.35) is obtained for the crowd-arm extension. Using this equation, the crow-arm extension can be calculated if the end coordinates of the dipper tip (trajectory) are known.

$$d_2 = a_2 s_\beta + \sqrt{p_x^2 + p_y^2 - a_1^2 - a_2^2 - 2a_1 a_2 c_\beta + \left(a_2 s_\beta\right)^2} \tag{4.35}$$

To obtain an equation for the angular rotation of crowd-arm (θ) for the known trajectory coordinates the following simplification operation is adopted. Suppose p_x and p_y can be represented by the equation (4.36) and (4.37).

$$p_x = r\cos\varphi \tag{4.36}$$

$$p_y = r\sin\varphi \tag{4.37}$$

Equations (4.38) and (4.39) are obtained after squaring and adding equations (4.36) and (4.37) and applying basic trigonometric identities. Equations (4.40) through (4.47) use basic trigonometric functions to eliminate the assumed parameters (r and φ) and obtain an equation for the angular rotation of first joint and hence the front-end assembly.

$$r = \sqrt{p_x^2 + p_y^2} \tag{4.38}$$

$$\varphi = A\tan 2(p_y, p_x) \tag{4.39}$$

$$-s_1 c_\varphi + c_1 s_\varphi = \frac{a_2 s_\beta - d_2}{r} \tag{4.40}$$

$$-s_1 c_\varphi + c_1 s_\varphi = \frac{a_2 s_\beta - d_2}{r} \tag{4.41}$$

$$\sin(\varphi - \theta_1) = \frac{a_2 s_\beta - d_2}{r} \tag{4.42}$$

$$\sin^2(\varphi - \theta_1) = \left(\frac{a_2 s_\beta - d_2}{r}\right)^2 \tag{4.43}$$

$$\cos(\varphi - \theta_1) = \pm\sqrt{1 - \left(\frac{a_2 s_\beta - d_2}{r}\right)^2} \tag{4.44}$$

$$\varphi - \theta_1 = A\tan 2\left(\frac{a_2 s_\beta - d_2}{r}, \pm\sqrt{1 - \frac{(a_2 s_\beta - d_2)^2}{r^2}}\right) \tag{4.45}$$

$$\theta_1 = \varphi - A\tan 2\left(a_2 s_\beta - d_2, \pm\sqrt{r^2 - (a_2 s_\beta - d_2)^2}\right) \tag{4.46}$$

$$\theta_1 = A\tan 2(p_y, p_x) - A\tan 2\left(a_2 s_\beta - d_2, \pm\sqrt{p_x^2 + p_y^2 - (a_2 s_\beta - d_2)^2}\right) \tag{4.47}$$

$$\theta_1 = A\tan 2\left(a_2 s_\beta - d_2, \pm\sqrt{p_x^2 + p_y^2 - (a_2 s_\beta - d_2)^2}\right) - A\tan 2(p_y, p_x) \tag{4.48}$$

Using equations (4.35) and (4.48), the crowd-arm extension and angular rotation of joint-1 can be determined when the end coordinates of dipper in reference coordinate fram-0 are known. The end coordinates of the dipper represent the trajectory followed by the dipper during the excavation process.

The forward and reverse kinematic models are built using the Newton-Euler iterative method. The kinematic model can be used to compute, best when implemented through a computer simulation, the positions and velocities of individual links and joints of the front-end assembly for a known trajectory.

4.2. DYNAMIC MODEL OF CABLE SHOVEL FRONT-END ASSEMBLY

The dynamic model defines the accelerations and forces acting on the links and joints of the cable shovel. The forces require the computation of angular and linear accelerations, which can be obtained by time-integration of the angular and linear velocities computed in the kinematic model. In its general form the dynamic model can be defined as in equation (4.49).

$$D(\Theta)\ddot{\Theta} + C(\Theta, \dot{\Theta})\dot{\Theta} + G(\Theta) = F - F_{load} \quad (F_t, F_n) \tag{4.49}$$

Where

$$D(\Theta) = \text{mass matrix}$$

$$C(\Theta, \dot{\Theta}) = \text{centrifugal and Coriollisterms}$$

$$G(\Theta) = \text{gravity terms}$$

This dynamic model for a shovel can be built using the Newton-Euler method. As stated previously, Newton-Euler method is considered superior because of its iterative nature that makes it more suitable for computer simulations.

The dynamic model is based on the kinematic model and uses the position and velocity relationships computed during the kinematic model. The Newton-Euler dynamic algorithm for computing the crowd force and the hoist torque comprises of the following steps:

1. Compute the angular acceleration ($\dot{\omega}_i$) of every link in the forward direction, starting from the saddle and moving outward towards the last link (the dipper).
2. Compute the acceleration ($\dot{v}_i$) of every link in the system in the forward direction.
3. Compute the acceleration ($\dot{v_{ic}}$) at the center of mass (centroid) of every link in the system in the forward direction.
4. Determine the force (F_i) acting on every link at the centroid of the link using ($\dot{v_{ic}}$) and mass of the link.
5. Compute the joint torque (N_i) for every link.

The force and torque are computed at the centroid of each link, therefore, the velocity and the acceleration of the centroid of every link are also computed.

The above steps are applied to the three links of the cable shovel front-end assembly in the forward direction sequentially. First, the angular acceleration for joint-1 is calculated as equation (4.50). The parameters on the right hand side of this equation (4.50) are already computed during the kinematic model.

$$ {}^1\dot{\omega}_1 = {}^1_0R\ {}^0\omega_0 \wedge \dot{\theta}_1\ {}^1\hat{Z}_1 + {}^1_0R\ {}^0\dot{\omega}_0 + \ddot{\theta}_1\ {}^1\hat{Z}_1 = \begin{bmatrix} 0 \\ 0 \\ \ddot{\theta}_1 \end{bmatrix} \qquad (4.50) $$

For the dynamic model, acceleration due to gravity also need to be included. The gravity effect in the reference frame is calculated as ${}^0\dot{v}_0 = g\hat{y}_0$ (vertically downward in the reference frame).

The acceleration of the first link is calculated as equation (4.51) after the inclusion of the gravity terms as well.

$$ {}^{1}\dot{v}_1 = {}^{1}_{0}R\left({}^{0}\dot{\omega}_0 \wedge {}^{0}P_1 + {}^{0}\omega_0 \wedge \left({}^{0}\omega_0 \wedge {}^{0}P_1\right) + {}^{0}\dot{v}_0\right) + 2{}^{1}\omega_1 \wedge \dot{d}_1 {}^{1}\hat{Z}_1 + \ddot{d}_1 {}^{1}\hat{Z} = \begin{bmatrix} gs_1 \\ gc_1 \\ 0 \end{bmatrix} \quad (4.51) $$

Similarly, the acceleration of the link at the center of gravity of each link is calculated using the angular acceleration and transformation matrices. This acceleration is used to compute the forces acting on each link using the 2nd law of motion. To calculate acceleration at the center of gravity of each link an imaginary frame C_i is attached at the centroid of each link. The direction of this imaginary frame is considered the same as that of the coordinate frame-*i*. The acceleration of the center of gravity of first link is calculated as equation (4.52).

$$ {}^{1}\dot{v}_{c1} = {}^{1}\dot{v}_{c1} = {}^{1}\dot{\omega}_1 \wedge {}^{1}P_{c1} + {}^{1}\omega_1 \wedge \left({}^{1}\omega_1 \wedge {}^{1}P_{c1}\right) + {}^{1}\dot{v}_1 = \begin{bmatrix} -\frac{a_1}{2}\dot{\theta}_1^2 + gs_1 \\ \frac{a_1}{2}\ddot{\theta}_1 + gc_1 \\ 0 \end{bmatrix} \quad (4.52) $$

Considering the symmetry in each link, the inertia matrix for the first link can be defined as equation (4.52a).

$$ {}^{c1}I_1 = \begin{bmatrix} I_{xx1} & 0 & 0 \\ 0 & I_{yy1} & 0 \\ 0 & 0 & I_{zz1} \end{bmatrix} \quad (4.52a) $$

A similar assumption was kept by Frimpong et. al., (2005). The torque for the first link is then defined as equation (4.53). The force acting on the first link is finally computed as equation (4.54).

$$ {}^{1}N_1 = {}^{c1}I_1 {}^{1}\dot{\omega}_1 + {}^{1}\omega_1 \wedge {}^{c1}I_1 {}^{1}\omega_1 = \begin{bmatrix} 0 \\ 0 \\ I_{zz1}\ddot{\theta}_1 \end{bmatrix} \quad (4.53) $$

$$ {}^{1}F_1 = m_1 {}^{1}\dot{v}_{c1} = \begin{bmatrix} -m_1 \frac{a_1}{2} \dot{\theta}_1^2 + m_1 g s_1 \\ m_1 \frac{a_1}{2} \ddot{\theta}_1 + m_1 g c_1 \\ 0 \end{bmatrix} \tag{4.54} $$

Similarly, for the 2nd link the same procedure is repeated as was done for the first link. As a first step, the angular acceleration of the 2nd link is computed as equation (4.55).

$$ {}^{2}\dot{\omega}_2 = \begin{bmatrix} 0 \\ \ddot{\theta}_1 \\ 0 \end{bmatrix} \tag{4.55} $$

The second link (crowd-arm) rotates with the same angular acceleration as that of the first joint. Therefore, the angular acceleration of the second link is equivalent the angular acceleration of the first joint. The linear velocity of the crowd-arm is computed as equation (4.56).

$$ {}^{2}\dot{v}_2 = \begin{bmatrix} -a_1\dot{\theta}_1^2 + g s_1 + 2\dot{d}_2\dot{\theta}_1 \\ 0 \\ -a_1\ddot{\theta}_1 - g c_1 + \ddot{d}_2 \end{bmatrix} \tag{4.56} $$

The linear velocity at the centroid of the crowd-arm is computed by equation (4.57). An imaginary frame is assigned at the centroid of the crowd-arm and velocity is computed in that reference frame.

$$ {}^{2}\dot{v}_{c2} = \begin{bmatrix} -a_1\dot{\theta}_1^2 + 2\dot{d}_2\dot{\theta}_1 + \frac{d_2}{2}\ddot{\theta}_1 + g s_1 \\ 0 \\ -\frac{d_2}{2}\dot{\theta}_1^2 - a_1\ddot{\theta}_1 + \ddot{d}_2 - g c_1 \end{bmatrix} \tag{4.57} $$

The torque of the crowd-arm can be computed using equation (4.58). A similar symmetry assumption is maintained as was assumed for the first link.

$$ {}^{2}N_2 = \begin{bmatrix} 0 \\ I_{yy2}\ddot{\theta}_1 \\ 0 \end{bmatrix} \tag{4.58} $$

The translated force for the crowd-arm is calculated using equation (4.59).

$$ {}^{2}F_2 = \begin{bmatrix} -m_2 a_1 \dot{\theta}_1^2 + 2m_2 \dot{d}_2 \dot{\theta}_1 + m_2 \frac{d_2}{2} \ddot{\theta}_1 + m_2 g s_1 \\ 0 \\ -m_2 \frac{d_2}{2} \dot{\theta}_1^2 - m_2 a_1 \ddot{\theta}_1 + m_2 \ddot{d}_2 - m_2 g c_1 \end{bmatrix} \tag{4.59} $$

And similarly, for the 3rd link (dipper) the same procedure is repeated. The dipper is fixed with the crowd-arm. Therefore, the angular acceleration of the dipper is exactly the same as that of the crowd-arm itself, which in turn is equivalent to the rotational acceleration of the first joint at saddle block. The rotational acceleration of the dipper is given as equation (4.60).

$$ {}^{3}\dot{\omega}_3 = \begin{bmatrix} 0 \\ 0 \\ \ddot{\theta}_1 \end{bmatrix} \tag{4.60} $$

The linear acceleration of the dipper is similarly computed using the general equation shown as part of equation (4.51). The acceleration at the centroid of the dipper is computed as equation (4.62).

$$ {}^{3}\dot{v}_3 = \begin{bmatrix} d_2 \ddot{\theta}_1 - a_1 \dot{\theta}_1^2 + 2\dot{d}_2 \dot{\theta}_1 + g s_1 \\ + d_2 \dot{\theta}_1^2 + a_1 \ddot{\theta}_1 - \ddot{d}_2 + g c_1 \\ 0 \end{bmatrix} \tag{4.61} $$

$$ {}^{3}\dot{v}_{c3} = \begin{bmatrix} d_2 \ddot{\theta}_1 - \left(\frac{a_3}{2} + a_1 \right) \dot{\theta}_1^2 + 2\dot{d}_2 \dot{\theta}_1 + g s_1 \\ \left(\frac{a_3}{2} + a_1 \right) \ddot{\theta}_1 + d_2 \dot{\theta}_1^2 - \ddot{d}_2 + g c_1 \\ 0 \end{bmatrix} \tag{4.62} $$

Torque at the gravity center of the crowd-arm can be calculated using the equation (4.63). A dipper is assumed symmetrical and is consistent with the previous research (Frimpong et. al., 2005).

$$ {}^{3}N_{3} = \begin{bmatrix} 0 \\ 0 \\ I_{zz3}\ddot{\theta}_1 \end{bmatrix} \tag{4.63} $$

The translated force on the dipper is computed as equation (4.64) using the linear acceleration at the centroid of the dipper.

$$ {}^{3}F_{3} = \begin{bmatrix} m_3 d_2 \ddot{\theta}_1 - m_3\left(\frac{a_3}{2} + a_1\right)\dot{\theta}_1^2 + 2m_3\dot{d}_2\dot{\theta}_1 + m_3 g s_1 \\ m_3\left(\frac{a_3}{2} + a_1\right)\ddot{\theta}_1 + m_3 d_2\dot{\theta}_1^2 - m_3\ddot{d}_2 + m_3 g c_1 \\ 0 \end{bmatrix} \tag{4.64} $$

Equations (4.50) to (4.64) describe the forward dynamics of the shovel front-end. This forward dynamic model can be used to compute the force and torque available on the dipper tip for the initial force and torque of the first joint. The equations (4.50) through (4.64) are useful as the acceleration, torque and force for every link and joint of the shovel can be computed iteratively. This helps in designing a better digging operation that can minimize the force and torque requirement.

For this research a reverse dynamic model is required that incorporates the payload and resistive forces on shovel. The reverse dynamic model computes the force and torque required at the saddle joint to overcome the resistive digging and material forces as shown in Figure 4.2. The reverse dynamic model can be built by writing force and moment balance equations starting from the dipper-tip and moving backward towards the first joint.

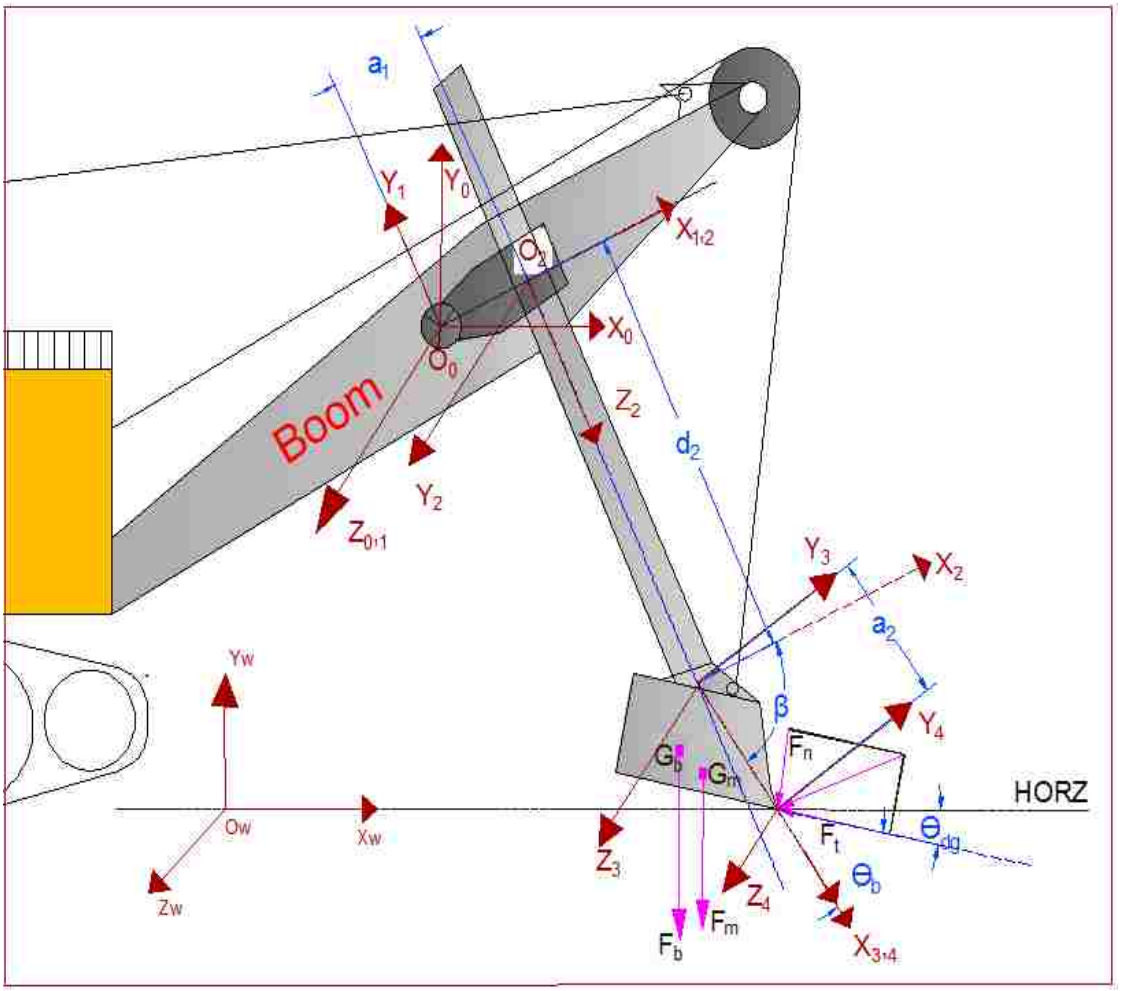

Figure 4.2. External forces on the dipper

The force and torque shown in Figure 3.1 are the most important parameters for dynamic model of the shovel. In fact, the whole dynamic modeling effort is done to compute these two parameters. These represent the crowd force for the dipper to penetrate the formation, and the hoisting torque required to move the dipper through the formation. These shovel power packs must be able to provide this crowding force and hoisting torque to overcome the digging resistive and weight forces on the shovel. Shovel digging and energy efficiency is directly linked with these two parameters (Awuah-Offei, 2007).

The resistive forces on the shovel are described in Figure 4.2. The external forces acting on the dipper teeth are resolved into its constituent components – F_t and F_n – parallel and perpendicular to the teeth (the bottom of the bucket as well) plane respectively. These forces are evaluated in coordinate frame-4 as (4.65) and (4.66).

$$ {}^{4}f_{4x} = F_t c_{\theta b} + F_n s_{\theta b} \tag{4.65} $$

$$ {}^{4}f_{4y} = -F_t s_{\theta b} - F_n c_{\theta b} \tag{4.66} $$

The inward or reverse dynamics is computed in a systematic and iterative method using the Newton-Euler formulations. The inward iteration for the dipper is calculated as equations (4.67) and (4.68). As seen in the equation the forces of i^{th} reference frame are translated backward in the $(i\text{-}1)^{th}$ reference frame.

$$ {}^{3}f'_{3} = {}^{4}_{3}R\,{}^{4'}f_{4'} + {}^{3}F'_{3} \tag{4.67} $$

$$ {}^{3}f_{3} = \begin{bmatrix} -F_t C_{\theta b} C_{\beta} + F_n S_{\theta b} C_{\beta} - F_t S_{\theta b} S_{\beta} - F_n C_{\theta b} S_{\beta} \\ +F_t C_{\theta b} S_{\beta} - F_n S_{\theta b} S_{\beta} - F_t S_{\theta b} C_{\beta} - F_n C_{\theta b} C_{\beta} \\ 0 \end{bmatrix} \tag{4.68} $$

$$ + \begin{bmatrix} m_3 d_2 \ddot{\theta}_1 - m_3\left(\frac{a_3}{2} + a_1\right)\dot{\theta}_1^2 + 2m_3 \dot{d}_2 \dot{\theta}_1 + m_3 g s_1 \\ m_3\left(\frac{a_3}{2} + a_1\right)\ddot{\theta}_1 + m_3 d_2 \dot{\theta}_1^2 - m_3 \ddot{d}_2 + m_3 g c_1 \\ 0 \\ \end{bmatrix} $$

Other than the external excavation resistive forces, there are dynamic resistive forces of the payload and dipper itself. These forces also need to be translated backward to the reference frame 3. The magnitude and point of application *of* these forces are separate. However, for simplicity these forces are combined into a single force acting at

the centroid of the dipper. A similar assumption was made by Frimpong et. al., (2005) and Awuah-Offei, (2009). This combined forces (F_p) is shown in Figure 4.3. A coordinate frame-4' is imagined to be assigned at the center of mass of these weight forces and the forces for inward dynamics of the dipper system.

$$ {}^{4}f'_{4x} = F_p c_{\theta e} \tag{4.69} $$

$$ {}^{4}f'_{4y} = -F_p s_{\theta e} \tag{4.70} $$

$$ {}^{3}f'_{3} = {}^{4}_{3}R\, {}^{4'}f_{4'} + {}^{3}F'_{3} \tag{4.71} $$

$$ {}^{3}f'_{3} = \begin{bmatrix} F_p c_{\theta e} c_{\beta'} - F_p s_{\theta e} s_{\beta'} \\ -F_p c_{\theta e} s_{\beta'} - F_p s_{\theta e} c_{\beta'} \\ 0 \end{bmatrix} \tag{4.72} $$

The resulting reverse force translated to reference frame-3 is given as equation (4.73).

$$ {}^{3}f_{3} = \begin{bmatrix} m_3 d_2 \ddot{\theta}_1 - m_3 \left(\frac{a_3}{2} + a_1 \right) \dot{\theta}_1^2 + 2 m_3 \dot{d}_2 \dot{\theta}_1 + m_3 g s_1 + F_a \\ m_3 \left(\frac{a_3}{2} + a_1 \right) \ddot{\theta}_1 + m_3 d_2 \dot{\theta}_1^2 - m_3 \ddot{d}_2 + m_3 g c_1 + F_b \\ 0 \end{bmatrix} \tag{4.73} $$

$$ F_a = F_t C_{\theta b} C_{\beta} + F_n S_{\theta b} C_{\beta} \quad F_t S_{\theta b} S_{\beta} \quad F_n C_{\theta b} S_{\beta} + F_p c_{\theta e} c_{\beta'} \quad F_p s_{\theta e} s_{\beta'} \tag{4.74} $$

$$ F_b = +F_t C_{\theta b} S_{\beta} \quad F_n S_{\theta b} S_{\beta} \quad F_t S_{\theta b} C_{\beta} \quad F_n C_{\theta b} C_{\beta} \quad F_p c_{\theta e} s_{\beta'} \quad F_p s_{\theta e} c_{\beta'} \tag{4.75} $$

Equation (4.76) describes the general algorithm for this translation (Craig, 1996). And the reverse translated torque computed at joint-3 is given as equation (4.77).

$$ {}^{3}n_{3} = {}^{3}N_{3} + {}^{3}_{4}R\,{}^{4}n_{4} + {}^{3}P_{c3} \wedge {}^{3}F_{3} + {}^{3}P_{4} \wedge {}^{3}_{4}R\,{}^{4}f_{4} \tag{4.76} $$

$$ {}^{3}n_{3} = \begin{bmatrix} 0 \\ 0 \\ I_{zz3}\ddot{\theta}_1 \end{bmatrix} + \begin{bmatrix} 0 \\ 0 \\ 0 \end{bmatrix} + \begin{bmatrix} 0 \\ 0 \\ \frac{a_3}{2}\left(m_3\left(\frac{a_3}{2} + a_1\right)\ddot{\theta}_1 + m_3 d_2 \dot{\theta}_1^2 - m_3 \ddot{d}_2 + m_3 g c_1 \right) \end{bmatrix} \tag{4.77} $$

$$ + \begin{bmatrix} a3 \\ 0 \\ 0 \end{bmatrix} \wedge \begin{bmatrix} -F_t C_{\theta b} C_\beta + F_n S_{\theta b} C_\beta - F_t S_{\theta b} S_\beta - F_n C_{\theta b} S_\beta \\ +F_t C_{\theta b} S_\beta - F_n S_{\theta b} S_\beta - F_t S_{\theta b} C_\beta - F_n C_{\theta b} C_\beta \\ 0 \end{bmatrix} $$

The constant parameters in equation (4.77) can be simplified as equations (4.78) and (4.7).

$$ F_c = F_t C_{\theta b} C_\beta + F_n S_{\theta b} C_\beta \quad F_t S_{\theta b} S_\beta \quad F_n C_{\theta b} S_\beta \tag{4.78} $$

$$ F_d = +F_t C_{\theta b} S_\beta \quad F_n S_{\theta b} S_\beta \quad F_t S_{\theta b} C_\beta \quad F_n C_{\theta b} C_\beta \tag{4.79} $$

The equation (4.77) will modify into equations (4.80) and (4.81).

$$ {}^{3}n_{3} = \begin{bmatrix} 0 \\ 0 \\ I_{zz3}\ddot{\theta}_1 \end{bmatrix} + \begin{bmatrix} 0 \\ 0 \\ 0 \end{bmatrix} + \begin{bmatrix} 0 \\ 0 \\ \frac{a_3}{2}\left(m_3\left(\frac{a_3}{2} + a_1\right)\ddot{\theta}_1 + m_3 d_2 \dot{\theta}_1^2 - m_3 \ddot{d}_2 + m_3 g c_1 \right) \end{bmatrix} \tag{4.80} $$

$$ + \begin{bmatrix} a3 \\ 0 \\ 0 \end{bmatrix} \wedge \begin{bmatrix} F_c \\ F_d \\ 0 \end{bmatrix} $$

$$ {}^{3}n_{3} = \begin{bmatrix} 0 \\ 0 \\ I_{zz3}\ddot{\theta}_1 + m_3(a_1 \frac{a_3}{2} + \frac{a_3^2}{4})\ddot{\theta}_1 + m_3 \frac{a_3}{2} d_2 \dot{\theta}_1^2 - m_3 \frac{a_3}{2} \ddot{d}_2 + m_3 \frac{a_3}{2} g c_1 + a_3 F_d \end{bmatrix} \tag{4.81} $$

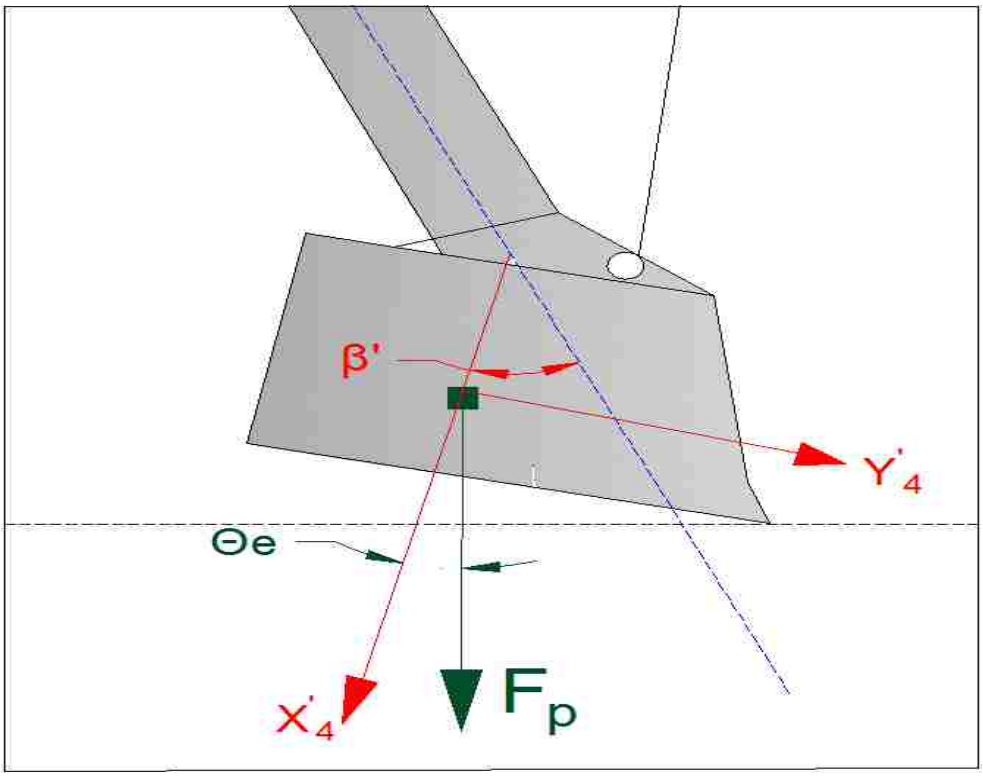

Figure 4.3. Payload and dipper weight forces

And similarly, the torque translation from the centroid of the dipper to the joint-3 is computed using algorithm in equation (4.82), while the resulting torque is given as equation (4.83).

$$ {}^{3}n'_{3} = {}^{3}N_{3} + {}^{3}_{4}R\,{}^{4}n_{4} + {}^{3}P_{c3} \wedge {}^{3}F_{3} + {}^{3}P'_{4} \wedge {}^{3}_{4}R\,{}^{4}f'_{4} \tag{4.82} $$

Where the primed parameters represent the calculations performed in our CF 4'.

$$ {}^{3}n'_{3} = \begin{bmatrix} 0 \\ 0 \\ a'_{3}\left(-F_{p}c_{\theta e}s_{\beta'} - F_{p}s_{\theta e}c_{\beta'}\right) \end{bmatrix} \tag{4.83} $$

As before, the constant parameters are combined into a single parameter given in equation (4.84).

$$\mathbf{F_e} = -\mathbf{F_p c_{\theta e} s_{\beta'}} - \mathbf{F_p s_{\theta e} c_{\beta'}} \tag{4.84}$$

$$^3n'_3 = \begin{bmatrix} 0 \\ 0 \\ a'_3 F_e \end{bmatrix} \tag{4.85}$$

The total combined torque at joint 3 (CF 3) is given as equation (4.86).

$$^3n_3 = \begin{bmatrix} 0 \\ 0 \\ I_{zz3}\ddot{\theta}_1 + m_3(a_1\frac{a_3}{2} + \frac{a_3^2}{4})\ddot{\theta}_1 + m_3\frac{a_3}{2}d_2\dot{\theta}_1^2 - m_3\frac{a_3}{2}\ddot{d}_2 + m_3\frac{a_3}{2}gc_1 + a_3F_d + a'_3F_e \end{bmatrix} \tag{4.86}$$

The same procedure is repeated to translate the forces and torque backward to the previous coordinate frame. Equations (4.87) and (4.89) represent the force translation to joint 2 (the translational joint at the crowd-arm and saddle-block junction).

$$^2f_2 = {}^3_2R\,{}^3f_3 + {}^2F_2 \tag{4.87}$$

$$^2f_2 = \begin{bmatrix} \left(m_3d_2 + m_2\frac{d_2}{2}\right)\ddot{\theta}_1 - \left(m_3\left(\frac{a_3}{2} + a_1\right) + m_2a_1\right)\dot{\theta}_1^2 \\ + 2\left(m_3 + m_2\right)\dot{d}_2\dot{\theta}_1 + \left(m_2 + m_3\right)gs_1 + F_a \\ 0 \\ \left(m_3\left(\frac{a_3}{2} + a_1\right) - m_2a_1\right)\ddot{\theta}_1 + \left(m_3d_2 - m_2\frac{d_2}{2}\right)\dot{\theta}_1^2 \\ + \left(m_2 - m_3\right)\ddot{d}_2 + \left(m_3 - m_2\right)gc_1 + F_b \end{bmatrix} \tag{4.88}$$

The resulting torque translation to joint-2 are represented in equation (4.89) and (4.90).

$$ {}^{2}n_2 = {}^{2}N_2 + {}^{2}_{3}R^{3}n_3 + {}^{2}P_{c2} \wedge {}^{2}F_2 + {}^{2}P_3 \wedge {}^{2}_{3}R^{3}f_3 \tag{4.89} $$

$$ {}^{2}n_2 = \begin{bmatrix} 0 \\ I_{yy2}\ddot{\theta}_1 \\ 0 \end{bmatrix} + \tag{4.90} $$

$$ \begin{bmatrix} 0 \\ I_{zz3}\ddot{\theta}_1 + m_3(a_1\frac{a_3}{2} + \frac{a_3^2}{4})\ddot{\theta}_1 + m_3\frac{a_3}{2}d_2\dot{\theta}_1^2 \quad m_3\frac{a_3}{2}\ddot{d}_2 + m_3\frac{a_3}{2}gc_1 + a_3F_d \quad + a_3F'_e \\ 0 \end{bmatrix} $$

$$ + \quad \begin{bmatrix} 0 \\ m_2a_1\frac{d_2}{2}\dot{\theta}_1^2 + 2m_2\frac{d_2}{2}\dot{d}_2\dot{\theta}_1 + m_2\frac{d_2}{2}\frac{d_2}{2}\ddot{\theta}_1 + m_2\frac{d_2}{2}gs_1 \\ 0 \end{bmatrix} + $$

$$ \begin{bmatrix} 0 \\ m_3d_2d_2\ddot{\theta}_1 \quad m_3d_2\left(\frac{a_3}{2} + a_1\right)\dot{\theta}_1^2 + 2m_3d_2\dot{d}_2\dot{\theta}_1 + m_3d_2gs_1 + d_2F_a \\ 0 \end{bmatrix} \text{`} $$

The equation (4.90) can be simplified as equation (4.91).

$$ {}^{2}n_2 = \begin{bmatrix} 0 \\ \left(I_{yy2} + I_{zz3}\right)\ddot{\theta}_1 + \left(m_3(a_1\frac{a_3}{2} + \frac{a_3^2}{4} + d_2^2) + m_2\frac{d_2^2}{4}\right)\ddot{\theta}_1 \\ 0 \end{bmatrix} \tag{4.91} $$

$$ + \begin{bmatrix} 0 \\ \left(-m_2a_1\frac{d_2}{2} - m_3a_1d_2\right)\dot{\theta}_1^2 \\ 0 \end{bmatrix} $$

$$ + \begin{bmatrix} 0 \\ -m_3\frac{a_3}{2}\ddot{d}_2 + 2\left(m_2\frac{d_2}{2} + m_3d_2\right)\dot{d}_2\dot{\theta}_1 \\ 0 \end{bmatrix} $$

$$ + \begin{bmatrix} 0 \\ m_3\frac{a_3}{2}gc_1 + \left(m_2\frac{d_2}{2} + m_3d_2\right)gs_1 + d_2F_a + a_3F_d + a'_3F_e \\ 0 \end{bmatrix} $$

Finally, the resultant backward translated force to the first joint (the rotational joint of the saddle block) is computed using algorithm of equation (4.92) and is given as equation (4.93).

$$ {}^{1}f_1 = {}^{2}_{1}R\,{}^{2}f_2 + {}^{1}F_1 \tag{4.92} $$

$$ {}^{1}f_1 = \begin{bmatrix} \left(m_2\frac{d_2}{2} + m_3 d_2\right)\ddot{\theta}_1 - \left(m_1\frac{a_1}{2} + m_2 a_1 + m_3\left(\frac{a_3}{2} + a_1\right)\right)\dot{\theta}_1^2 \\ + 2\left(m_2 + m_3\right)\dot{d}_2\dot{\theta}_1 + \left(m_1 + m_2 + m_3\right)gs_1 + F_a \\ \left(m_1\frac{a_1}{2} - m_2 a_1 + m_3\left(\frac{a_3}{2} + a_1\right)\right)\ddot{\theta}_1 + \left(m_2\frac{d_2}{2} + m_3 d_2\right)\dot{\theta}_1^2 \\ + \left(m_2 - m_3\right)\ddot{d}_2 + \left(m_1 + m_2 + m_3\right)gc_1 + F_b \\ 0 \end{bmatrix} \tag{4.93} $$

Equation (4.93) represents the force that must be provided at the first joint to overcome all the resistive forces including the formation excavation and payload forces.

Similarly, the required torque at the first joint is given by equations (4.94) and (4.95).

$$ {}^{1}n_1 = {}^{1}N_1 + {}^{1}_{2}R\,{}^{2}n_2 + {}^{1}P_{c1} \wedge {}^{1}F_1 + {}^{1}P_2 \wedge {}^{1}_{2}R\,{}^{2}f_2 \tag{4.94} $$

$$ {}^{1}n_1 = \begin{bmatrix} 0 \\ 0 \\ \left(\left(I_{zz1} + I_{yy2} + I_{zz3}\right) + m_1\frac{a_1^2}{4} + m_2\left(\frac{d_2^2}{4} - a_1^2\right) - m_3\left(a_1^2 - \frac{a_3^2}{4} - d_2^2\right)\right)\ddot{\theta}_1 \end{bmatrix} + \begin{bmatrix} 0 \\ 0 \\ -2m_3 a_1 d_2 \dot{\theta}_1^2 \end{bmatrix} \tag{4.95} $$

$$+\begin{bmatrix} 0 \\ 0 \\ 2\left(m_2\frac{d_2}{2}+m_3d_2\right)\dot{d}_2\dot{\theta}_1 \end{bmatrix}$$

Finally, the inertial force and torque equations for the crowd-arm can be written as equation (4.96).

$$F_1=\begin{bmatrix} \left(m_2\frac{d_2}{2}+m_3d_2\right)\ddot{\theta}_1-\left(m_1\frac{a_1}{2}+m_2a_1+m_3\left(\frac{a_3}{2}+a_1\right)\right)\dot{\theta}_1^2+2(m_2+m_3)\dot{d}_2\dot{\theta}_1+(m_1+m_2+m_3)gs_1+F_a \\ \left(m_1\frac{a_1}{2}-m_2a_1+m_3\left(\frac{a_3}{2}+a_1\right)\right)\ddot{\theta}_1+\left(m_2\frac{d_2}{2}+m_3d_2\right)\dot{\theta}_1^2+(m_2-m_3)\ddot{d}_2+(m_1+m_2+m_3)gc_1+F_b \\ 0 \end{bmatrix} \quad (4.96)$$

$$\begin{aligned} \tau_1 = \quad & \left(\left(I_{zz1}+I_{yy2}+I_{zz3}\right)+m_1\frac{a_1^2}{4}+m_2\left(\frac{d_2^2}{4}-a_1^2\right)-m_3\left(a_1^2-\frac{a_3^2}{4}-d_2^2\right)\right)\ddot{\theta}_1 \\ & -2m_3a_1d_2\dot{\theta}_1^2+2\left(m_2\frac{d_2}{2}+m_3d_2\right)\dot{d}_2\dot{\theta}_1-\left((m_2-m_3)a_1+m_3\frac{a_3}{2}\right)\ddot{d}_2 \\ & +\left(m_1\frac{a_1}{2}-m_3\left(a_1-\frac{a_3}{2}\right)+a_1m_2\right)gc_1+\left(m_2\frac{d_2}{2}+m_3d_2\right)gs_1+d_2F_a-a_1F_b+a_3F_d+a_3'F_e \end{aligned} \quad (4.97)$$

If the $\{d\ \theta\}^T$ is assumed to represent the Θ of equation (4.49). Then the equations (4.96) and (4.97) can be arranged to represent the general form for the dynamic model of the cable shovel as given in equation (4.49).

The equation (4.98) defines the reverse dynamic model of cable shovel front-end assembly. This model includes the external resistive forces acting on the teeth and the dynamic forces of payload and weight of the dipper. The model, once properly programed, can compute quickly the hoisting torque and crowd force requirements for the cable shovel dipper.

$$\begin{Bmatrix} F_1 \\ \tau_1 \end{Bmatrix} = \begin{bmatrix} 0 & \left(m_2\frac{d_2}{2}+m_3 d_2\right) \\ -\left(\left(m_2-m_3\right)a_1+m_3\frac{a_3}{2}\right) & \left(I_{zz1}+I_{yy2}+I_{zz3}\right)+m_1\frac{a_1^2}{4}+m_2\left(\frac{d_2^2}{4}-a_1^2\right)-m_3\left(a_1^2-\frac{a_3^2}{4}-d_2^2\right) \end{bmatrix} \begin{Bmatrix} \ddot{d}_2 \\ \ddot{\theta}_1 \end{Bmatrix} \quad (4.98)$$

$$+\begin{bmatrix} 2\left(m_2+m_3\right)\dot{\theta}_1 & -\left(m_1\frac{a_1}{2}+m_2 a_1+m_3\left(\frac{a_3}{2}+a_1\right)\right)\dot{\theta}_1 \\ 2\left(m_2\frac{d_2}{2}+m_3 d_2\right)\dot{\theta}_1 & -2m_3 a_1 d_2\dot{\theta}_1 \end{bmatrix} \begin{Bmatrix} \dot{d}_2 \\ \dot{\theta}_1 \end{Bmatrix}$$

$$+\begin{bmatrix} \left(m_1+m_2+m_3\right)gs_1 \\ \left(\left(\frac{m_2}{2}+m_3\right)gs_1\right)+\left(m_1\frac{a_1}{2}-m_3\left(a_1-\frac{a_3}{2}\right)+a_1 m_2\right)gc_1 \end{bmatrix} \begin{Bmatrix} d_2 \\ \theta_1 \end{Bmatrix}$$

$$+\begin{bmatrix} F_a \\ F_a - a_1 F_b + a_3 F_d + a_3' F_e \end{bmatrix}$$

The crowd force and hoisting torque are the two most important parameters for shovel excavation. Their accurate estimation is critical for a digging operation and the shovel power packs must be able to provide these two components to overcome resistive forces. The variation in the soil/rock parameters can greatly alter the force and torque requirements for the shovel. Introducing a shovel without a prior estimation of crowd force and hoist requirements can be detrimental to shovel health and longevity. The dynamic model can be quickly analyzed to foresee the impacts of these variations on shovel components without compromising the health of shovel and avoid any severe stress loading of the shovel components. The dynamic model, along with the crowd and hoisting forces, also computes the torques and forces for every individual link in the shovel. Computing these will further help estimate stress loading of shovel components.

Shovel energy requirements are directly linked with crowding and hoisting forces. Shovel energy requirements can be optimized for an energy efficient excavation (Awuah-Offei, 2007). The shovel energy profile can also be used for operator efficiency measure (Frimpong, 2008). The energy requirements have a major impact on the shovel excavation

costs. As was discussed in Section 2, excavation and loading costs constitute the major component of mining operation where truck and shovel system is used as a primary excavation system.

4.3. SUMMARY OF THE MATHEMATICAL MODEL

A Kinematic and dynamic model of the shovel is built in this section using the Newton-Euler iterative algorithm. The Newton-Euler iterative approach is considered superior over the other methods because of its ease for computer implementation. Both the forward and reverse kinematic and dynamic models are constructed. Forward models start from the joint at the saddle block and terminate at the dipper tip, while the reverse models do the opposite. Kinematic model computes the position, rotation and velocities for every link and joint in the mechanism. The kinematic model forms the basis for dynamic model as the forces and torques are computed in the dynamic model. The forces and torques require the linear and rotational accelerations, in respective order, and can be computed either by time integration of the velocities computed in the kinematic model or using the fundamental robotics relationship.

For this research the reverse dynamic model is needed that incorporates the formation resistive and payload forces. The forces are iteratively computed from the dipper-tip to the joint at the saddle block. The forces acting on every individual component, joint and link, of the shovel front-end component is computed during the formulation of reverse dynamic model. This iterative nature of the Newton-Euler algorithm is helpful to investigate the stress loading of the individual component. Equation (4.98) is the culminating equation for the dynamic model as it computes the all-important crowd force and hoisting torque required to overcome the resistive forces.

5. NUMERICAL MODELING AND VIRTUAL PROTYPING OF DIPPER FORMATION INTERACTION

The next logical step, in sequence, is to make a scheme to solve the mathematical model of the shovel dipper-teeth problems and generate useful outputs for the virtual prototype and fatigue modeling. The mathematical model, developed in Section 4, is solved numerically in MATLAB and Simulink environments. This part of simulation generated the resistive excavation forces acting on the shovel during the excavation process, and the resulting torque and moment at the shovel saddle point required to overcome the resistive forces. A 3D virtual prototype of the shovel's dipper-teeth assembly is created in AutoCAD (Autocad, 2012) and ANSYS Designmodeler softwares (ANSYS, 2014a). The transient structural simulations are performed in ANSYS Workbench (ANSYS, 2014a) to compute the stress loading of the shovel's dipper-teeth assembly in response to the excavation resistive forces. Small cracks are introduced at various locations of the shovel dipper and simulations are performed to compute the stress intensity factors around these cracks. This section describes the detailed design and workflow for the numerical and virtual prototype simulations conducted for this research.

5.1. NUMERICAL SIMULATIONS FOR SHOVEL'S DYNAMIC MODEL

The dynamic modeling effort for the shovel dipper-teeth assembly in Section 4 resulted in equation (4.98). This dynamic model is a system of ordinary differential equations (ODEs). The model is a result of an iterative process and includes a number of sub-processes involving linear and ODEs. MATLAB R2012a and Simulink (Stavropoulou et al., 2013) are used as platforms to build routines and sub-systems to completely describe the motions, forces and torques of the shovel's components.

MATLAB/Simulink platform is selected because it provides a greater ease and efficiency to build numerical routines and it has a vast library of numerical algorithms for a comprehensive modeling of complex processes.

The dynamic model equations (ODEs) are numerically solved in Matlab/Simulink using the embedded Runge-Kutta algorithm. MATLAB offers a number of solver options for ODEs (MathWorks, 2012). The suitability of these options overlap based on the complexity of ODEs and one can get similar results from two or more options. The common and general purpose solver are ode45 and ode23. For this simulation ode45, with a variable time-step, is used to provide algorithms to the ODE models.

The solution process is explained in the Figure 5.1. This simulation model consists of MATLAB programs (.m files) and Simulink design based models and sub-models. The simulation model consists of the main model and four sub-models. These sub-models define the dipper's trajectory, the crowd-arm extension and rotation, and the resistive forces (cutting forces, material and dipper's weight) on the dipper.

5.1.1. Test Bench Geometry and Trajectory Sub-model. A representative bench geometry is created for this simulation and is illustrated in Figure 5.2. The bench face-angle for this geometry is set at 80^{o} and the bench height is 15.25 m (50 ft), which are typical of P&H 4100 XPC shovel operation. The digging cycle starts at the toe of the bench and finishes at the crest of the bench in 3 seconds. The depth of cut is selected in such a way that the dipper is completely filled as it reaches the crest of the bench in 3 seconds without any spillage of material. Generally, the dipper is filled before it reaches the crest and leaves a crown at the crest of the bench, which falls under gravity because of its weight and lack of support. The 3-second simulation period is selected to compare results with and lack of support. The 3-second simulation period is selected to compare

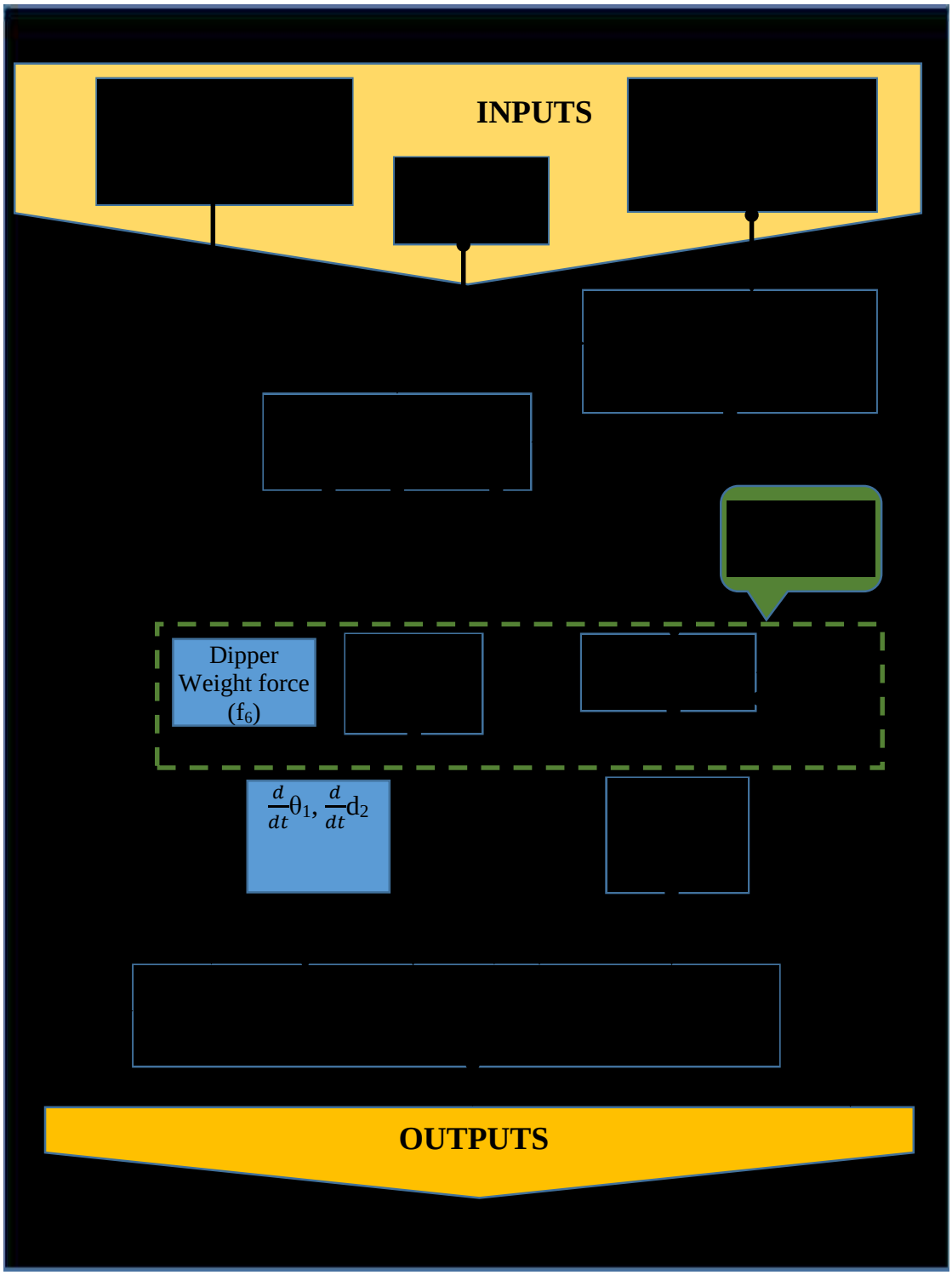

Figure 5.1. Flowchart of simulation model

results with some of the earlier research (Awuah-Offei and Frimpong, 2006; Awuah-Offei et al., 2009; Frimpong et al., 2008) for model.

The characteristics for the excavated material can be selected for various digging conditions. A simulation step size is selected based on the reason that the dipper covers equal vertical distance in each step. This condition is selected to make the dipper move with a constant linear velocity as suggested by the field experimental results of Hendricks and Scoble (1990). The shape of the failure surface could vary depending upon the

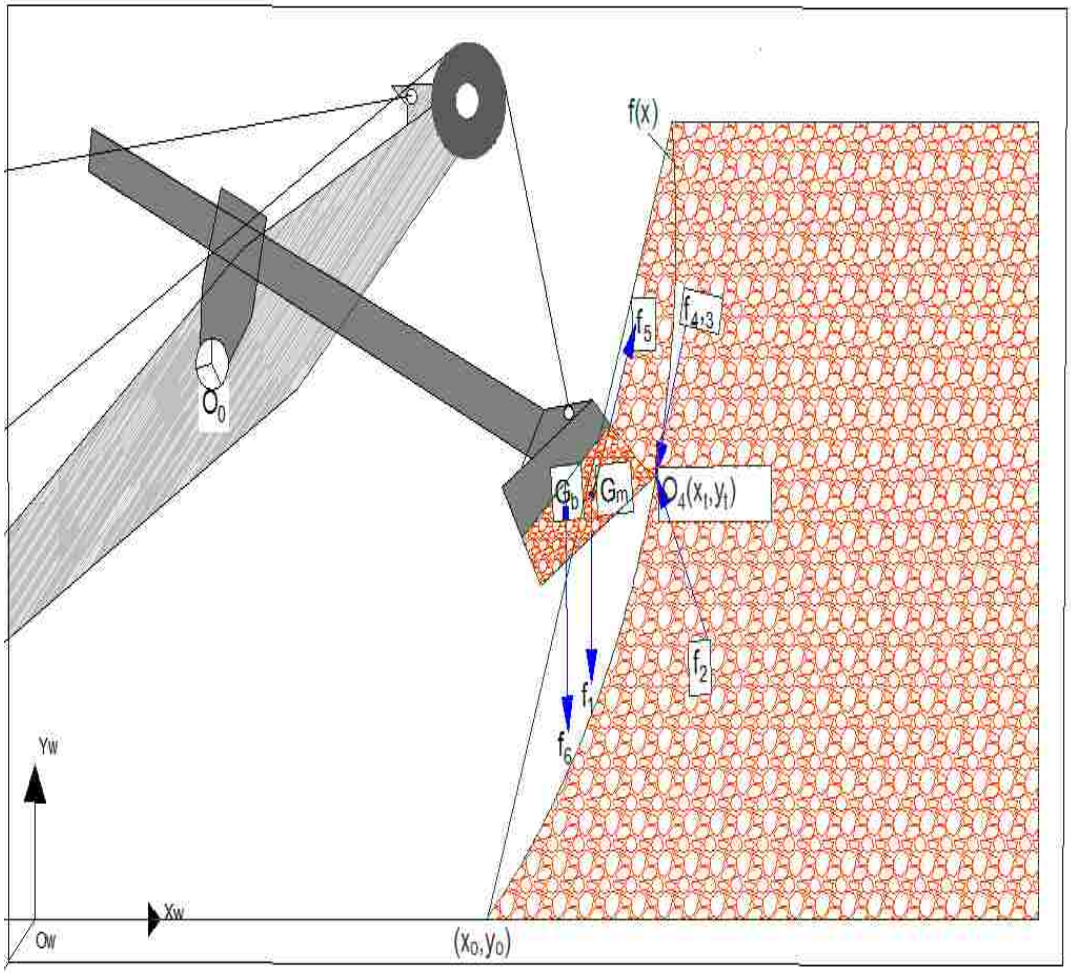

Figure 5.2. Representative bench geometry

material. A curved failure plane was assumed by Awuah-Offei et al. (2009), Hemami (1994), and Takahashi et al. (1999) while Irwin (1957) used a combination of log-spiral and straight line to model the crack surface. In this research study, a curved crack surface trajectory is assumed which is shown in Figure 5.3 and modeled as a quadratic equation (5.1) through a curve fitting process in MATLAB R2012a.

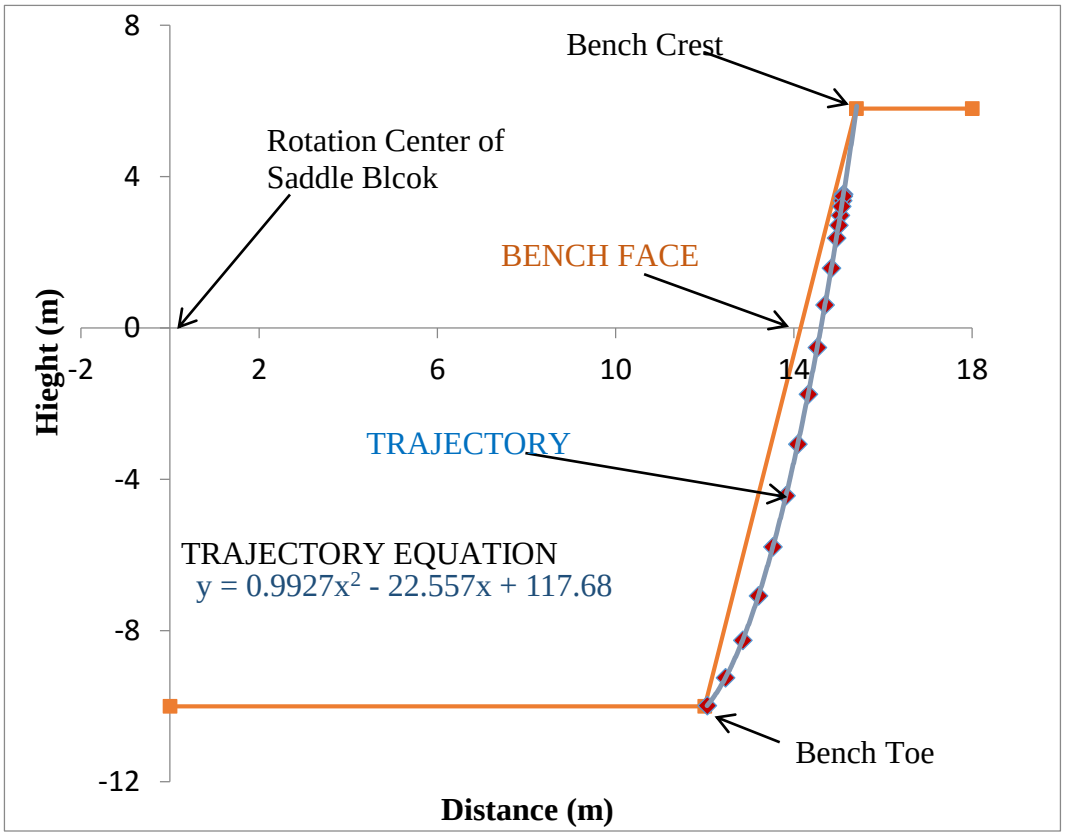

Figure 5.3. Dipper trajectory modeling

$$y = 0.9927x^2 - 22.557x + 117.68 \quad (5.1)$$

During the simulation process the coordinates of the dipper tip ($O_4(x,y)$) and the dipper depth into the working bench (d) are continuously computed at every time step

using equations (5.2) and (5.3) respectively. The trajectory generated in MATLAB, using equation (5.2), is shown in Figure 5.4.

$$O_4[x, y] = [-0.4837t^2 + 2.4351t + 12.053, \quad 0.9927 * x^2 - 22.557 * + 117.68] \tag{5.2}$$

$$d = O_4(y) - O_4(x) \tag{5.3}$$

5.1.2. Crowd-arm Extension and Rotation Angle Sub-model. A sub-model is used to calculate the crowd-arm extension (d_2) and rotation (θ_1) using equations (4.35) and (4.48). The trajectory coordinates, from the trajectory sub-model, are used as input to these equations. Both d_2 and θ_1, and their higher derivatives, are important input parameters for the crowd-arm force and torque calculations. The crowd-arm extension and rotation are plotted in Figure 5.5.

5.1.3. Payload and Force f_1 Sub-models. The payload is calculated as a separate sub-system. This sub-system forms the basis for the important dynamic payload force (f_1) inside the dipper. As shown in Figure 5.2, the dipper trajectory is defined in such a way that the dipper is completely filled as it leaves the bank without any material spillage. At any instant, therefore, the payload is equivalent to the area under the trajectory curve. At each simulation step the (x, y) coordinates of the trajectory are computed and the area excavated (A_c) is numerically computed using equation (5.4). MATLAB R2012a has built-in routines for numerical integration, and are used for this calculation. This area is then used to calculate the force (f_1) due to the payload weight.

$$A_c = \frac{1}{2}(x_t - x_o)^2 tan\alpha - \int_{x_o}^{x_t} f(x)\, dx \tag{5.4}$$

$$f_1 = A_c \omega \rho g \tag{5.5}$$

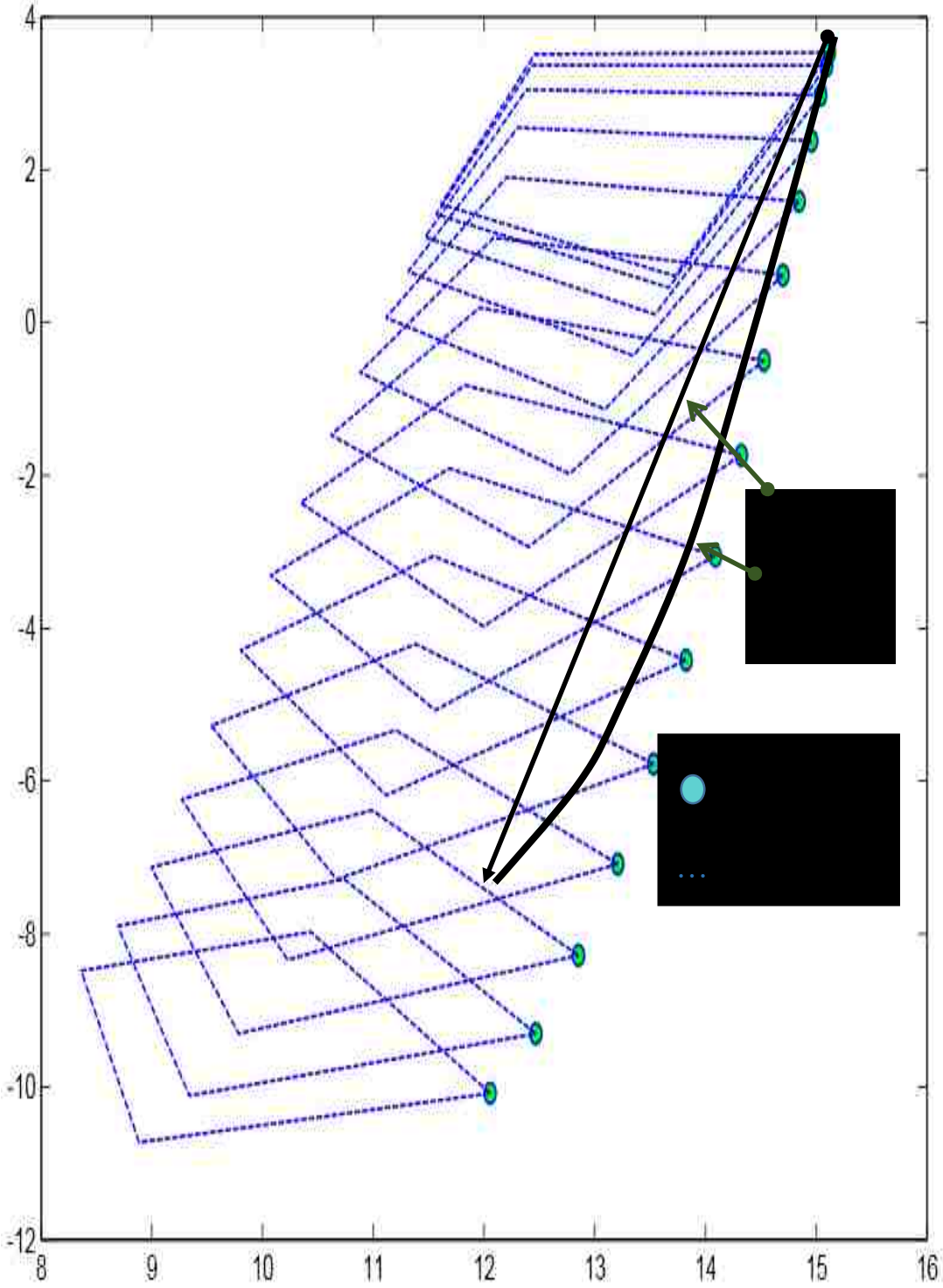

Figure 5.4. Trajectory definition in MATLAB/Simulink

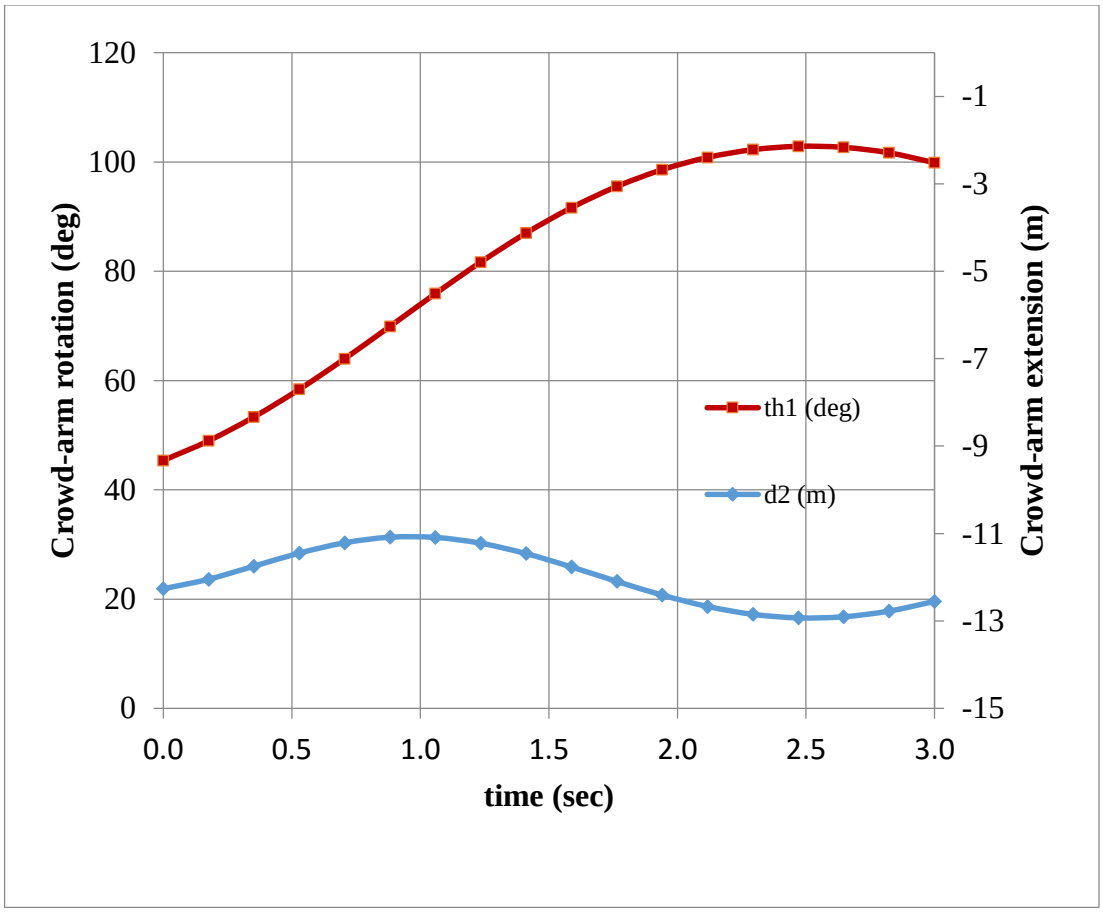

Figure 5.5. Crowd-arm extension (d_2) and rotation (th_1)

An optimization algorithm by Awuah-Offei et al. (2009) is used to define the geometry of the filled payload. This geometry is based on the material distribution suggested by Hemami (1994). In this method a suitable polygonal geometry is determined that fills the dipper based on the area of material excavated. The centroid for each material geometry, a polygon, inside the dipper is computed using the algorithm developed by Sommer III (2011) in equation (5.6). This centroid is a dynamic point and is used as the point of application for the dynamic force f_1. The geometry of the material loaded into the dipper and the centers of mass for material and dipper are shown in Figure 5.6. This force

(f_1) is computed continuously at every instant of the excavation process. The payload force is shown in Figure 5.7.

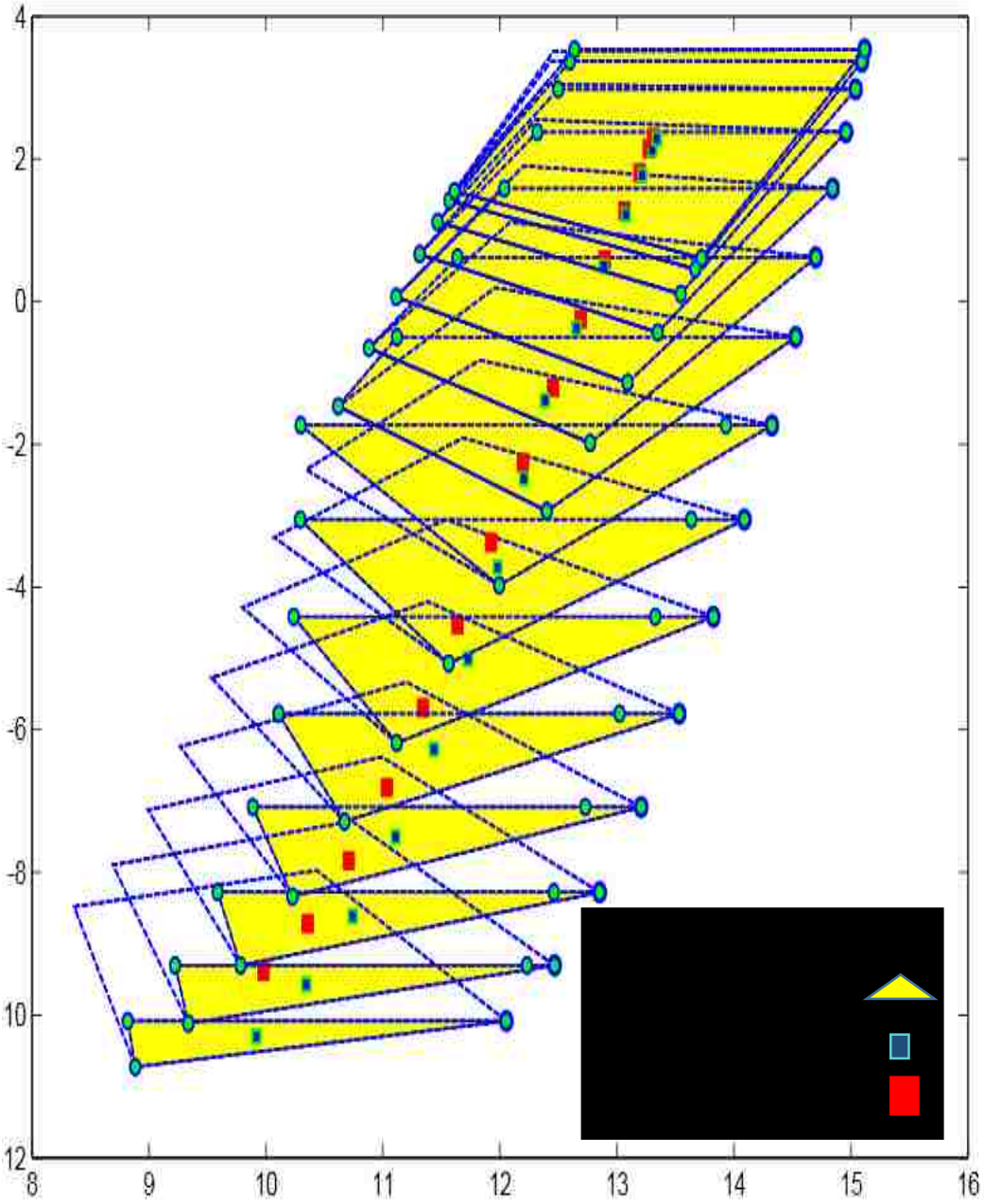

Figure 5.6. Material geometry modeling of payload

$$\frac{x_{Gm} = \frac{\iint x dx dy}{\iint dx dy}}{y_{Gm} = \frac{\iint y dx dy}{\iint dx dy}} \quad (5.6)$$

5.1.4. Material Resistive Force f_6 Sub-model. The force due to the weight of the dipper is continuously calculated throughout the digging cycle along the trajectory. The weight of the dipper is computed using the dimensions of the dipper and the material properties and is shown in Figure 5.7. The gravity center of the dipper is determined using the algorithm developed by Sommer III (2011) in a 2D plane. Both the dimensions and centroid location for the dipper are shown in Figure 5.6**.**

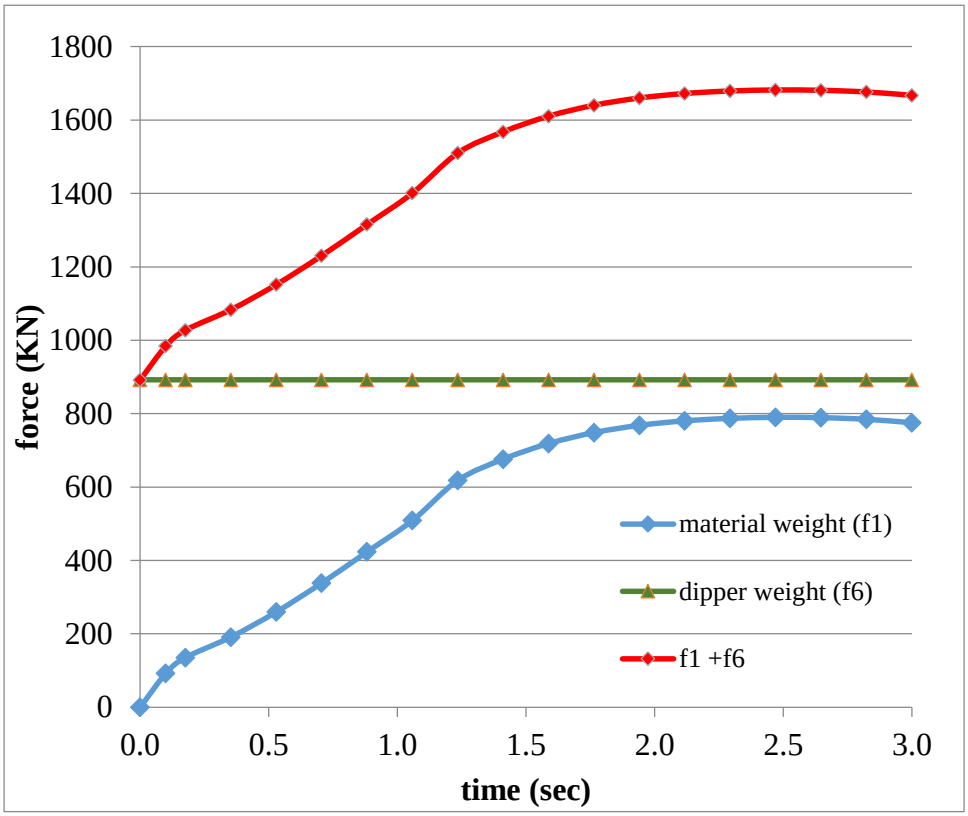

Figure 5.7. Forces due to weights of dipper and payload (f_1 & f_6)

As determined from the Figure 5.6, the centroid of the dipper and the payload coincide closely as the dipper is filled with the material. At the start of the digging cycle, the two centroids are a little far apart. Because, the payload force is smaller at the start of digging cycle, the centroid of the dipper is used as the common point of application for both f_1 and f_6.

5.1.5. Digging Resistive Forces f_3 and f_4 Sub-models. For the resistive forces, f_3 and f_4, the model developed by Zelenin et al. (1985) is used to measure the resistive forces on a bucket with teeth. Both forces are combined as a single resistive force (F_r) and thus represents the total force of dipper. This force is discussed in detail in Section 2 and is given as equation (2.7). The cutting force (F_r) acts along the tangent of the trajectory at the dipper tip. This force is resolved into its rectangular components, one along the dipper base and the other normal to it. These tangent and normal components (F_t and F_n respectively) of the resistive force (F_r) are computed at every trajectory point in this sub-model.

5.1.6. The Main Model and Numerical Simulation. The dynamic model of the dipper-teeth assembly is solved in the main model. The outputs from all the sub-models, along with system constants and time-steps are fed into the main model as inputs. The main model then numerically solves the mathematical model and generates the desired outputs. Two of the important results or outputs from this solution are the hoisting force (F_1) and crowd-arm torque (T_1). These two results and the components of the hoisting force (F_{1x} and F_{1y}) are shown in Figure 5.8. Other than these outputs, the solution of the simulation model generates an important wealth of data including individual joint torques, joint forces, velocities, and accelerations. This information can be used to test the model against a number of field conditions (e.g., bench geometry, digging cycle-time,

dipper filling etc.) and environmental variables (e.g., density of material, and fragmentation size).

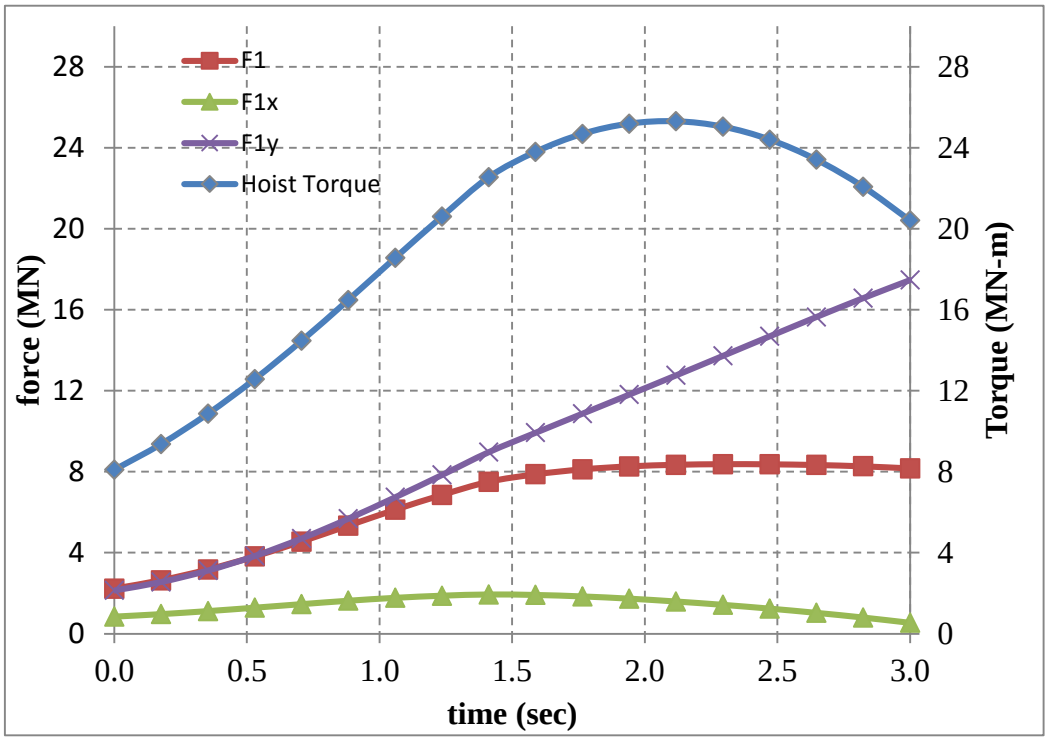

Figure 5.8. Crowd force and hoist torque required for shovel digging cycle

During this numerical simulation process, four of the six resistive forces (f_1, f_3, f_4, f_6) are computed as separate sub-systems, while the other two resistive forces (f_2 and f_5) are set to zero. The resistive force f_2 is set to zero by selecting an appropriate trajectory of the dipper (Hemami, 1994). The excavation trajectory is selected in such a way that the dipper stays clear off the material and does not compress the material. This assumption is reasonable in the sense that it involves proper bench geometric design and operator's skill. An improper bench geometric design would lead to undue stresses on the

shovel, which must be avoided during the excavation process. The force f_5 represents the inertia forces for the dipper and the payload. This force can be set to zero if the dipper moves through the material with a constant velocity and hence with zero acceleration. For this research, it is assumed that the dipper moves through the bench with a constant velocity and hence a zero acceleration. This assumption is consistent with the field observations by Hendricks and Scoble (1990) for hoist rope extension and is maintained by Frimpong et al. (2005) and Hemami (1994). The constant velocity is maintained by dividing the trajectory into equal vertical distance steps travelled in equal time intervals.

5.2. MODEL VERIFICATION

The results must be verified and validated, before they are used as input to the virtual prototyping. One way of doing this is to compare the results against the known values to check if the model produces the desired results. A systematic but simple step-by-step approach is adopted for the model verification purposes. The dynamic model is simulated in MATLAB/Simulink using a number of sub-systems. P&H4100XPC shovel is used as a base shovel model for verification purposes. Shovel dimensions are measured from scaled diagram and are given in Table 5.1.

5.2.1. Trajectory Path and Coordinate Transformation. The dipper's trajectory path is given as an input to the model and is shown in Figure 5.2. The coordinate transformation is checked analytically using Microsoft Excel. The known lengths of the crowd-arm extension and rotation are given as an input to determine the dipper-end coordinates. And conversely, the dipper extension and rotation were determined against the known dipper end coordinates and rotation. The coordinates and dimensions matched perfectly in both cases.

Table 5.1. P&H 4100XPC Shovel Dimensions

Dipper Capacity (m^3)	28.44
Dipper Inner Width (m)	4.6241
Mass of Dipper (kg) (link 3)	14802
Mass of Crowd-arm (kg)	40134
Mass of Saddle Block (kg)	16207
Saddle Block Length (m)	1.1162
Length from Crowd-Arm to Dipper-Lip (m)	3.3004

The bench geometry is given as an input to the dynamic system. The dipper is filled as it moves towards the crest of the bench and it is completely filled by the time it reaches the crest. The dipper movement and the material filling processes are verified graphically by plotting the dipper corner coordinates and the material polygon inside the material. The results are shown in Figure 5.4 and Figure 5.6. As can be seen in both cases, the results show an exact match of dipper's dimensions and trajectory profile.

5.2.2. Digging Force. The digging force is calculated using the cutting force model suggested by Zelenin et al. (1985) model and is discussed in the sub-system 2.2. The parameters are given in Table 5.2. To compare the results, the force is analytically computed at a time when the shovel dipper is horizontal with ground. The resistive force in this situation is calculated, analytically, as 45.6 KN. That particular time is calculated as 1.52 seconds from Figure 5.5. The force calculated by the force sub-system at 1.52sec is 45.8KN. The two values match closely. The material resistive forces acting on the dipper are shown in Figure 5.9. These forces are similar in magnitude to the results reported by Awuah-Offei et al. (2009).

Table 5.2. Digging Forces Parameters for Zelenin et al. (1985)

C_o =	10
With of dipper = w =	4.6241 m
z =	1.2

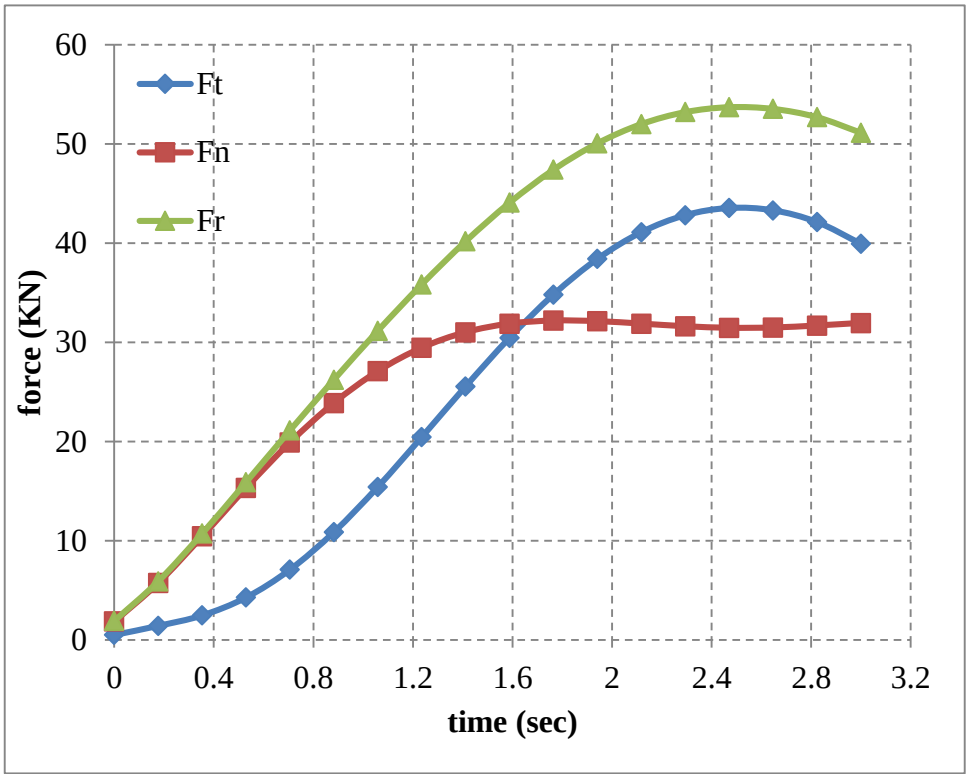

Figure 5.9. Material resistive forces acting on the dipper

5.3. SHOVEL VIRTUAL PROTOTYPING

A virtual 3D prototype of the shovel is built in AutoCAD-2012 and is shown in Figure 5.10. The dimensions of the shovel front-end assembly are chosen to represent the dimensions of P&H 4100 XPC shovel and are measured from a scaled model (P&H,

2012). The front-end geometry is simplified to avoid unnecessary geometric complications. For example, the ore-release door is considered fixed to the dipper, the

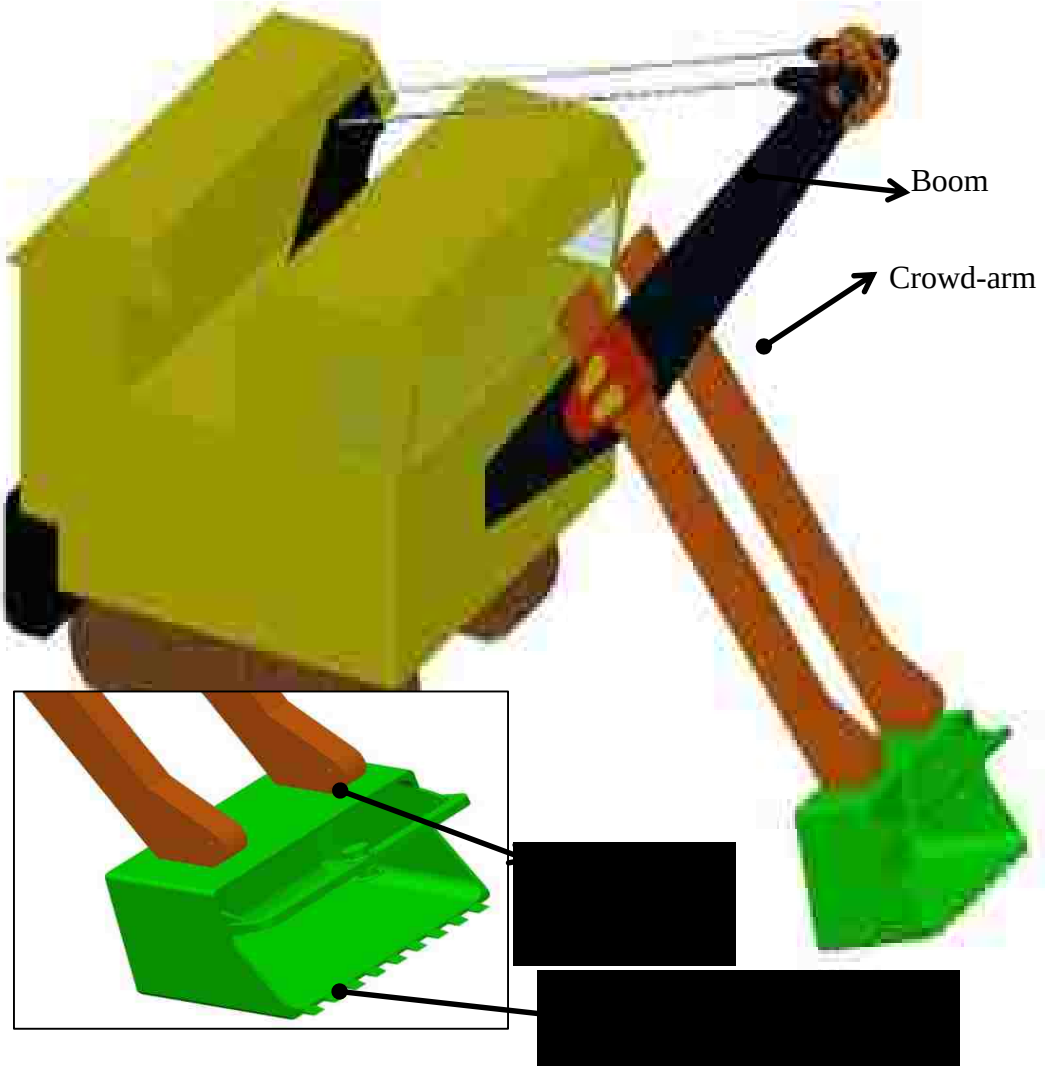

Figure 5.10. A simplified 3D model of cable shovel and dipper

teeth are considered fixed to the dipper lip. The assumption for the fixed door is justified as it stays closed throughout the digging phase. This assumption helps avoid the inclusion

of door's trip mechanism and associated parts into the mechanical model and the simulation process.

This research is intended to model the stress loading and fatigue failure of the dipper and teeth assembly. Therefore, the exclusion of the components is justified. The teeth are modeled as fixed to the front-end lip of the dipper. In reality, the teeth are attached through the adaptors and need regular replacements. Sometimes, the teeth are welded together to avoid any lateral movement, which justifies the fixed teeth assumption. The simplified 3D model of the dipper is shown in Figure 5.10. The CAD model is then transferred to the ANSYS/Workbench R15.0 (ANSYS, 2014a) using IGES (Initial Graphics Exchange Specification) format. The transferred geometric model is linked as a live model in ANSYS/Workbench for FEM based stress analysis.

The shovel dipper-teeth assembly is symmetric in the vertical plane. Therefore, a symmetry plane is defined at the mid-plane of the crowd-arm and intersecting the boom, saddle and dipper. This symmetric plane reduces the number of elements for FEM and hence the computation cost. The imported geometric model contains many geometric flaws. Therefore, the model is cleaned before meshing. Further, to reduce the number of elements, a process of slicing and dicing is used. The sides of the dipper are sliced into individual components. This whole slicing and dicing process resulted in more sweepable bodies for efficient meshing and resulted in a smoother mesh as shown in Figure 5.13.

5.3.1. Contacts and Boundary Conditions. The model consists of two moving joints that control the positioning of the dipper into the working bench. These contacts are appropriately modeled in the ANSYS Workbench software and are shown in the Figure 5.11.One revolute joint between the saddle and boom and one prismatic joint between the dipper-handle and saddle block control the crowding and digging actions of

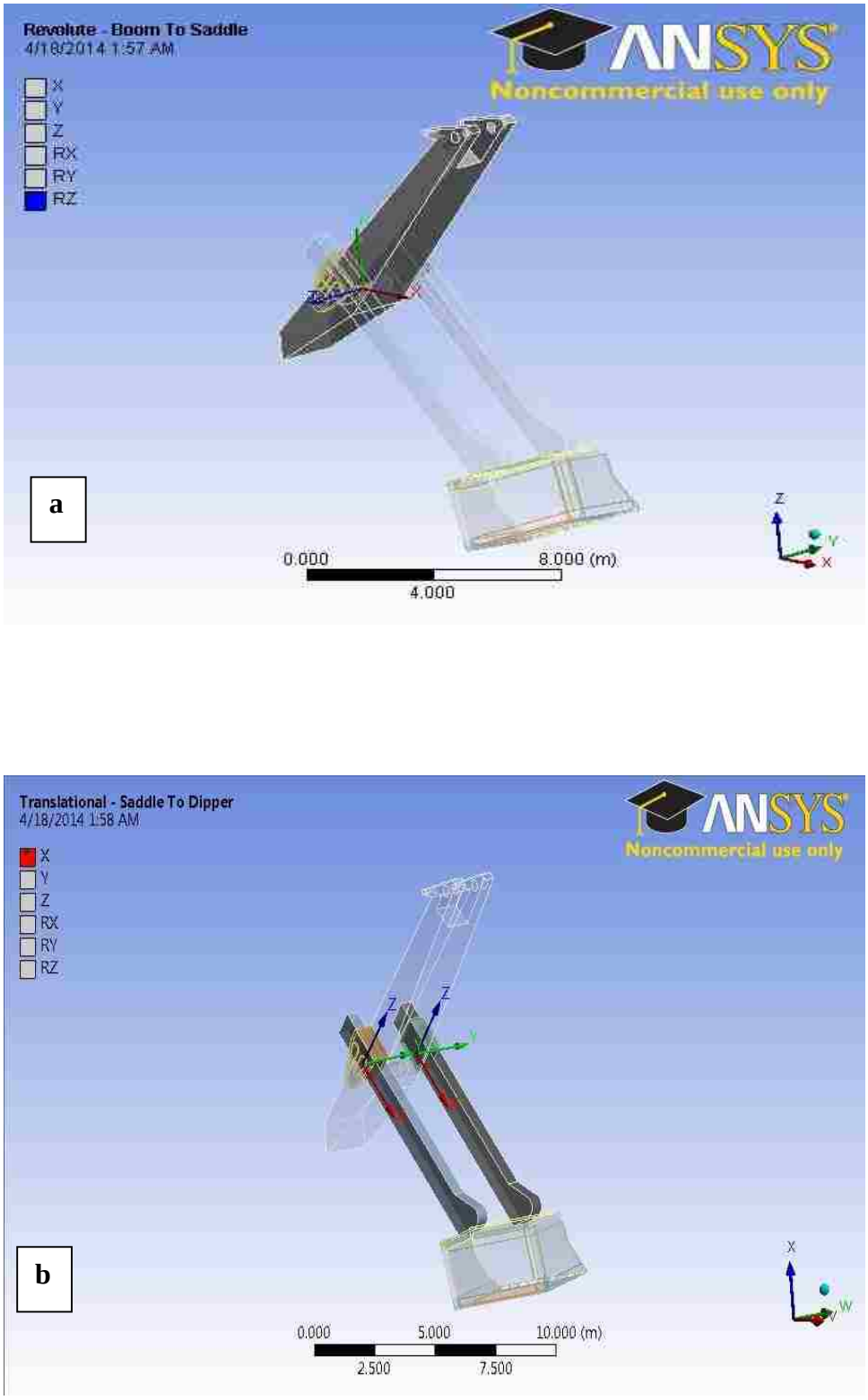

Figure 5.11. Joints definition of shovel front-end a) revolute b) prismatic

the dipper. The motions are restricted by applying stop constraints on these three joints. The revolute joint is restricted in the vertical plane for angular motion, whereas the prismatic joint is restricted in a way that the dipper-handle never leaves the saddle. These constraints preserve the integrity of the allowable dipper trajectories and movements. The dipper is fixed to the crowd-arm and the teeth are fixed to the dipper.

The boom and saddle are modeled as rigid bodies. The boom is considered fixed to the ground. The revolute joint allows rotation only around the z-axis. The two prismatic joints allow motion along the x-axis only. The resistive forces of the formation are applicable as a remote force available at the teeth. The material force is also modeled as remote forces acting on the dipper. The revolute joint is given a fixed rotation every time step to ensure the completion of the digging cycle in 3 seconds. The contacts and boundary conditions are shown in Figure 5.12.

5.3.2. Element Types and Mesh Generation. The mesh size (number of elements per body) is a very critical factor in stress analysis as it is directly linked with the accuracy of the results and computation time. A very coarse mesh will need lesser computational resources. However, the results might not be accurate. A very fine mesh, on the other hand, might produce better results. However, the computation time can be very high. Smoothness and connectivity of mesh across geometric bodies are also equally important and critical factors. ANSYS Workbench meshing tools provide a way to balance the mesh size and accuracy. ANSYS Workbench provides a large library of element types for meshing and a number of tools to control the mesh size (ANSYS, 2014b).

To control the size and smoothness of a mesh, a series of steps are performed. The input CAD geometry/model generally contains a number of geometrical flaws, i.e., holes,

multiple and/or missing surfaces. The geometry is cleaned from these flaws, as a first step. This task is done in ANSYS Workbench design modular. Design modular provides tools to do basic editing of the geometry and remove flaws by filling gaps/holes, adding,

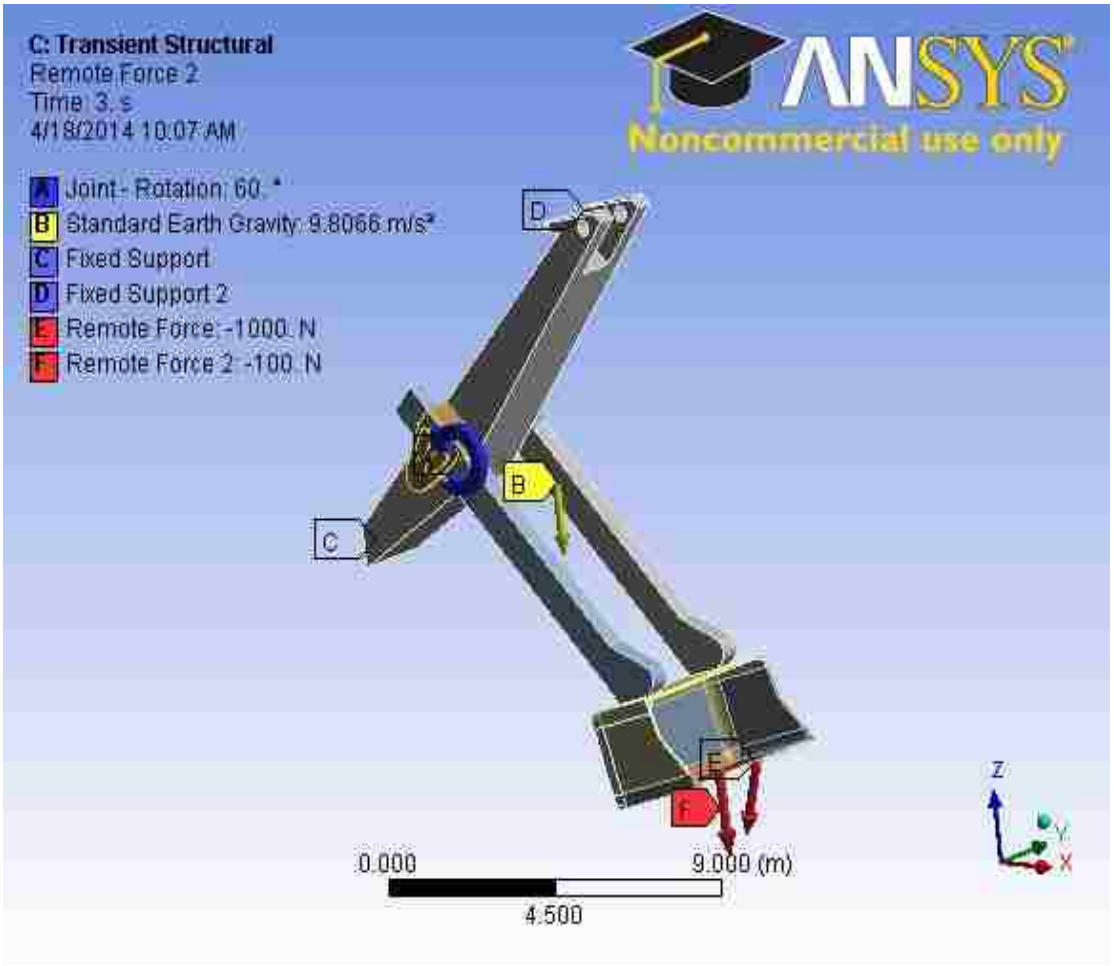

Figure 5.12. Boundary conditions and external forces on shovel front-end

deleting and merging surfaces. Further, all the fillet surfaces are removed to reduce the number of elements required. A process of dicing and slicing the whole body is adopted to make the bodies sweepable (one type of mesh element can be swept across the whole

body. The whole shovel body is diced and sliced to ensure that all the bodies become sweepable for meshing. The sweepable bodies provide an excellent control for meshing as element types and sizes, and hence mesh size, can be defined for each body. Element

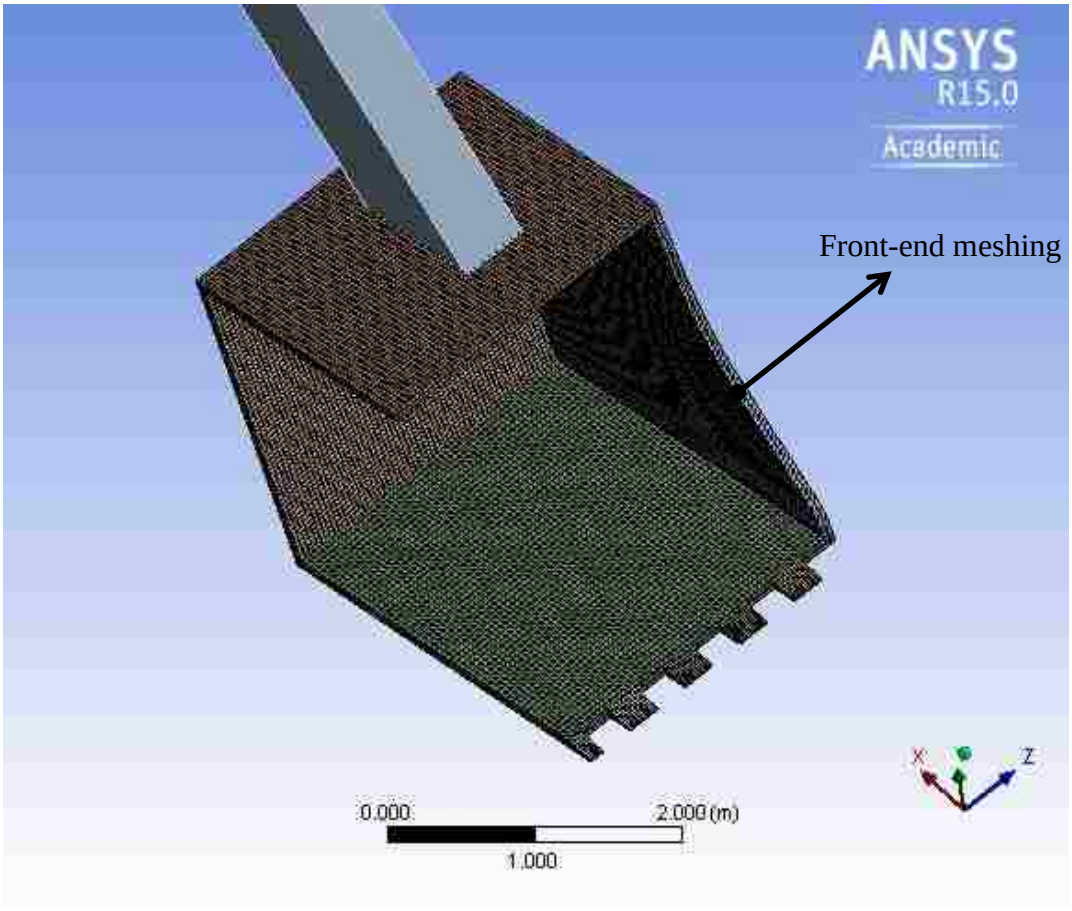

Figure 5.13. Meshing of dipper and crowd-arm

types and sizes, for this research, are chosen based on the complexity of the geometry and details of the analysis required for a particular part of the shovel body. Three dimensional brick elements are utilized to mesh the dipper-handle. A coarse mesh is created for the crowd-arm as the stress modeling is not performed for the dipper. The dipper is the main

focus of this research. Therefore, the dipper body is modeled using brick elements with a minimum of three elements through the thickness of the dipper. The resulting mesh is shown in Figure 5.13. Similarly, mesh refinement is applied to the teeth during the fatigue modeling process as a fine mesh is required for the analysis.

5.3.3. Dipper's Trajectory Modeling. Dipper trajectory is given as an input function to the shovel simulation process in Matlab/Simulink. The dipper traverses the known trajectory and the reverse kinematic model is used to determine the crowd-arm

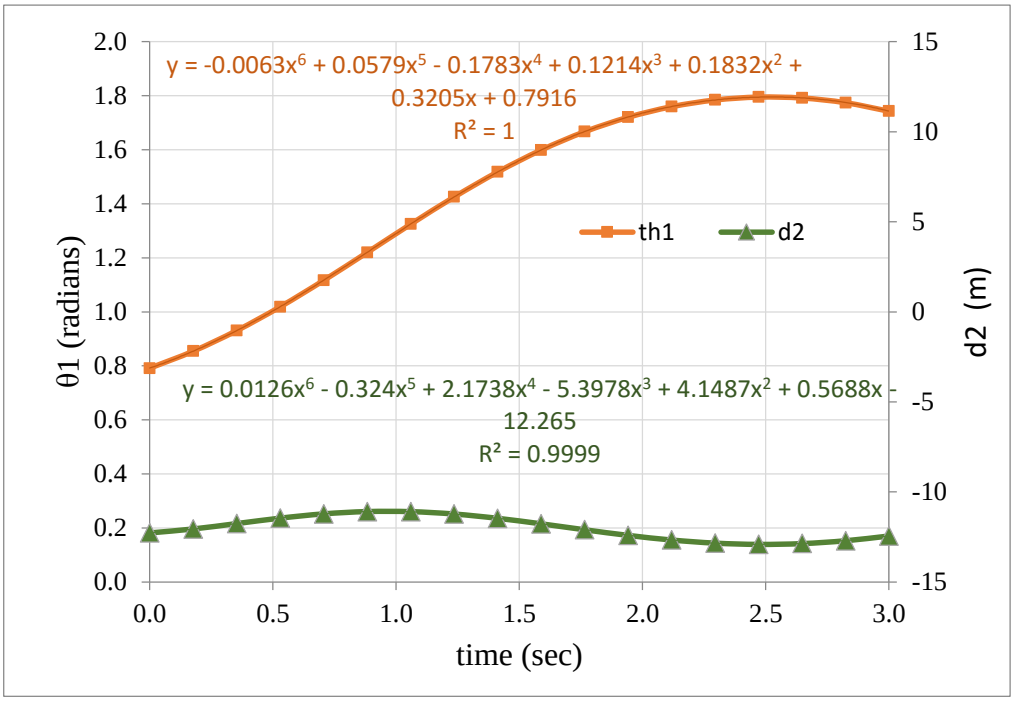

Figure 5.14. Crowd-arm rotation and extension modeling for trajectory

extension (d_2) and rotation (θ_1) requirements to achieve this trajectory. The dipper trajectory is shown in Figure 5.4 and the required crowd-arm extension (d_2) and rotation (θ_1) are shown in Figure 5.5. These two output parameters (d_2 and θ_1) from the numerical

simulation process are used as inputs for the shovel virtual prototyping. Together, these two define the dipper's trajectory. The functions for d_2 and θ_1 are generated in MATLAB R2012a, using a curve fitting process. The function generated for crowd-arm extension (d_2), as a higher order polynomial of time, is given as equations (5.7). And, the function generated for crowd-arm rotation (θ_1), as a higher order polynomial of time, is given as equation (5.8).

$$d_2 = 0.0063t^6 + 0.0579t^5 + 0.1783t^4 + 0.1214t^3 + 0.1832t^2 + 3205t + 0.7916 \quad (5.7)$$

$$\theta_1 = 0.0.126t^6 - 0.324t^5 + 2.1738t^4 - 5.3978t^3 + 4.1487t^2 + 0.5688t - 12.265 \quad (5.8)$$

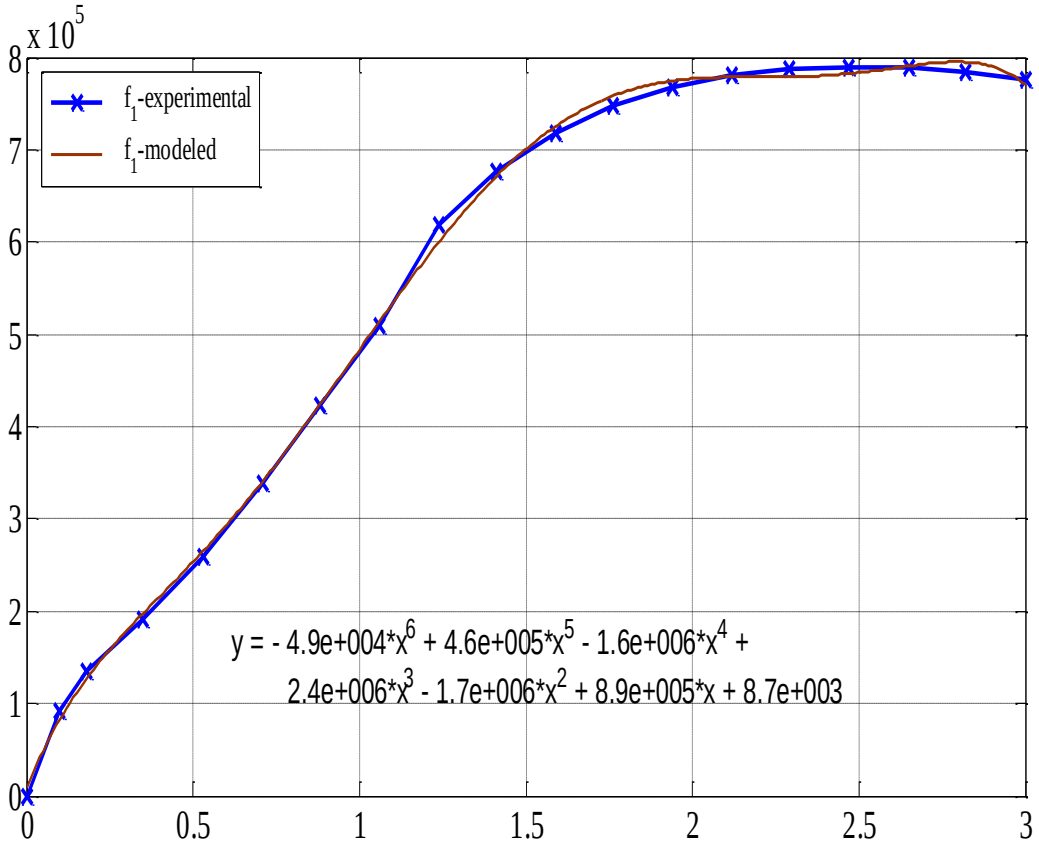

Figure 5.15. Force modeling of payload

The data-fitted models for d_2 and θ_1 are plotted in Figure 5.14. A comparison of these models with the simulation outputs for the same parameters as shown in Figure 5.5 indicates a high correlation. These two parameters (d_2 and θ_1) are given as inputs to the two joints of the shovel model. Crowd-arm rotation (θ_1) is used as input for the revolute joint between the boom and the saddle. The extension (d_2) is given as input to the translation joint between the crowd-arm and the saddle-block.

5.3.4. External Forces Modeling. The gravitational, material-resistance, and material-weight forces act on the shovel during the shovel excavation process. The material resistance and weight forces are computed during the shovel dynamic simulation and are fed into the system as a time function. The gravitational force acts on all the bodies and is modeled as standard gravitational force acting in the negative Y direction of the reference frame.

The force due to payload (f_1) is computed during the numerical simulation process performed in MATLAB/Simulink. The calculated force is illustrated in Figure 5.7. A function for this force (f_1) is generated in MATLAB using a curve-fitting method. A higher order polynomial is used to model this function to achieve better accuracy and smoothness for short-step sizes during virtual prototyping. The model function is given as equation (5.9) and is shown in Figure 5.15. This force is distributed on the shovel dipper and back-side plate of the shovel. The force is considered as a uniformly distributed force, acting along the negative Y direction, during the virtual prototyping process.

$$f_1 = -4.9e4t^6 + 4.6e5t^5 - 1.6e6t^4 + 2.4e6t^3 + 1.7e6t^2 + 8.9e5t + 8.7e3 \quad (5.9)$$

The payload also exerts a force on the side-walls. This force is modeled using the earth pressure at-rest theory (Coulomb, 1776). According to this theory, the side

horizontal earth pressure at-rest is k_{ep} times the vertical pressure as in equation (5.10). Where k_{ep} is given by equation (5.11).

$$P_h = k_{ep} * P_v \tag{5.10}$$

$$k_{ep} = 1 - \sin(\varphi) \tag{5.11}$$

In this case, the vertical pressure (P_v) is the payload. This calculated side force is considered to be acting uniformly over the side wall.

The digging force (F_r) and its components (F_t and F_n) act on the shovel teeth. The component forces, F_t and F_n, act in the dipper coordinate frame. F_t acts along the dipper bottom plate and F_n acts normal to the plane of the teeth. The forces are also computed during the numerical simulation process, and are shown in Figure 5.9. These forces are modeled, as time functions, in MATLAB through a curve fitting process. The force Ft is modeled as a higher order polynomial function of time and is given as equation (5.12).

Similarly, the forced F_n is modeled as a higher order polynomial function of time and is given as equation (5.13). The modeled force is illustrated in Figure 5.16.

$$\begin{aligned} F_t = {} & -65.72t^9 + 1028t^8 - 6550t^7 + 21270t^6 - 34521t^5 + 18200t^4 \\ & + 12120t^3 - 2371t^2 + 6481t + 769.3 \end{aligned} \tag{5.12}$$

$$\begin{aligned} F_n = {} & -91.66t^9 + 1198t^8 - 6327t^7 + 17360t^6 - 27960t^5 + 34700t^4 \\ & - 42370t^3 + 21960t^2 + 29910t + 2586 \end{aligned} \tag{5.13}$$

5.4. SHOVEL STRESS AND FATIGUE MODELING AND ANALYSIS

The shovel stress analysis is performed in ANSYS Workbench-R15.0 (ANSYS, 2014a). First a rigid body analysis is performed to assure that the dipper follows the given trajectory for the given angular rotation, crowd-arm extension and the external forces. Afterwards, a transient analysis is performed for the dipper's stress analysis.

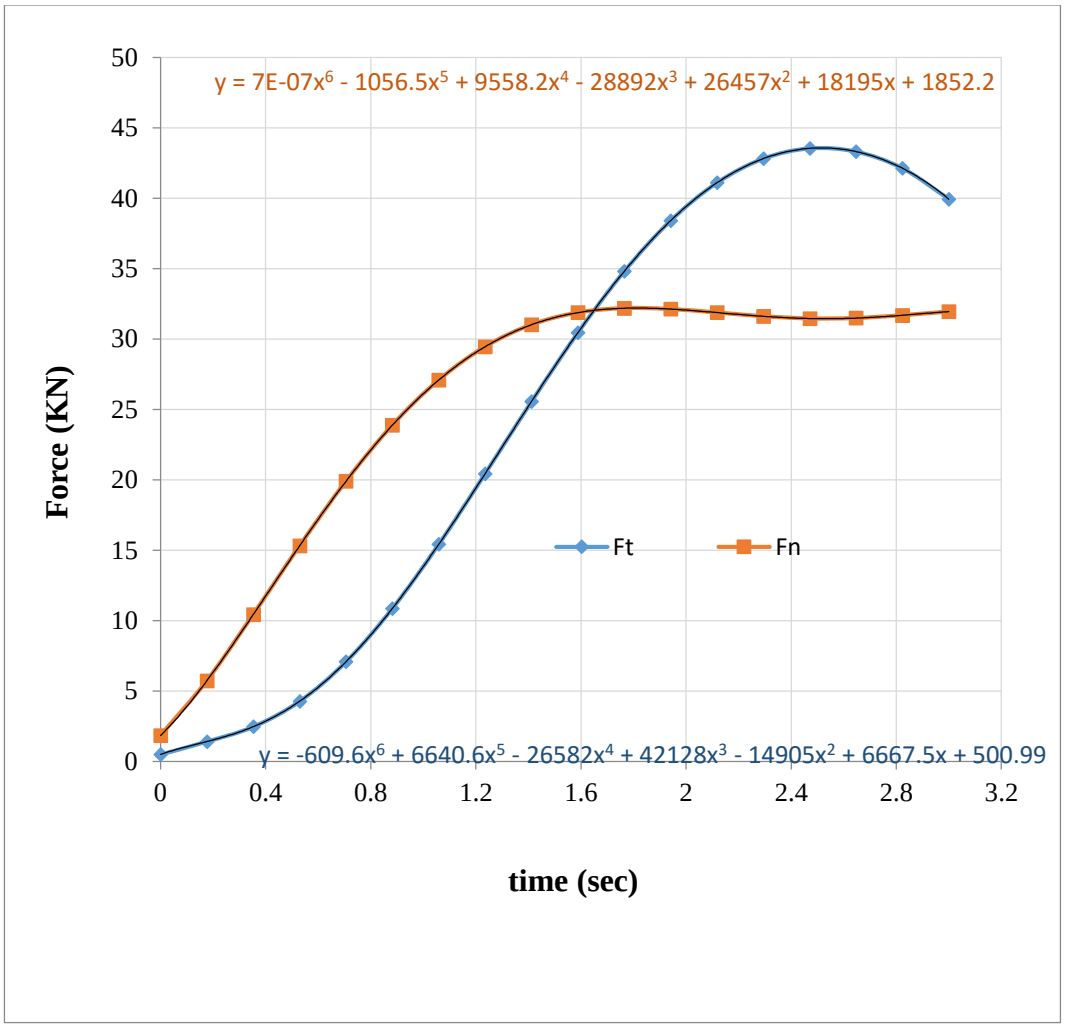

Figure 5.16. Modeling for resistive forces on dipper

5.4.1. Rigid Body Analysis of Shovel Dipper. First a rigid body analysis of the dipper is performed in ANSYS Workbench R14.5. During this rigid body analysis in ANSYS Workbench R14.5 all the geometrical parts of the dipper are modeled as rigid bodies and consist of only one node per body. This greatly reduces the computation time requirements and ANSYS uses a robust rigid body solver for this analysis.

Rigid body analysis is performed to validate that the dipper follows the desired trajectory for the given set of angular rotation, crowd-arm extension, and all the external

forces. The angular rotation and crowd-arm extension are given as input functions defined in equations (5.7) and (5.8). The external forces due to payload, side-wall pressure, and digging resistance are provided as input functions defined as equations (5.9), (5.10), (5.12), and (5.13).

The total simulation time for rigid body analysis is set at 3 seconds, typical of P&H 4100 XPC shovel, and is run in two steps. The first step lasts for 0.001 second and the second step starts at 0.001 seconds and ends at 3 seconds, the simulation's end time. This very small first step ensures that the external forces do not get very high in magnitude at the start of the simulation process. The presence of high forces at zero time creates convergence issues. The first step is further divided into multiple time steps with a minimum step-size of 1e-6 second and a maximum of 1e-5 seconds. This creates anywhere between 100 to 1000 time sub-steps for the first simulation step and allows the external forces to grow as a stepped loading. Equation (5.14) explains this step-loading concept for the external force modeled in equation (5.13), which is the equation for the tangential component of digging force on the dipper. At time zero, this force has a value of 2586 N. This high force value at zero time is transformed into a stepped loading by defining this force as a function of time (F_t= 2586*t) during the first simulation step. At the end of the first step size the full loading function is applied from step two of the simulation till the end of simulation. The equation (5.13) is modified as equation (5.14).

All the other forces acting on the dipper and teeth assembly are modified in a similar way. For all these forces, the high force intercepts (forces at zero time) are modelled as functions of time during the first simulation step. The smaller step-size of the first time-step allows the force to grow slowly initially and reach a force intercept value by the end of the first step. The full force function kicks in from the second step.

$$F_t = \begin{cases} 2586t & \forall\, t = 0 - 0.001\text{sec} \\ -91.66t^9 + 1198t^8 - 6327t^7 + 17360t^6 - 27960t^5 & \\ \quad + 34700t^4 - 42370t^3 + 21960t^2 + 29910t + 2586 & \forall\, t = 0.001 - 3\text{sec} \end{cases} \tag{5.14}$$

5.4.2. Transient Analysis of Shovel Dipper. A transient analysis of the dipper-and teeth performed in ANSYS Workbench R15. For this analysis, the dipper-and-teeth assembly and crowd-arm are converted into flexible bodies. This change allows ANSYS to compute stresses on the dipper components. All force functions, as used during the rigid-body analysis, remain the same. The joint functions are defined for the desired trajectory generation. The dipper's flexible bodies are meshed appropriately, using sweepable bodies and controlled meshing. The dipper's mesh model is shown in Figure 5.13. As used previously during the rigid body analysis, the simulation time is set at 3 seconds. The simulation is run in two steps with multiple sub-steps for better convergence. A minimum time step of 1e-6 seconds and maximum time step of 2e-5 seconds are used for the simulation. This creates anywhere between 100 to 1000 time sub-steps for the first simulation step and allows the external forces to grow as a stepped loading. These step sizes gave a converged solution for all the cases. ANSYS uses an efficient solver (mechanical APDL) for stress analysis. The dipper's stress profile generated through transient analysis, to overcome the resistive forces and to trace the desired trajectory, is presented in Figure 5.17.

5.4.3. Fatigue and Fracture Life Modeling of Dipper and Teeth. The variation of cutting and weight resistive forces results in stress loading of shovel front-end components. The dipper and teeth assembly engages directly with the formation which results in stress loading of the shovel front-end assembly. The loading is cyclic and is generally a continuous process for shovel operation. This cyclic loading results in the

fatigue cracking of the front-end components. The initiated fatigue cracks, and the ones already present due to manufacturing flaws, can propagate to critical lengths and result in component failure, which then leads to expensive repairs and shovel downtimes.

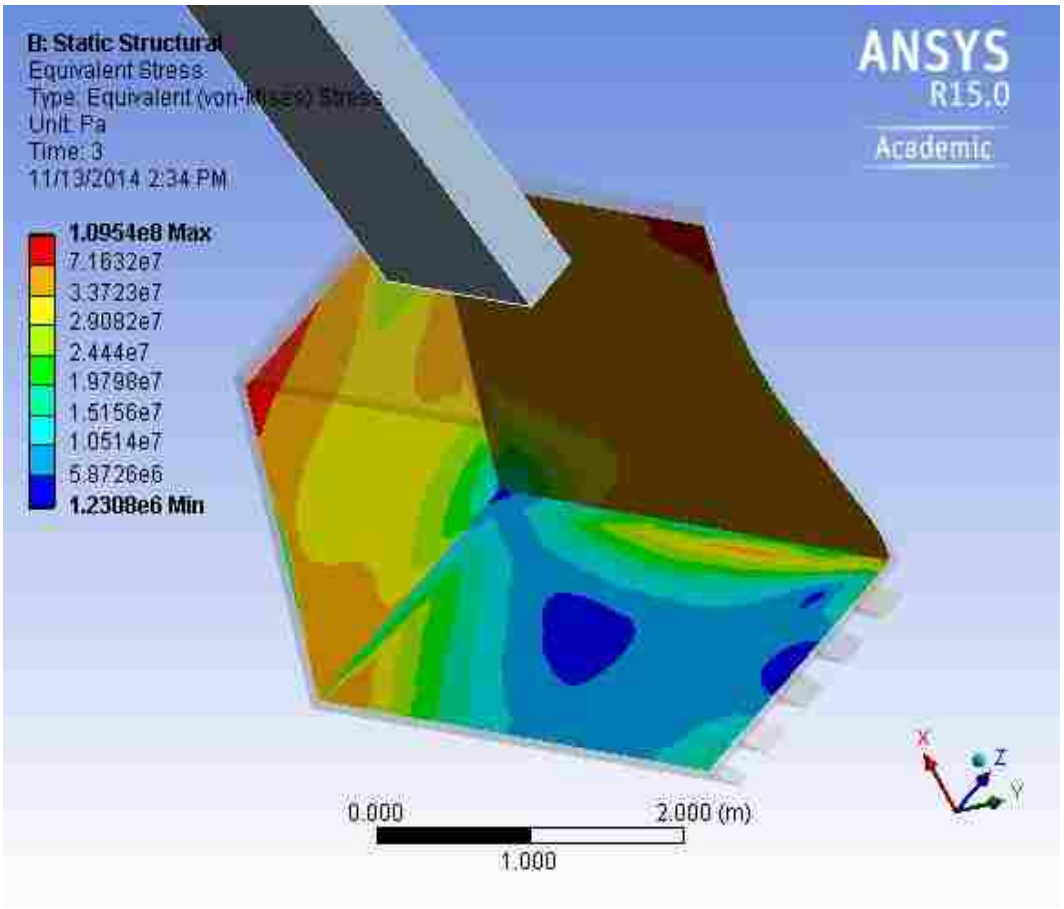

Figure 5.17. Equivalent stress (von-Mises) stress loading of dipper

As shown in Figure 2.2, the crack life is divided into three phases- initiation, propagation, and rapid growth to failure. Majority of crack life is spent during the propagation phase. Crack initiation can also be attributed to material and geometrical flaws, other than the stress and environmental factors. In the field, the shovel front-end

components are engaged directly with abrasive and hard material. Therefore, there is always a greater chance of localized pitting, deep abrasion and grooving for the dipper and teeth assembly. These pitting, grooving, abrasion and welding repairs can act as the initial cracks and are a subject of interest for this research.

5.4.3.1. Numerical computation of SIFs. As discussed in Section 2.4.2, the most common methods for calculating fracture mechanics parameters are the J-integral, energy-release rate, and stress intensity factor. These parameters are available in literature for simple geometries and loading conditions. However, for complex geometries and loading conditions, the calculation of these parameters is not an easy task and numerical techniques need to be applied for an accurate estimate of these parameters.

Finite element techniques evaluate the fracture mechanics parameter using the energy release rate method. Many commercial software packages present the option to calculate these parameters, as does ANSYS Workbench (R15). ANSYS Workbench R15 provides several tools to evaluate fracture mechanics parameters that rely on calculating the domain integral, interaction integral, or virtual crack-closure techniques (Raju and Newman, 1997). In all these techniques, energy release is estimated around the crack tip nodes in close loops, in the form of contours. For 2D cases, the node at the crack tip forms the first contour. While for 3D cases, all the nodes forming the crack-front determine the first contour.

The shape, length and depth of a crack determine the crack life at a specific location. There can be an infinite number of possible combinations for the shovel dipper and teeth. One of the important field usable results of this research is to determine the safe maintenance interval for the shovel operation. The field practice is that the operator takes a walk around the shovel before every shift and visually examines crack formations

with the naked eye. Given the huge size of the dipper-and-teeth assembly, a 3-inch crack length for the dipper and 1-inch for the dipper teeth is selected for the analysis here.

The stress profile close to crack-tips is very high. As a result majority of the cracks can be considered as elliptical in shape. Elliptical shaped cracks are the most commonly studied cracks for metals. ANSYS Workbench R14.5 introduced a fracture module for fracture analysis of elliptical cracks. The module can calculates the stress intensity factors (SIFs) and J-integrals for three modes of fracture failure. This fracture module is chosen for the fracture analysis for this research. This research is only analyzing the surface elliptical cracks in the dipper-teeth assembly, therefore, this module is suitable for this research.

For this research, representative cracks in the bottom-plate, side-wall and teeth are analyzed for life expectancy and the results are used to determine the safe maintenance interval. In the present version of ANSYS R15, only one crack can be analyzed for stress-intensity determination at a time. A finer mesh is required around the crack geometry. These conditions make crack simulation and analysis computationally expensive and long. Missouri S&T's high performance computing cluster (2014) is used to run the virtual prototype simulations.

5.4.3.2. Crack geometries for SIF computation. Figure 5.18 illustrates the location and geometry of a modeled elliptical crack in the dipper's bottom plate. This representative crack is 3-inch long and is 1-inch deep. A localized reference system defines the geometry of this crack. Crack plane lies on this XZ plane, while the width of crack is along the Y direction of this plane. The crack grows along the X and Z directions. The associated mesh models for this crack are shown in Figures 5.19 and 5.20.

Figure 5.19 illustrates the mesh model of a representative elliptical crack in the dipper bottom plate. Figure 5.20 illustrates the wire frame mesh model for the same crack. As illustrated in both figures, there are six circular contours around the crack-front inside

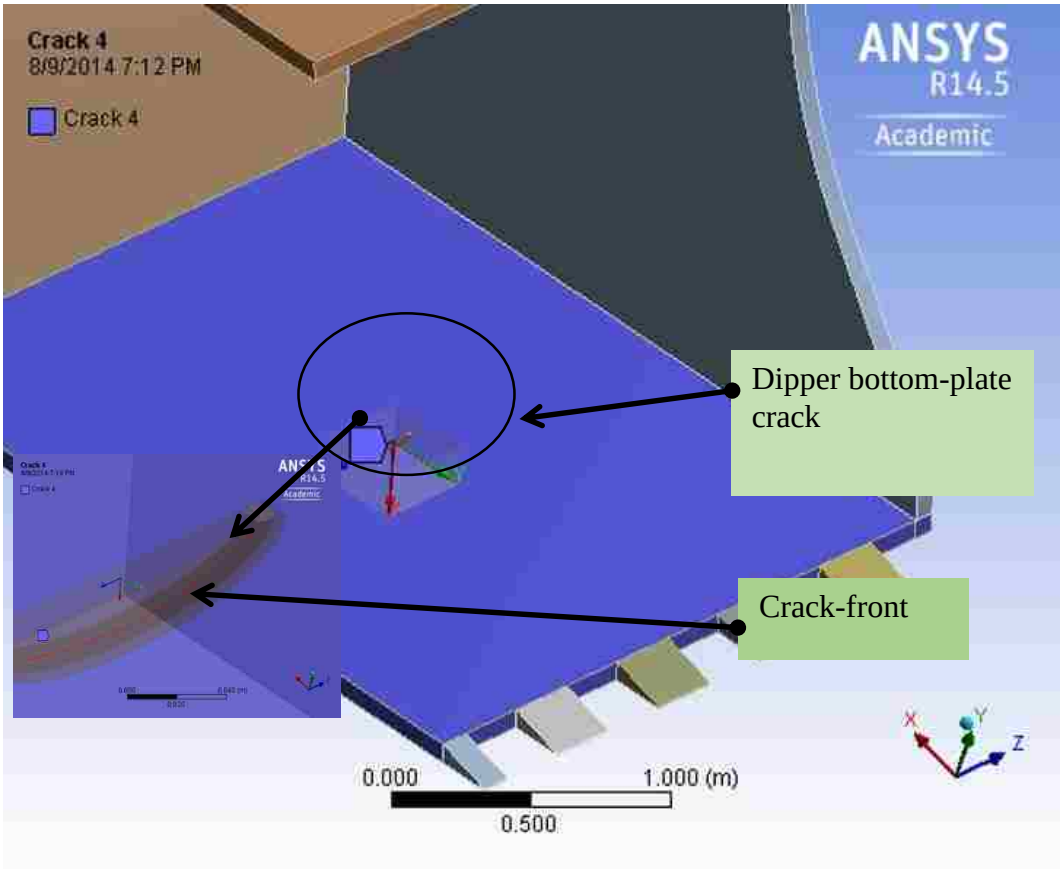

Figure 5.18. Elliptical crack at middle of the dipper bottom-plate

the dipper-bottom plate. Each circular contour has eight divisions. There is a node at the ends of each segment. Therefore, each circular contour consists of eight nodes around the crack-front. The crack-front is divided into eighteen segments, each represented by a node in the mesh model. Therefore, the eighteen nodes define the crack-front in this model.

Stresses are computed at every node around the crack-front and the six contours generate the stress profile around the crack-front. The stress profile is used to compute the SIFs for each simulated crack.

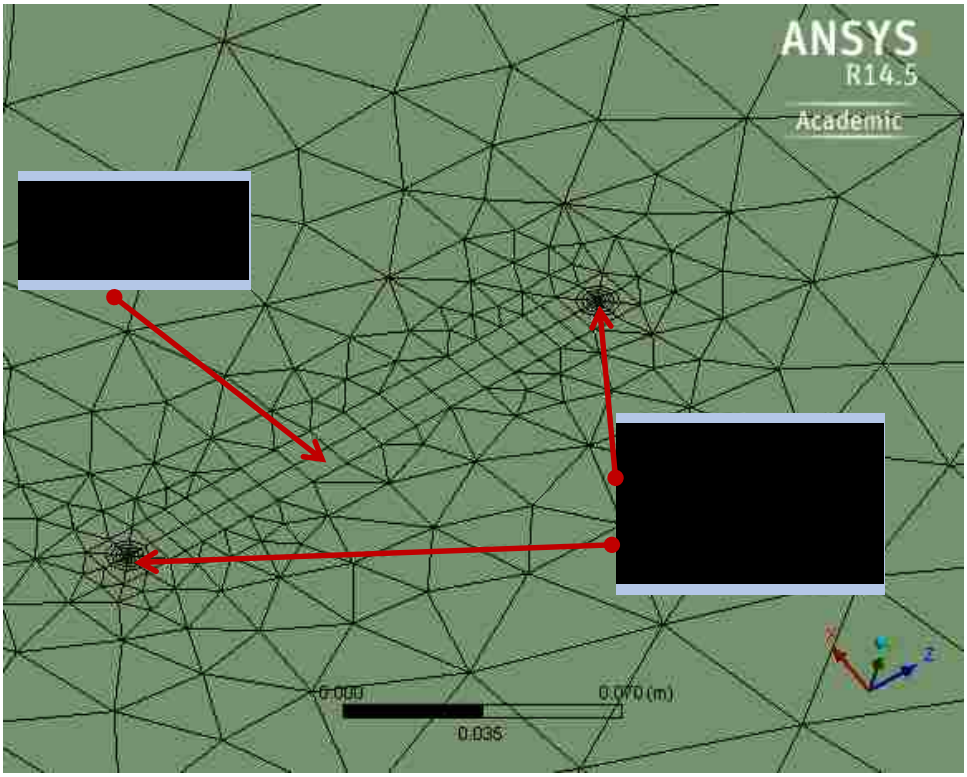

Figure 5.19. Mesh model for the bottom plate elliptical crack

Similarly, crack simulations are performed for the dipper's side-wall. A representative crack in the dipper side-wall is shown in Figure 5.21. This representative crack is elliptical in shape and is 3 inches long (major axis) and 1 inch deep (minor axis). The crack is oriented horizontally at the middle of the dipper side wall. A local coordinate frame is assigned at the center of the crack. The crack plane is set on the XZ plane of this reference frame. The length of this crack is along the Z axis and depth of the crack is

along the X axis. The width of the crack is along the Y axis. A very small width is assumed for the crack to represent a hairline crack.

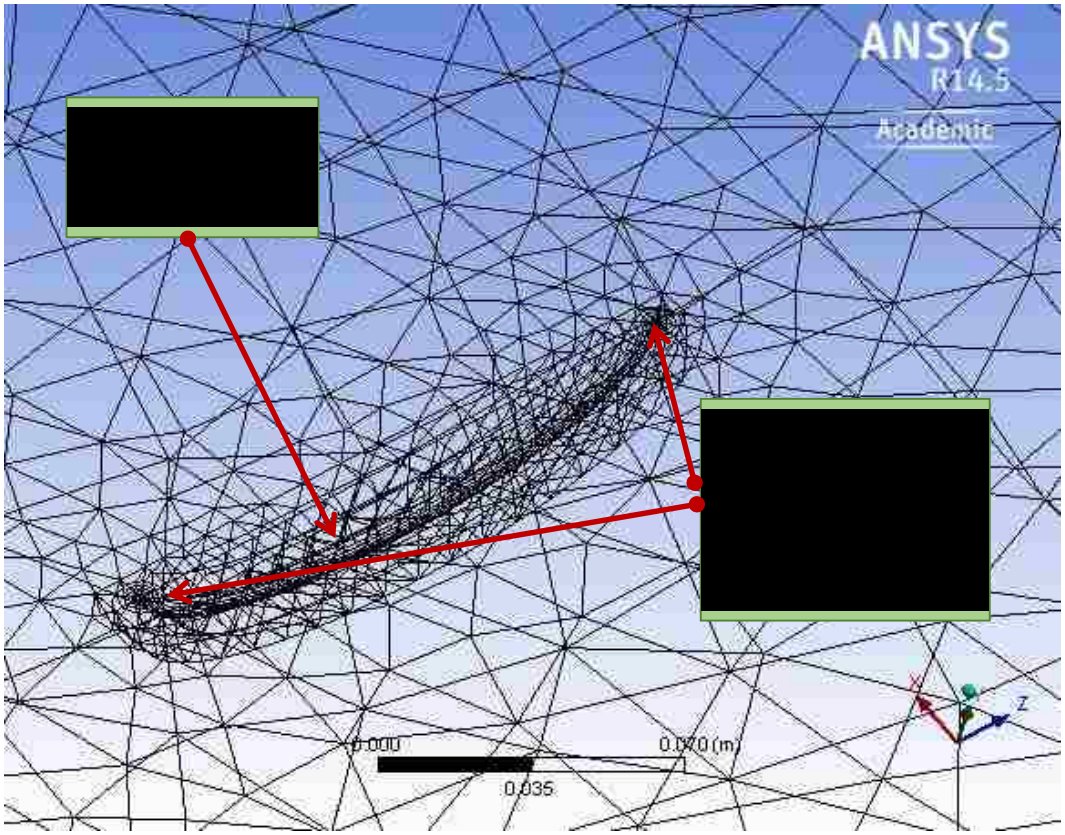

Figure 5.20. Wireframe mesh model for the bottom plate elliptical crack

The associated mesh generated for this side-wall crack is shown in Figure 5.22. The same parameters, as used for the bottom-plate crack, are used to define the mesh profile for this crack. There are six contours around the crack-front inside the side-wall. Each circular contour is divided into eight segments. There is one node at the endpoint of each segment. Therefore, every contour consists of eight nodes around the crack-front. Crack-front itself is divided into eighteen segments and hence, eighteen nodes. Stress is

computed at each of these nodes during the dynamic analysis and is used to compute the SIF for each crack.

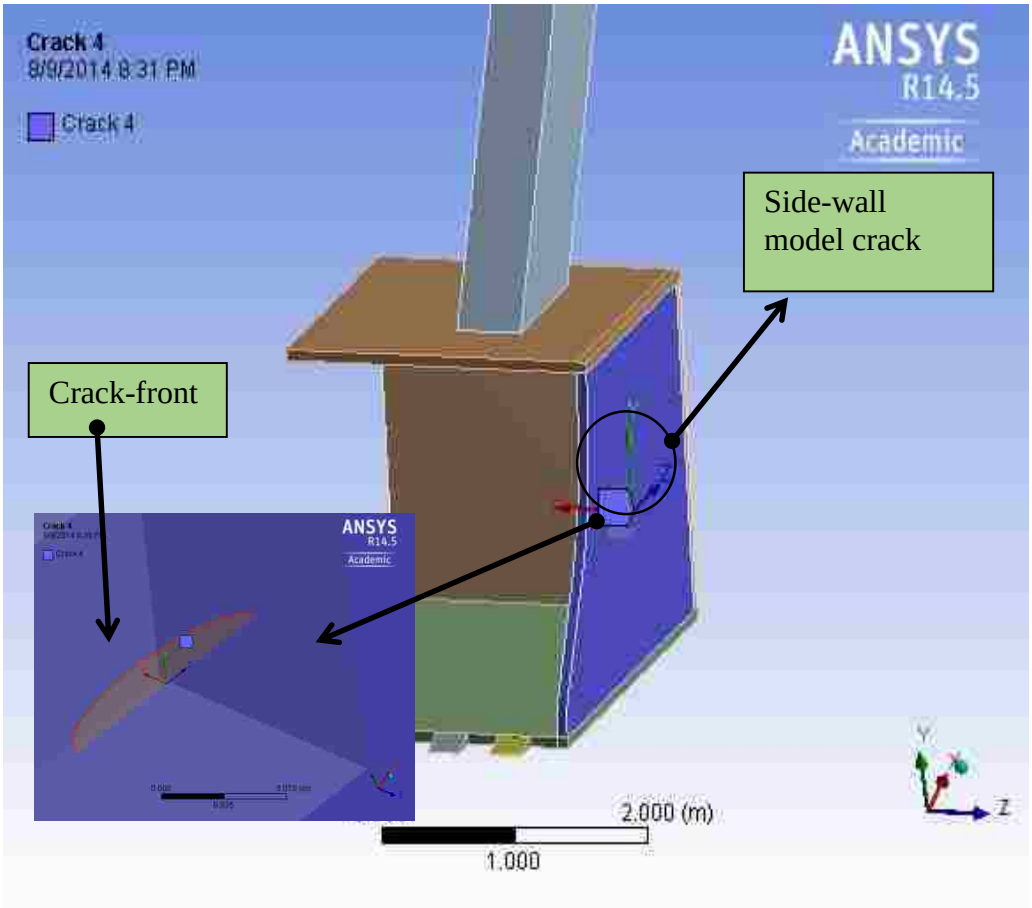

Figure 5.21. Elliptical crack at middle of the dipper side-wall

Similarly, a representative elliptical crack-front is modeled on the face of the corner tooth. The modeled crack is parallel to the cutting edge of the tooth and is located at the center of the tooth face. The crack's length is 1-inch with a half-inch depth. The crack's length and width represent the major and minor axes of the elliptical crack, respectively. The location and geometry for this crack are illustrated in Figure 5.23. A

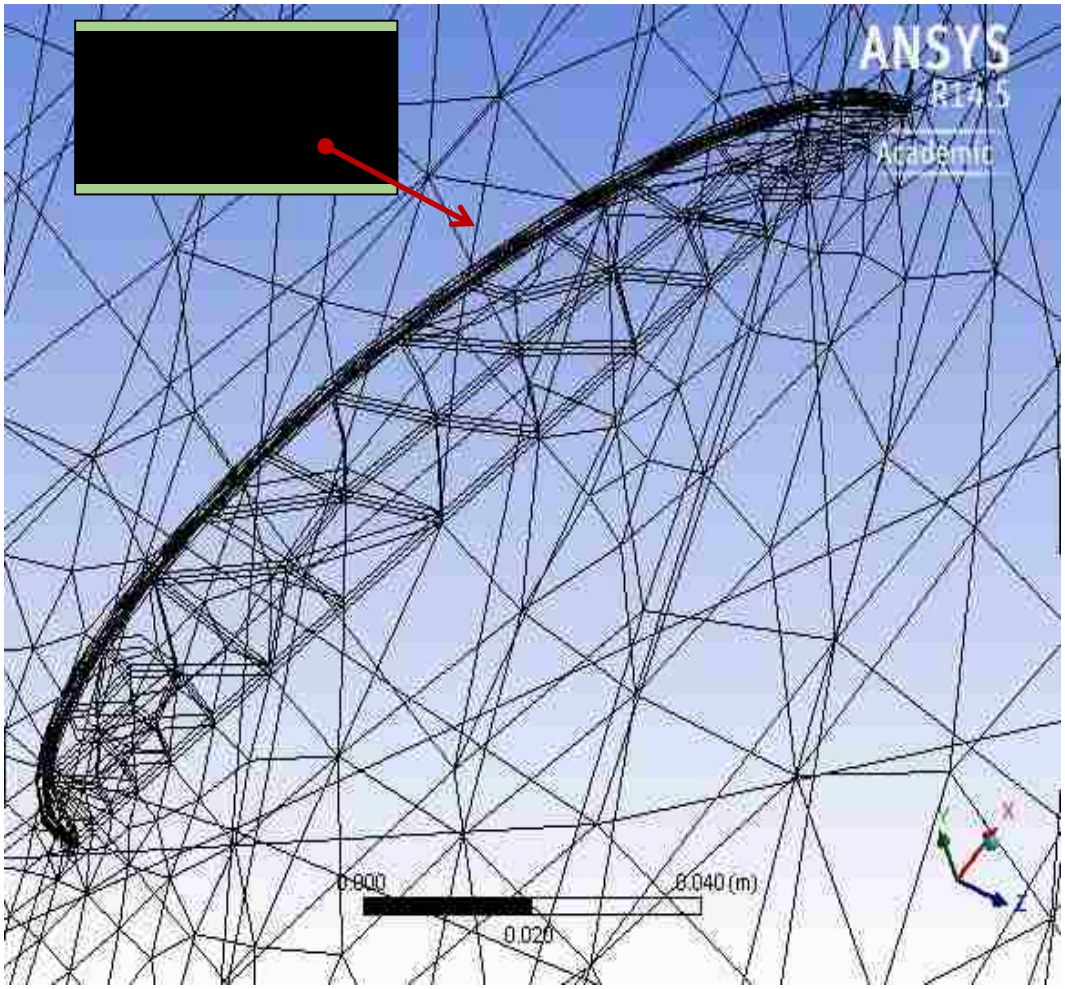

Figure 5.22. Mesh model for the side-plate elliptical crack

local coordinate frame is assigned at the center of this ellipse and the crack-front is in the XZ plane with major and minor axes along the Z and X directions respectively. The crack-front is represented by eighteen nodes and there are six contours around every node of the crack-front. Each contour consists of eight nodes. The mesh model for this crack is shown in Figure 5.24. The SIF is calculated at each node of the crack-front using these six contours and their nodes.

The important fracture modeling parameters for the three representative cracks are summarized in Table 5.3. The geometry of these crack-fronts is semi-elliptical and is

defined by major and minor axis. Major and minor axes of this crack geometry define the length and depth of the cracks respectively. A local coordinate frame is assigned at the center of the elliptical crack-front with major and minor axis along the Z and X directions respectively. The crack-front is divided into a number of segments, which define the number of nodes. The crack-front is surrounded by circular contours, which are represented by nodes.

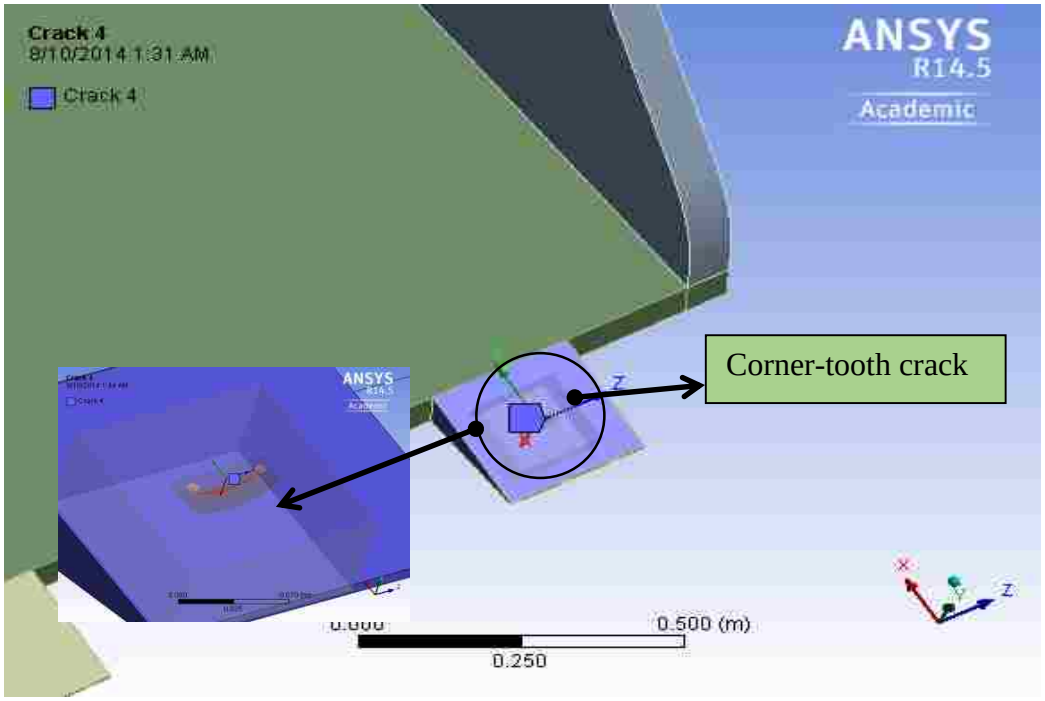

Figure 5.23. An elliptical crack at the center of the corner tooth

5.4.3.3. SIFs for representative crack geometries. SIFs for all the six contours around the crack are numerically computed in ANSYS R15. SIFs for mode-I (crack opening mode) conditions are calculated for every contour. The simulated representative crack-front for the dipper bottom-plate is illustrated in Figure 5.25. The figure shows the

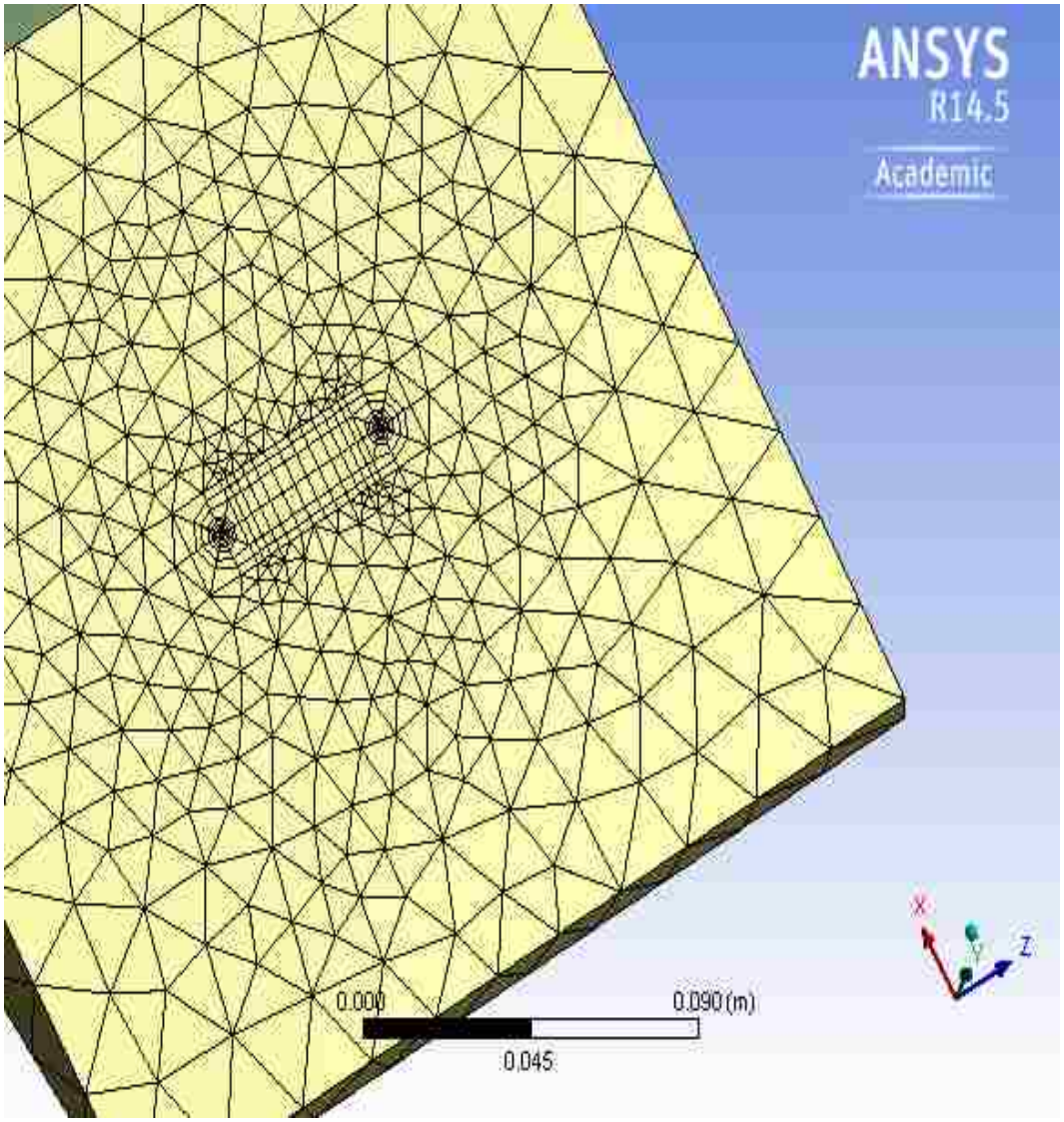

Figure 5.24. Mesh model for an elliptical crack on the corner tooth

SIF values (mode-1) for the 6th contour. Similar diagrams exist for all the six contours around the crack-front. These SIF values are used for life estimation of various size cracks on dipper, after detailed experimentation. The simulated crack-front for the dipper's side-wall, in mode-I, is illustrated in Figure 5.26, and for the corner-tooth surface crack in Figure 5.27.

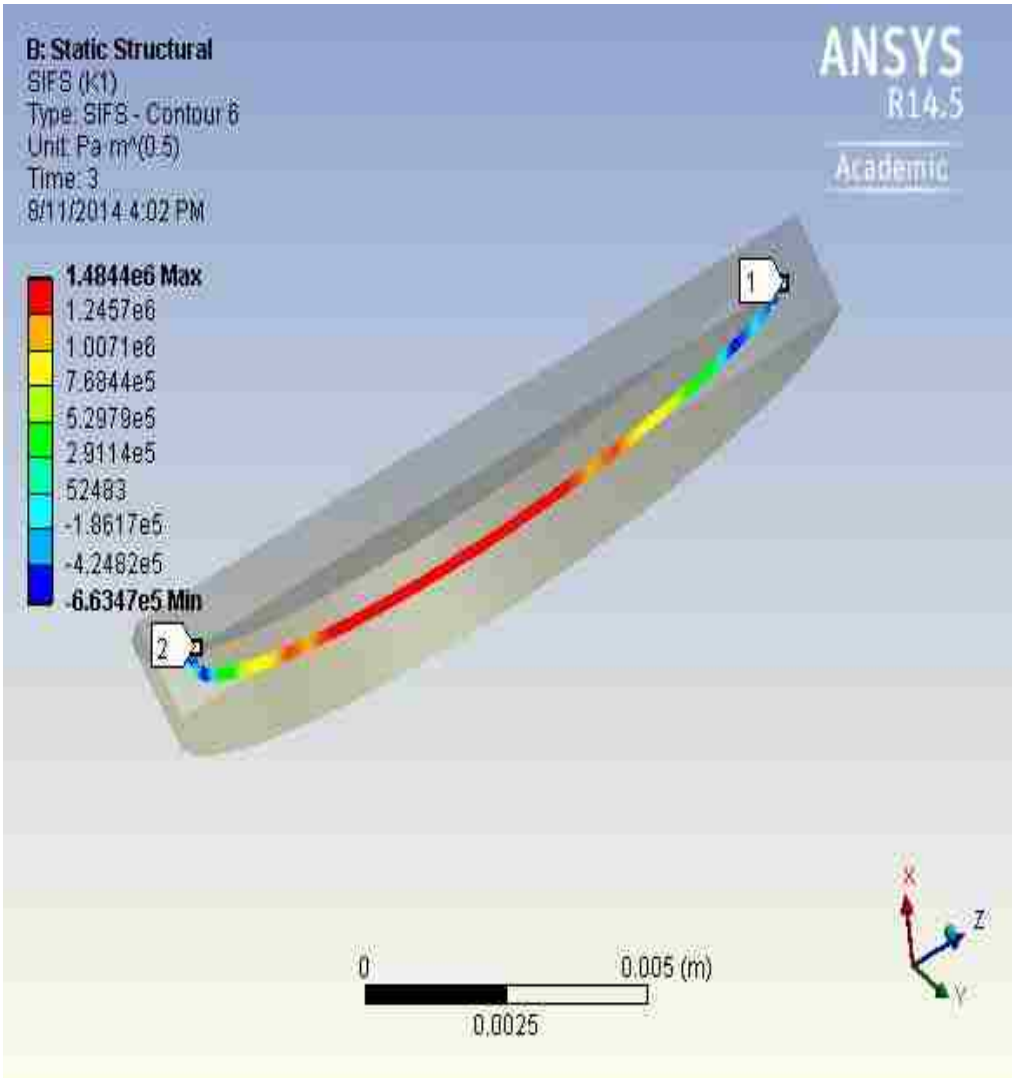

Figure 5.25. SIF for mode-1 for the dipper's bottom-plate crack

5.5. SUMMARY OF NUMERICAL SIMULATION AND VIRTUAL PROTOTYPE MODELING

A two-step simulation process is used for shovel stress and fatigue failure analysis. A numerical simulation process is used to generate the desired force functions in the first step. In the second step, a virtual prototype of the shovel's front-end is built and simulations are run to generate dipper's stress profile against the resistive forces. This

Table 5.3. Fracture Modeling Parameters of Representative Cracks

Parameter	**Description**	**Crack-1**	**Crack-2**	**Crack-3**
Location		Bottom Plate	Side Plate	Corner Tooth
Major Axis (m)	Length of crack	0.0762 (3-inches)	0.0762 (3-inches)	0.0254 (1-inches)
Minor Axis (m)	Depth of crack	0.0254 (1-inch)	0.0254 (1-inch)	0.0127 (0.5-inch)
Mesh Contours	No. of contours around crack-front	6	6	6
Circumferential Divisions	No. of division of contour circle	8	8	8
Crack-Front Divisions	No. of nodes to define crack-front	18	18	18

stress profile is used to simulate induced cracks in the bottom-plate, side-wall and corner tooth of the dipper, for life estimation of fatigue cracks.

A virtual test bench geometry is created and a desired dipper's trajectory is generated. This desired trajectory is used as an input function to the kinematic model to obtain the resultant crowd-arm extension and rotation. An optimized algorithm is used to model the dipper filling process. The dynamic weight force of the payload is calculated for the desired trajectory. The digging resistive forces on the dipper are computed at every simulation time step as well. The resistive digging and weight forces are applied on the dipper and the dipper's dynamic model is solved using MATLAB/Simulink software

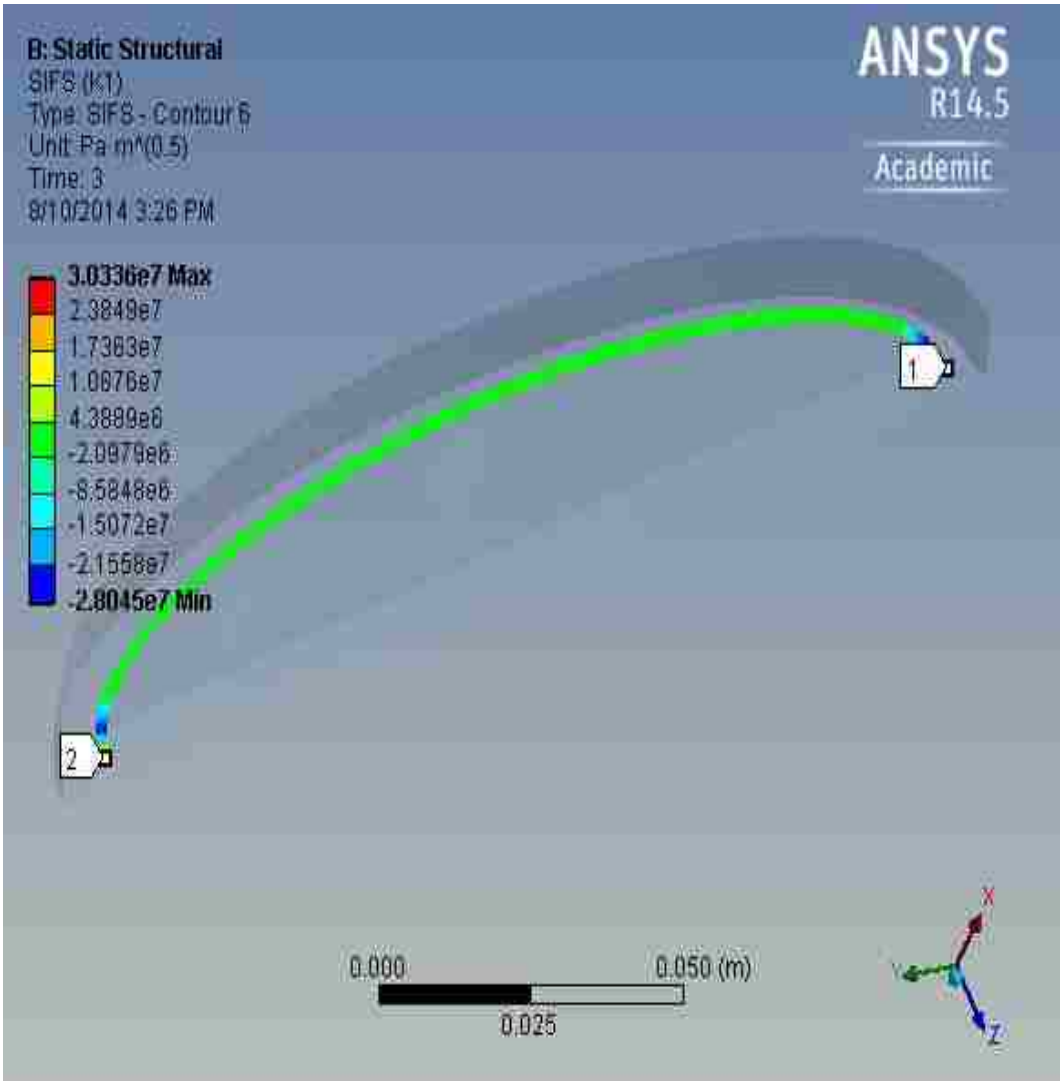

Figure 5.26. SIF for mode-1 for the dipper's side-wall crack

environment. MATLAB's Runge-Kutta algorithm is used for the numerical simulation process and the resultant hoisting torque and crowd-arm forces are computed.

The resistive force functions and the desired trajectory functions (created from numerical simulation process) are used as inputs for this virtual prototype. Both the rigid and flexible body analyses are conducted in ANSYS (R15) software. ANSYS (R15) contains numerically efficient routines to solve the complex FEM models. The dipper's

stress profile is generated for a set of input parameters. Representative fatigue cracks are induced in the bottom-plate, side-wall, and in the corner tooth of the dipper. SIFs are computed around these cracks which are later used for the life estimation modeling of the dipper.

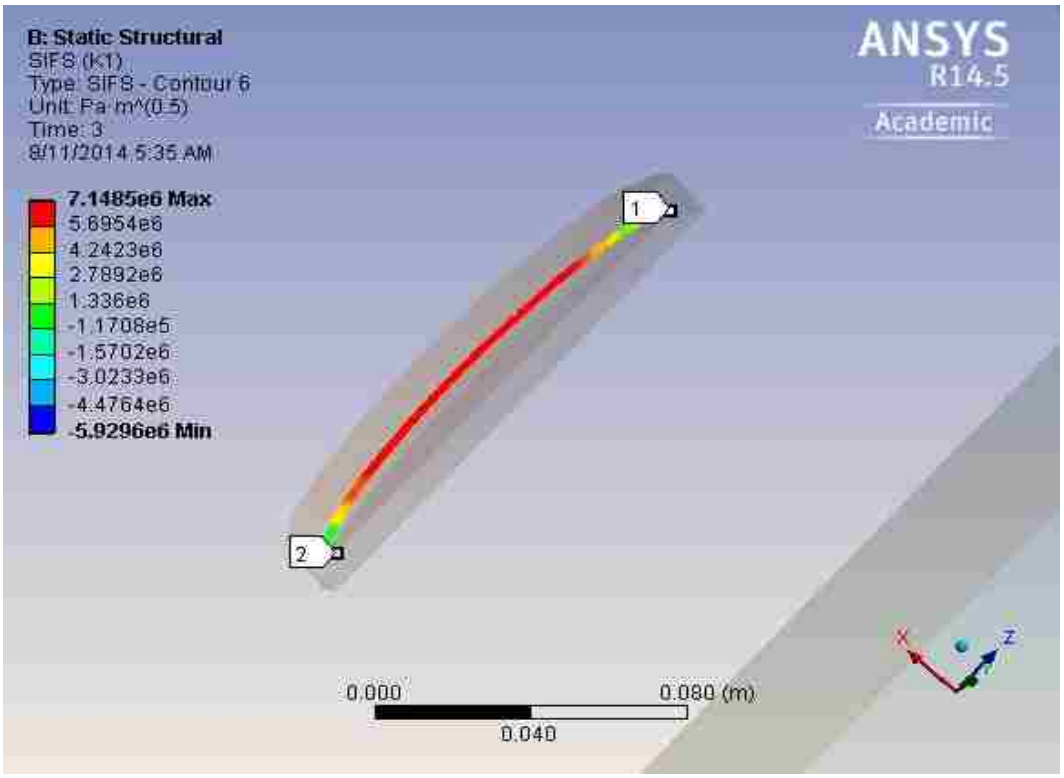

Figure 5.27. SIF for mode-1 for the dipper's corner tooth crack

6. EXPERIMENTAL DESIGN AND EXPERIMENTATION

A detailed experimental design is followed to analyze the important design variables for dipper stress and fracture failure modeling. The experimentation is twofold. The first set of experiments is designed to analyze the impact of critical field and formation parameters on dipper stress profile. The second set of experiments is designed to perform a detailed investigation of fracture propagations and life expectancy of pre-defined fractures at selected key locations of the dipper-teeth assembly. The key locations are the based on the stress profiling studies. The experimentation is performed using computer simulations, which are computationally expensive.

6.1. EXPERIMENTATION ENVIRONMENT

The experiments for dipper stress analysis and fracture failure modeling is performed using ANSYS R15 Workbench platform. ANSYS R15 Workbench platform provides an efficient framework for the design and simulation of common engineering design projects. It contains powerful and efficient routines for efficient meshing, finite element solutions, and simulations (ANSYS, 2014b). The virtual prototype of dipper-teeth assembly is based on a three-link mechanism connected through joints and contacts. There is no material non-linearity in the system as the shovel dipper-teeth assembly is assumed to be made of homogenous structural steel. However, the system has geometric non-linearity in the form of contacts and high-deflections of its components. For non-linear problems, the stiffness matrix of the finite element model is non-linear, and getting a nicely converged solution becomes a critical and challenging aspect of the solution process. The governing equation for a non-linear solution can be written as equation (6.1).

$$[K_i][\Delta u_i] = [F^{app}] - [F_i^{nl}] \tag{6.1}$$

The right hand side of this equation represents the out of balance force residual (difference between applied and nodal loads) after every iteration. Ideally, there shouldn't be any residual left at each iteration (exact solution), but that generally does not happen and there is always a residual left (approximate solution). For a converged and balanced system, this residual should decrease continuously with every iteration performed, within a certain tolerance and threshold. During the simulation, at the start of each iteration ANSYS makes an initial guess of the displacement vector [u_i] and calculates the force residual. This out of balance force residual is compared with the force convergence criterion and the displacement values are adjusted for next iteration. The iterations continue until the residual is lesser than the convergence criterion and the system comes in equilibrium.

A force convergence criterion (threshold and tolerance) becomes a key-factor for the solution convergence in non-linear finite element problems. A loose force convergence criterion might produce quick converged solutions with bad results. A tight criterion, on the other hand, might make unnecessary extra iterations without improving the results. For this research, a residual limit of 0.001*[F^{app}] is set as a convergence criteria and represent 0.1% of the applied load. This lower value of convergence criterion produced stable and acceptable solutions for this research. ANSYS graphically displays the force residuals as the Newton-Raphson residual outputs and these residual plots present a nice tool to test the system convergence (ANSYS, 2014b). The dipper-teeth assembly is subjected to steep loading forces at the start of digging cycles. The presence of these high resistive forces at the start of iteration process can cause convergence issues.

For this reason, the initial high load values are converted into stepped loading and are explained in Section 5.3.4. Maximum degree of freedom (Max DOF) is another stability criterion for finite element based dynamic analysis. ANSYS computes the maximum displacement on every contact node inside the model during iteration and compares it with the criterion. The solution is acceptable only if the Max DOF is within the acceptable limit. This ensures that the contact elements stay together during the simulation process. A program controlled limit is utilized to define the Max DOF limit. Both the convergence criterion and Max DOF limit ensure a stable and converged solution for the simulation experiments.

ANSYS R15 only allows a maximum of 32000 nodes for dynamics and structural analysis in ANSYS Mechanical (ANSYS, 2014b) academic license. Due to this limit, the mesh size cannot be refined beyond a certain element size. A strategy is adopted to use a coarser mesh for the dipper and a finer mesh in the proximity of the cracks for fatigue analysis. Even with the coarser mesh, the solution time for this problem is very long. On the dual core processor machine, the recorded computational time was more than 24 hours for stress related simulations only. Missouri S&T's high performance computing (HPC, 2014) facility is used for the experimentation purposes. The high performance computing platform consists of a cluster of powerful computers that makes the computation jobs faster and more efficient. ANSYS's remote solver manager (RSM) is used to communicate between the client and cluster.

6.2. EXPERIMENTAL DESIGN

A simplified experiment design procedure is adopted here to test the impact of critical variables on dipper stress-loading profile. Important stress related parameters are

first identified and then varied in a systematic way to analyze their impact on shovel stress profile. Similarly, a systematic approach is adopted to investigate the crack propagation properties of pre-defined cracks at the critical locations of the dipper. These locations are selected based on the stress analysis of dipper-teeth assembly and represent the high stress regions of the dipper. In addition, the cracks are investigated at the center of side-wall and bottom-plate, and on a corner tooth's face. The experimental design is based on the virtual prototype of P&H4100XPC shovel and the experimentation is run through computer simulations. The objective of the design and experimentation is to analyze the stress loading of the dipper-teeth assembly under varying field conditions, and to estimate the fatigue life of dipper components.

The important stress parameters are chosen to model the varying field operating conditions for a shovel. The selected field variables include material density, and resistive cutting forces. For material density, common formations excavated with cable shovel are selected that include coal, lime-stone, oil-sands, iron-ore, soil, granite, and copper ore. Typical material densities for these formations are used as inputs into the virtual prototype and simulations.

For the fatigue modeling, stress intensity factors (SIFs) for the pre-defined cracks at the highly stressed regions and at the center of the bottom-plate and the side-wall are computed by solving the J-integrals (Rice, 1968) around the crack-tips. Similarly, the SIFs are computed for the corner-tooth. Initial crack sizes, depths and orientations for these pre-defined cracks are systematically varied from a smaller to a larger crack and SIFs (J-integrals) are computed for each incremental crack. These SIFs are later used for life-expectancy and for estimation of the remaining life modeling for dipper-teeth assembly components.

6.3. EXPERIMENTATION FOR DIPPER STRESS MODELING

The dipper stress loading is a result of the interaction between dipper and formation. Dynamic resistive forces act on the dipper during the excavation process. There are a total of six resistive forces that act on the dipper during excavation (Hemami, 1994) and are explained in Section 2. Two dominant forces of all these forces are the cutting forces and the payload inside the dipper. Two separate series of experiments are designed to analyze the impact of these two forces on dipper stress loading profile.

6.3.1. Cutting Force Variation Experimentation. In this first series of experiments, the cutting forces are systematically varied for dipper's stress analysis. The cutting resistive force is calculated using the empirical models by Zelenin et al. (1985) in equation (2.7). According to this model, the cutting force depends upon a number of geometric parameters of the dipper (dipper-width, spacing between teeth, depth of cut, cutting angle and number of blows of a penetrometer "C_o"). The number of blows of penetrometer (sometimes called as dynamic densimeter) represent the number of drops of a weight of 2.5 kg on a flat, cylindrical end-piece of 1 cm^2 area to push this piece into ground to a depth of 10 cm (Zelenin et al., 1985). Other than "C_o" all other parameters are either fixed or can be controlled through bench geometric design. The parameter "C_o" is the only formation related parameter for the cutting force and is dependent upon many formation parameters e.g., density, moisture content, and type of soil. The value of this parameter can vary from 1 to 30 for unfrozen soils and 30 to 360 for frozen soils (Alekseeva et al., 1985; Zelenin et al., 1985). Here an initial value of 10 is selected for this parameter to represent soft or well blasted rock. During the first series of experiments, the value of this important parameter (C_o) is varied from 5 to 20 to determine its impact

on dipper stress profile. The cutting force is proportional to "C_o" as given in equation (2.7). With each single digit increase in "C_o", the resulting cutting force increases by 10%. Therefore, in the simulation experiments the cutting force is directly varied from -50% to 100% to reflect a variation from 5 to 20 in "C_o" respectively, with 10 being used as the reference value for "C_o".

Establishing a relationship between the stress-loading of dipper and parameter "C_o" is critical for many reasons. First, this is the only formation dependent parameter in the empirical cutting force model by Zelenin et al. (1985). Second, this parameter may be related to the rock fragmentation and blasting efficiency. The analysis will help determine the dipper stress loading in various soils and fragmented rock conditions. The analysis might be more useful for the teeth stress loading and fatigue failure analysis as these are directly engaged with the formation.

6.3.2. Material Density Variation. The second series of experiments analyzes the impact of material density on dipper stress profile. Material density defines the dipper payload. For a large shovel, like P&H4100 XPC, the dipper payload could be the most dominant of all these forces. Awuah-Offei et al. (2009) found the dipper payload to be most significant resistive force of all formation resistive forces. During this experimentation, the dipper's stress loading is computed for common excavated materials with large shovel. The typical density values for the tested materials are used for the experimentation.

The parameter "C_o" also depends on material density, although its direct relationship with material density is not measured by Zelenin et al. (1985). However, almost all of the cutting models show a linear relationship between cutting force and

material density as can be observed from the data presented by Wilkinson and DeGennaro (2007). Therefore, the cutting force is also varied in proportion to the material density variation. The cutting force is varied with the same percentage as the density of material is varied from the reference density of 1450 kg/m^3. Caution is exercised, as the higher density materials might cause the dipper payload to be more than recommended dipper capacity. This situation is avoided by implementing a constraint on the maximum dipper payload not to increase the manufacturer recommended dipper capacity (100 tons for this research). The above two experimentation series are summarized in Table 6.1 and 6.2.

6.4. EXPERIMENTATION FOR FATIGUE CRACK-FAILURE

A number of parameters control the crack failure modeling. These parameters include the crack geometry, shape, orientation and stress environment. A series of experimentation is run to investigate the crack-propagation of pre-defined cracks at the selected locations of the dipper in specific orientations.

Cracks can appear at any location of the dipper-teeth assembly or at any stresses location of the shovel front-end. The dipper-teeth assembly is huge in size and there can be an infinite number of possible combinations of crack-parameters (geometry, shape, orientation, stress environment etc.). The simulations are computationally expensive and require longer run times. Given the expensive computations, analyzing cracks at all of these locations is not optimal. Therefore, experimentation for crack failure and life-estimation is designed at the selected locations of the dipper-teeth assembly. These selected locations include high stress dipper regions, the center of side-wall and bottom-plate, and upper-face of tooth. All the dipper teeth are supposed to be loaded uniformly in the virtual prototype. Therefore, cracks are simulated only on the corner tooth. These

locations are shown in Figure 6.1. These selected, critical locations become the focus areas for further crack and life-estimation experimentation.

Table 6.1. Experimentations-I for Stress Modeling and Analysis

Experiment Series-I: Variation of Excavation Force	
Experimentation	Description
Variable and Scope	Variable: Co as defined in Zelenin (1985) model Scope: (Co = 5 to 20) Reference Value: 10 i.e., -50% to 100% variation in cutting force where the mean cutting forces is based on Co = 10
Number of Experiments	Total Number of Experiments: 15 Values of Co vary from 5 to 20
Significance	It is the only formation related parameter dependent upon the physical and mechanical properties of the formation It could be related to rock fragmentation and diggibilty.
Expected Results	The dipper stresses should vary in proportion with cutting resistive forces. The impact should be more profound on the teeth, which engage directly with the formation. Being smaller in proportion to the dipper payload, the overall dipper stress profile might not change significantly with this variation.

A separate series of experiments is run at each selected location of the dipper-teeth assembly. Pre-defined, semi-elliptical cracks are introduced at these locations, and are gradually incremented with fixed increments. The crack-depths are maintained at half of the crack-lengths for each crack increment. The semi-elliptical shape of the crack serves as the crack-front. Contours are created around the crack-front, and J-integrals are computed over each contour. These J-integral values are later used to compute the SIFs at the crack-tip.

For the side-wall experiments, semi-elliptical cracks are introduced at the center of the side-wall and the top corner. For each location, cracks are simulated in two orthogonal orientations (parallel and normal to the bottom-plate) as shown in Figure 6.2. These cracks are gradually incremented from a quarter of an inch to three inches with a step size of 0.5 inch. The depth of these cracks is incremented from one-eighth of an inch to 1.5 inches (half of the crack length).

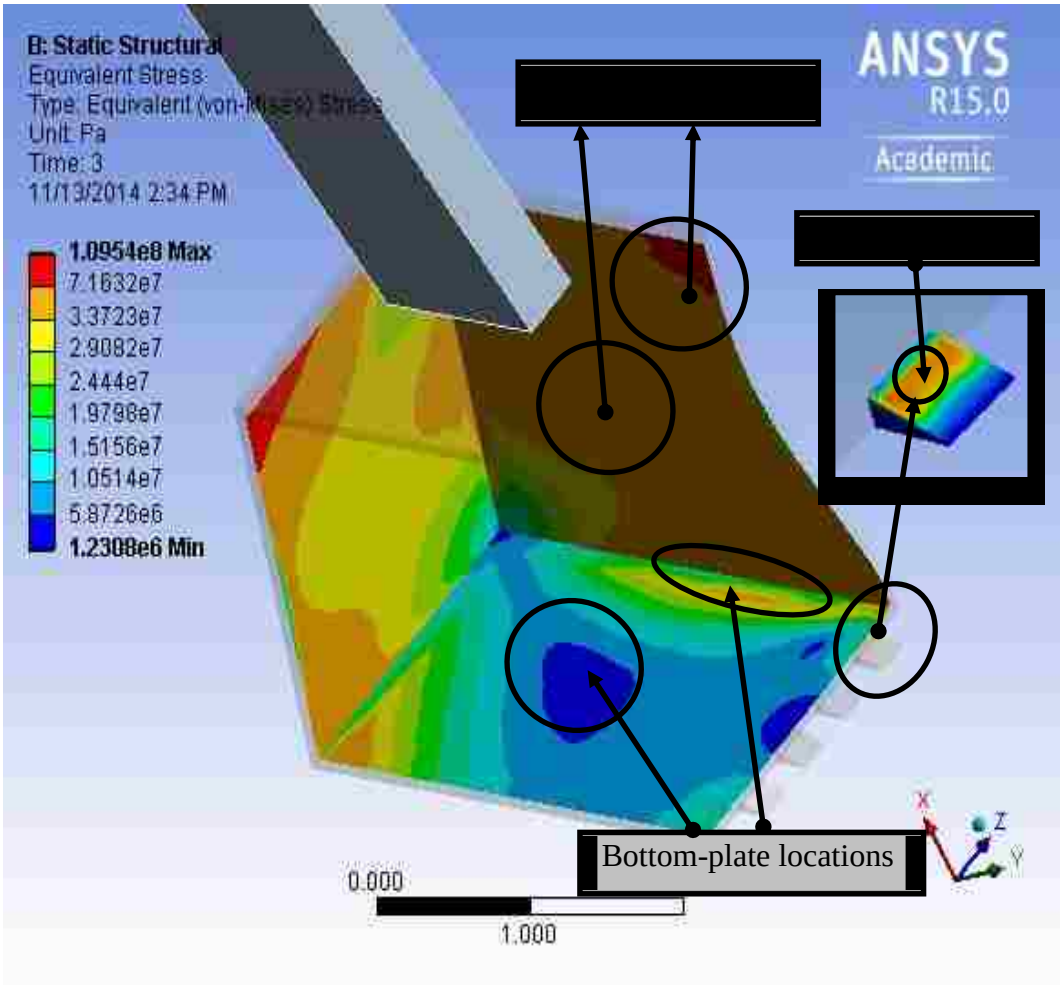

Figure 6.1. Selected locations for crack fracture analysis

Table 6.2. Experimentations-II for Stress Modeling and Analysis

<table>
<tr><th colspan="2">Experiment Series-II: Variation of Material Density</th></tr>
<tr><td>Experimentation</td><td>Description</td></tr>
<tr><td>Variable and Scope</td><td>Variable: Formation density (ρ) Kg/m^3

Scope: Typical densities for common excavation materials
Reference density: 1450

Secondary Variable: Cutting force (as cutting force varies linearly with density)

Scope: Varies directly with density variation

<table>
<tr><th>Material</th><th>Density (Kg/m^3)</th><th>Percent Variation</th><th>Cutting Force Variation</th></tr>
<tr><td>Base Case</td><td>1450</td><td>0</td><td>0</td></tr>
<tr><td>Coal</td><td>1200</td><td>-17%</td><td>-17%</td></tr>
<tr><td>Avg. Soil</td><td>1700</td><td>+17%</td><td>+17%</td></tr>
<tr><td>Copper Ore</td><td>2000</td><td>+38%</td><td>+38%</td></tr>
<tr><td>Limestone</td><td>2400</td><td>+66%</td><td>+66%</td></tr>
<tr><td>Oil-Sands</td><td>2600</td><td>+79%</td><td>+79%</td></tr>
<tr><td>Granit</td><td>2700</td><td>86%</td><td>86%</td></tr>
<tr><td>Iron Ore</td><td>4500</td><td>+210%</td><td>+210%</td></tr>
</table>
</td></tr>
<tr><td>Number of Experiments</td><td>Total number of experiments: 8</td></tr>
<tr><td>Expected Results</td><td>The dipper stresses should vary in proportion with material density. Density variation should have a significant impact on the dipper stress profile as it defines the dipper payload, which is the largest resistive force for dipper.</td></tr>
<tr><td>Significance</td><td>Being the largest contributor to the resistive force, its impact on stress profile is critical to analyze.</td></tr>
</table>

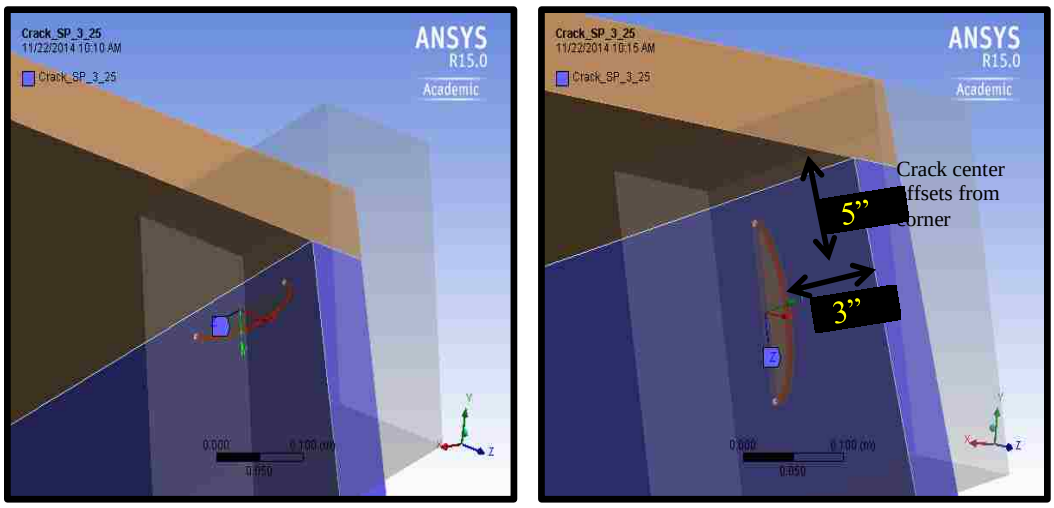

a) locations and orientations for the side-wall top-corner cracks

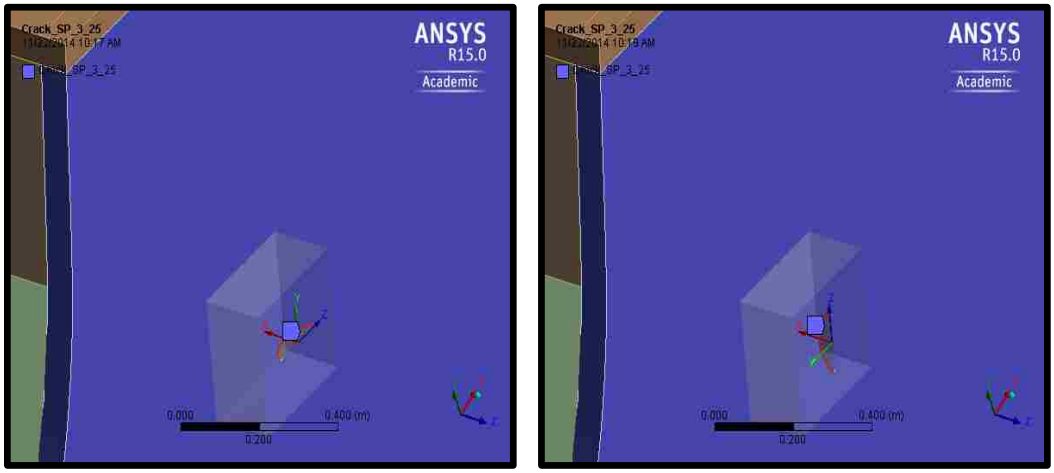

b) locations and orientations for the side-wall center cracks

Figure 6.2. Side-wall crack locations and orientations
a): top-corner b): center of side-wall

Similarly, for the bottom-plate experiments, semi-elliptical cracks are introduced at the center of bottom-plate and at a second location closer to the side-wall. For the central location, cracks are simulated in two orthogonal orientations which are parallel and normal to the side-wall. While for the location closer to side-wall, only one orientation of the crack is simulated. This direction is selected along the maximum stress

intensity direction as was established during the stress profiling of the dipper. These two crack locations, orientations, and the dipper stress profile are shown in Figure 6.3.

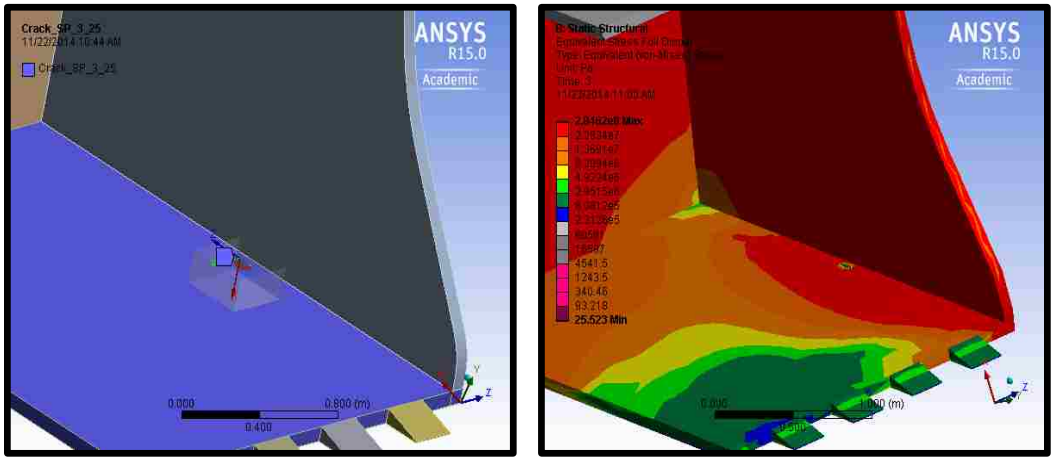

a): location, orientation for bottom-plate crack b): stress profile of dipper

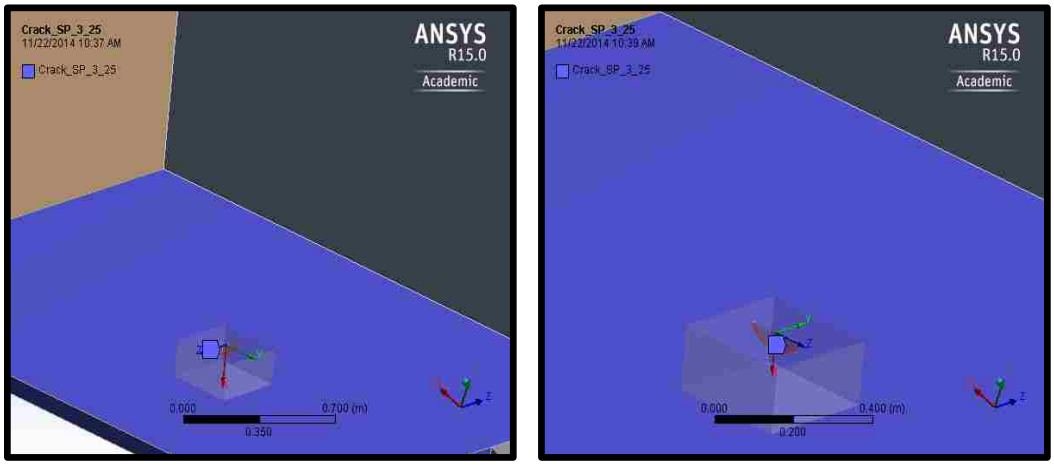

c) locations and orientations for the bottom-plate center cracks

Figure 6.3. Bottom-plate crack locations and orientations
a): closer to side-wall b): dipper stress profile c): center of bottom-plate

These cracks are gradually incremented from a quarter-inch to three inches with a step size of 0.5 inch. The depth of these cracks is incremented to half of the crack-length

every time. The corner-tooth is smaller in size as compared with the bottom-plate or the side-wall. The dipper-teeth are wedge-shaped bodies and the thickness increases continuously towards the dipper-lip. Because of this thickness variation, there can be countless possible scenarios for a crack to appear and propagate. Only one central crack location, with two orthogonal orientations, is tested in these experiments. The crack location and two orientations are shown in Figure 6.4. The crack-lengths are incremented from 0.125 inches to two inches in steps of 0.25 inches.

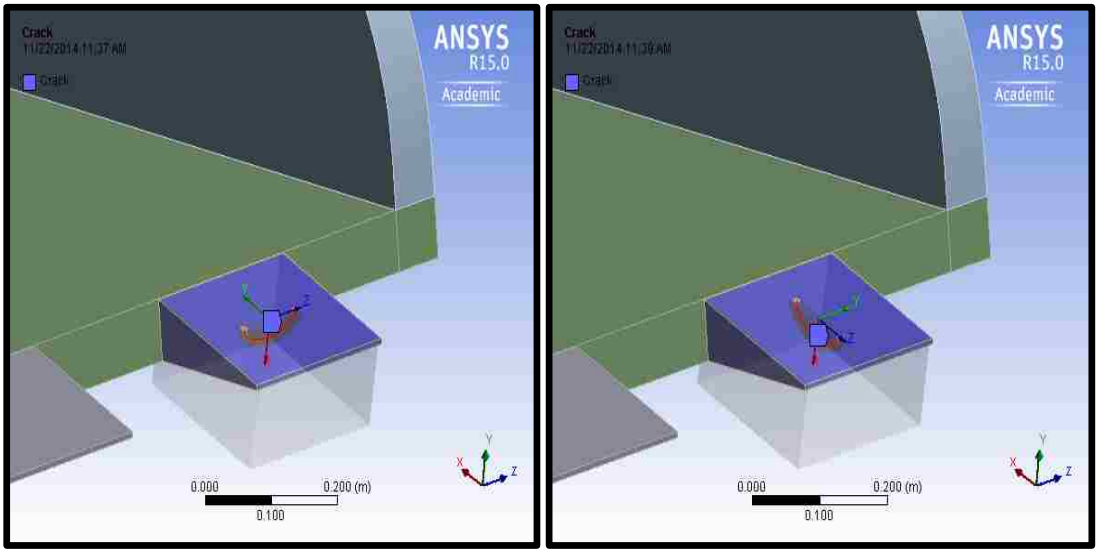

Figure 6.4. Corner-tooth crack location and orientations

The crack definition is explained in Figure 6.5 for the above experiments. For each crack, a localized coordinate frame is assigned at a point that serves as the center of semi-elliptical crack. The crack-length (major radius of ellipse) and the crack-depth (minor radius of ellipse) are defined along the Z and positive X directions, respectively. The crack-width is measured along the Y direction. The center and the two radii define

the shape of the crack-front. This crack front is divided into a number of segments and six circular contours are generated around the crack front. The circular contours are divided in segments as well. All these divisions represent the node locations for the finite element model. The J-integral values are computed for every contour along the crack-front. These values are used to compute the SIFs at the crack-tip and for life estimations.

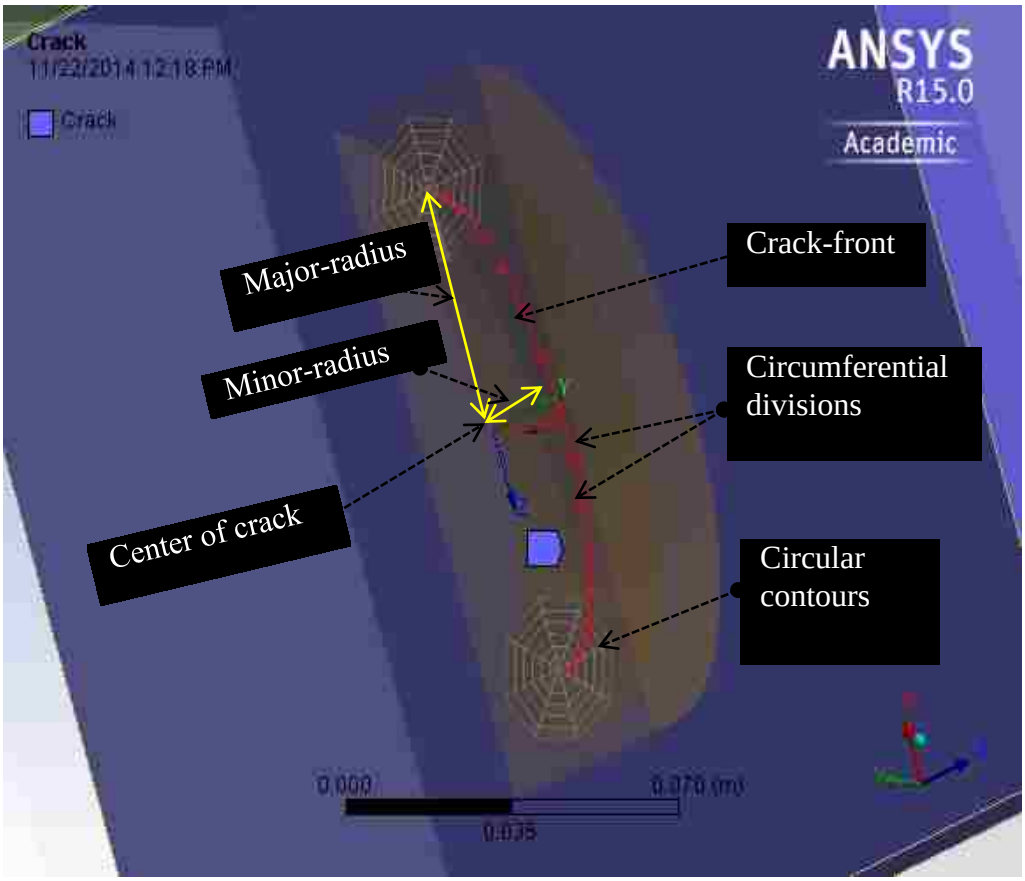

Figure 6.5. Crack definition in ANSYS for J-integral computations

Crack size is the most critical aspect of this fatigue crack modeling and dipper life-estimation. The SIFs are highly dependent upon the crack-size (length and depth).

The relationship between SIF and crack length is not linear. Estimating the variation of SIFs with size is the most important and critical aspect for life-estimation.

The series of experimentations conducted for the fatigue crack-simulations and life-estimations are summarized in Table 6.3.

Table 6.3. Experimentation for Fracture Modeling and Analysis

Crack Location	**Description**
Side-Wall Crack	Description: SIF computations and life-estimations for cracks at selected locations for the side-wall Variable: crack size Orientation Scope: Sizes: 0.25″, 0.5″, 0.75” 1.00″, 1.5”, 2.0″, 3.0” Orientation: Parallel to Bottom-Plate Normal to Bottom-Plate No. of Experiments: 28
Bottom-Plate Crack	Description: SIF computations and life-estimations for cracks at selected locations for crack in the bottom-plate. Variable: crack size Orientation Scope: Sizes: 0.25″, 0.5″, 0.75” 1.00″, 1.5”, 2.0″, 3.0” Orientation: Parallel to Bottom-Plate Normal to Bottom-Plate No. of Experiments: 21

Table 6.3. Experimentation for Fracture Modeling and Analysis (Cont.)

Tooth Crack	Description: SIF computations and life-estimations for cracks at selected location on the corner-tooth Variable: crack size Orientation Scope: Sizes: 0.125”, 0.25″, 0.5″, 0.75”, 1.00″, 1.25”, 1.5″, 1.75”, 2.0″ Orientation: Parallel to Bottom-Plate Normal to Bottom-Plate No. of Experiments: 18
Significance	To establish the relationship between SIF and crack length (a vs ΔK) To establish relationship between rate of change of crack-length and SIF ($\Delta a/\Delta N$ vs ΔK) To estimate the remaining life of component (N_f)
Expected Results	The SIF should increase with crack length and should show a logarithmic relationship between rate of change of crack-length and SIF ($\Delta a/\Delta N$ vs $\log\Delta K$ should be a straight line) as in Paris Law (Paris and Erdogan, 1963) Cracks in one orientation should grow more rapidly than the other orientation

6.5. SUMMARY AND CONCLUSIONS

A detailed experimental design and procedure is adopted to test the important field and operational parameters related to dipper stress analysis and fatigue life expectancy. The experimental design objectives and process are explained in this section. The experimentation is conducted through simulations run in ANSYS R15 environment. Appropriate force and maximum DOF criterion are set, with tolerance limits, to obtain

balanced converged solutions. The computations are expensive and long. Missouri S&T's high computing facility (HPC, 2014) is used to run the simulations. A series of experiments is designed and run to test each parameter.

The dipper's stress loading profile is tested for varying density and cutting resistance conditions. In the first series of experiments, the experiments are design to test the impact of formation density on dipper stress profile. Common excavated materials (coal, soil, copper ore, limestone, oil-sands, granite, and iron ore) with large shovels are selected for this purpose. Similarly, the second series of experiments is designed to test the impact of C_o parameter on dipper stress loading. This is the only field related parameter in the cutting forced model by Zelenin et al. (1985). The experiments are designed to vary this parameter from 5 to 20.

A separate series of experiments is designed to estimate the fatigue lives for dipper components. This is achieved by establishing prelateships between stress intensity factors (SIFs) and crack-lengths for various locations and components of the dipper. The locations are selected using the stress variation analysis and include the critical (high stressed) regions on dipper-teeth assembly and the central locations for dipper side-wall, bottom-plate and teeth. Pre-defined elliptical cracks are introduced at these locations in two orthogonal directions. The crack-lengths for these cracks is varied from a small crack-length to a larger crack-length in both orthogonal directions.

7. RESULTS AND DISCUSSIONS

The data obtained through the experimentation process is processed into useful information for the stress and fracture failure modeling of the shovel dipper-teeth assembly. The data collected from the numerical simulation and virtual prototyping is based on P&H 4100 XPC cable shovel. This section presents and discusses the important results gathered from the experimentation process.

The steel used for cable shovel dippers and teeth has high strength properties. The yield strength is specially the most important strength property, as the shovel experiences high levels of stress loading. A complete data sheet for the steel type used is not readily available in literature. Yin et al. (2008) investigated the fatigue life of a cracked boom. They reported the steel for boom was csa-g40.21-350WT. This steel has steel high yield strength of 320 MPa (SSAB, 2009). For this research it is assumed that the steel used for dipper is the same as used for the shovel boom. The steel properties used for this research are given in Table 7.1.

7.1. NUMERICAL SIMULATION RESULTS

The numerical simulation of kinematic and dynamic model of the shovel dipper-teeth assembly is performed in MATLAB/Simulink environment. The numerical simulation model consists of a number of sub-models and are explained in Section 5.0. These sub-models generate data on individual joint and link displacements, velocities, accelerations, forces, and torques. The two important data outputs from these sub-model simulations are the external resistive forces, and the force and torque requirements for shovel to overcome these resistive forces.

Table 7.1. Properties of Steel for Dipper and Teeth

Property	Value	Unit
Density	7900	Kg/m3
Young's Modulus	2.3E+11	Pa
Poisson's Ratio	0.3	
Tensile Yield Strength	3.2E08	Pa
Compressive Yield Strength	3E08	Pa
Tensile Ultimate Strength	4.6E+08	Pa

7.1.1. Material Resistive Forces. The external resistive forces acting on the dipper-teeth assembly during the excavation cycle are shown Figure 7.1. The diagram illustrates that the digging resistive forces increase continuously, but not linearly, during the digging cycle and peak at around 2.5 second. At this instance, the dipper arm is just above the horizontal and is at its maximum depth into the bench. The tangential force (F_t) is at its maximum at this moment, as the dipper teeth are almost vertical into the formation. While, the normal force (F_n) becomes a local minimum at this time moment. Furthermore, it is observed that at the start of the digging cycle, the normal force is larger than the tangential force and both of these forces increase with time. However, at time 2-seconds from the start of digging cycle the tangential forces become greater than the normal forces. At this time instant, the dipper teeth are almost vertical into the bench and experience the maximum forces. As the dipper continues to move upward along the trajectory, the teeth direction tangential forces start to decrease as well.

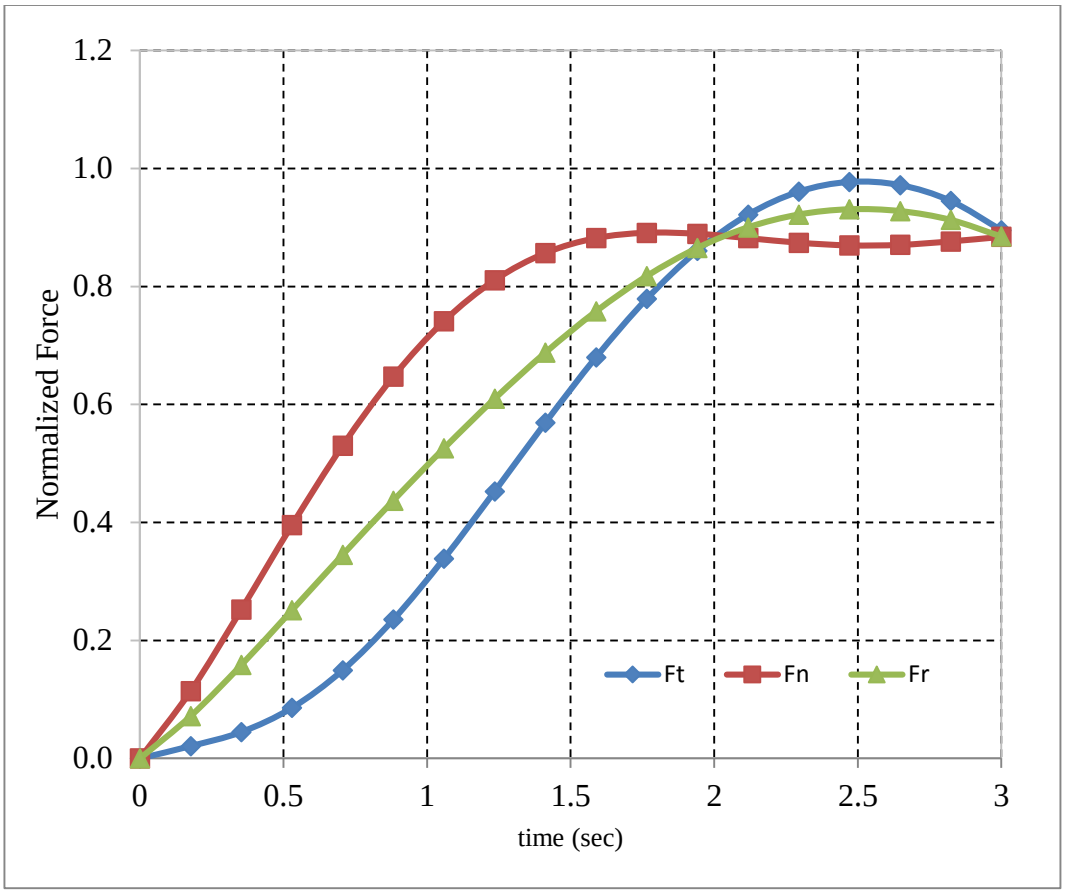

Figure 7.1. Material resistive forces acting on the dipper

7.1.2. Crowd-Force and Hoist-Torque. The hoist torque and crowd-force are computed during the simulation process, as the dipper traverses through the trajectory. The hoist torque and force requirements for P&H 4100XPC shovel are shown in Figure 7.2. The hoist torque requirements increase continuously as dipper traverses the trajectory and is filled with material. The maximum torque requirement is around 2.1 seconds. It is consistent with the fact that the maximum resistive digging forces act on the dipper at this instant and that the dipper-arm is at its maximum extension.

The dynamic model and simulation in MATLAB presents certain advantages over a virtual prototype model. The most important being the flexibility to apply to a wide

range of shovel dipper sizes and geometries. The model flexibility comes from the fact that shovel dimensions, material properties, excavated material models are all defined as separate MATLAB files in the simulated model. The model can also be used for quicker analysis for the shovel energy requirements for a multiple bench geometries and material properties.

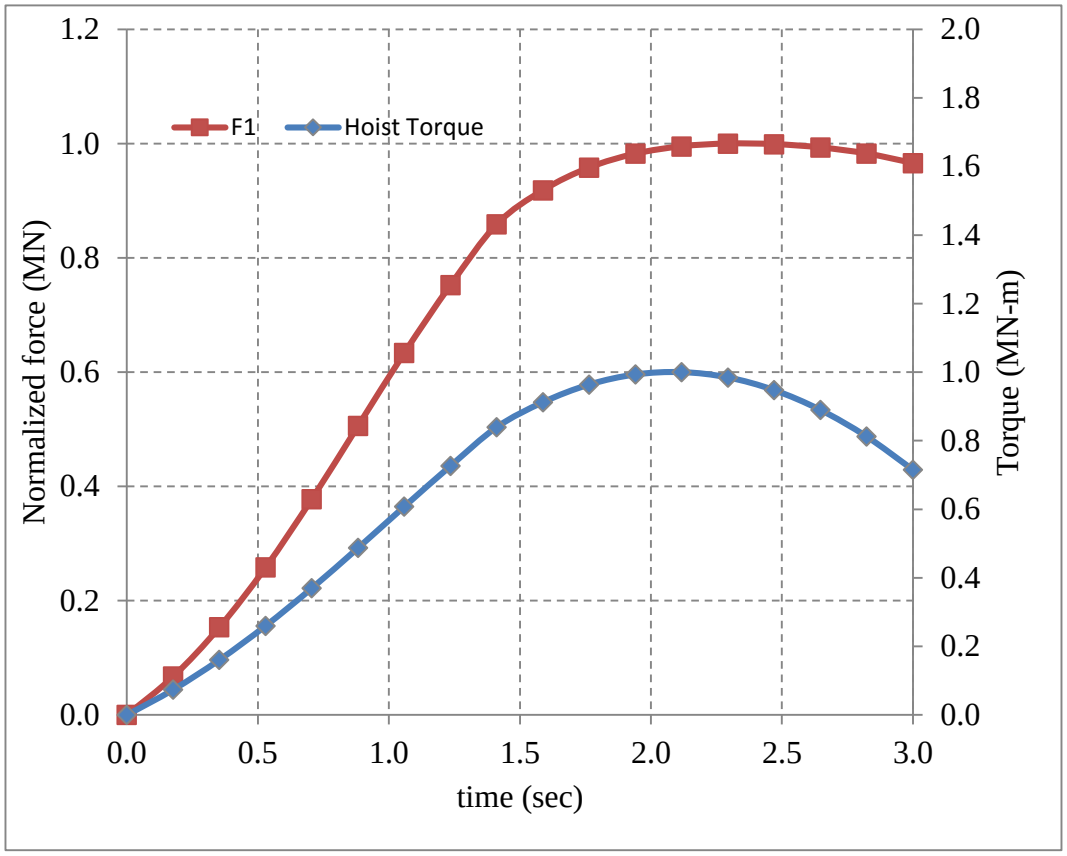

Figure 7.2. Crowd force and hoist torque for shovel

7.2. DIPPER-TEETH STRESS ANALYSIS

The virtual prototype model of the dipper-teeth assembly for the P&H4100XPC shovel is built using Autocad and ANSYS R15 platforms. The angular rotation and

extension of the dipper arm, external digging forces, and dynamic material weight forces from the dynamic simulated model are used as inputs for this virtual prototype. A transient/structural analysis is performed in ANSYS Workbench (R15). Two series of experiments are performed to determine the dipper-teeth assembly stress profile. In these series of experiments, the impact of "Co" and material density variation is measured on dipper-teeth assembly stress loading. Stress loading for the full dipper-teeth assembly, dipper bottom-plate, dipper side-wall, and teeth is computed for each experiment. The representative stress profiles are shown in Figure 7.3 and Figure 7.4. The stress contour maps are used to identify the high and lower stress regions to be used for fatigue fracture modeling and analysis.

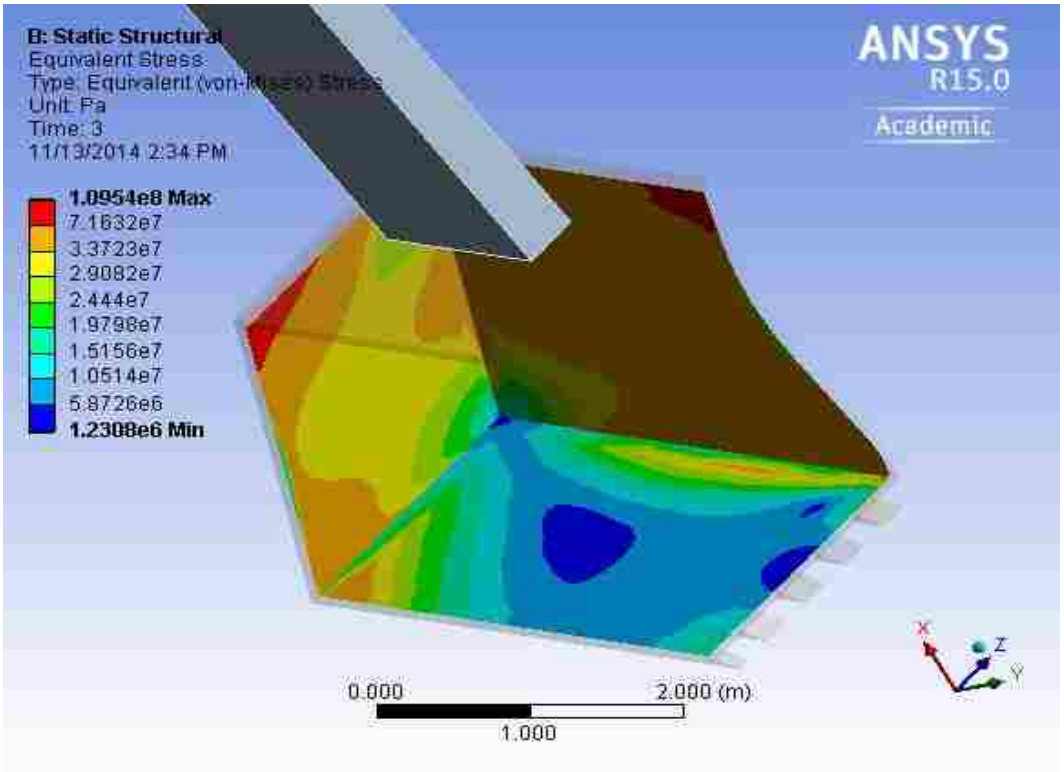

Figure 7.3. Equivalent stress (von-Mises) profile of dipper-teeth assembly

The stresses on the dipper-teeth assembly vary with time. The equivalent stress variation for the dipper-teeth assembly is shown in Figure 7.5. The stress profiles in Figures 7.3 and 7.4 are shown at the end of the simulation time only. A detailed stress distribution is given later in this section.

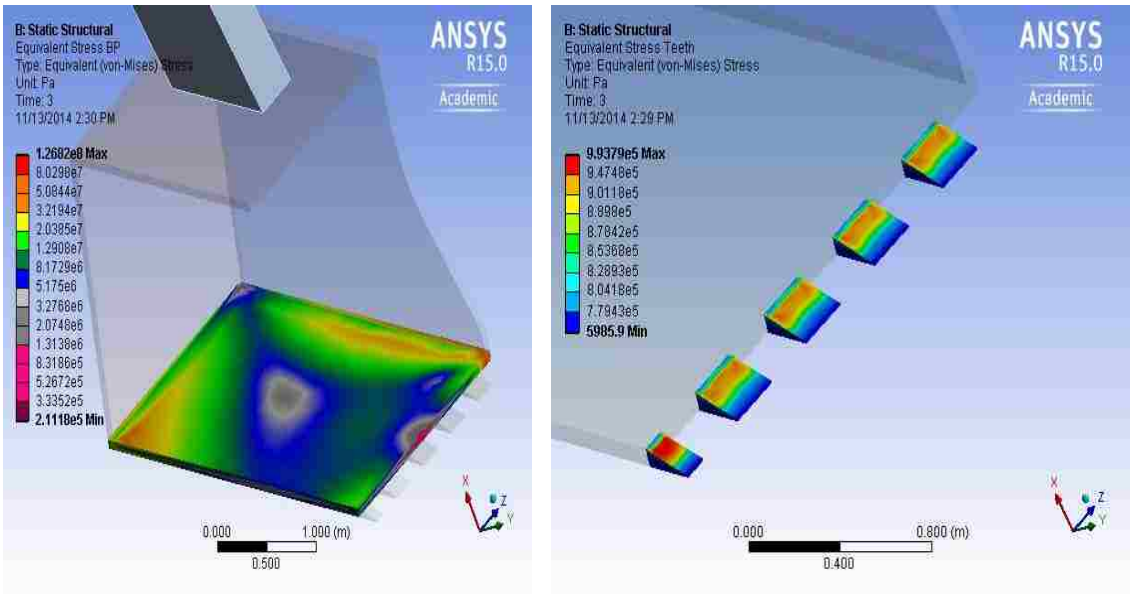

Figure 7.4. Equivalent stress (von-Mises) for dipper bottom-plate and teeth

The contour maps present a great visual tool to identify the regions of high and low stress on dipper components. As shown in Figure 7.3, the side-wall experiences high stress during the excavation process. The top-corner is under a high stress than the rest of the side-wall. The stress on the rest of the side-wall is fairly uniform, except for the bottom corner, which shows lighter stress load. These areas become the focus for the fracture analysis.

The bottom-plate shows a variation of stress. The stresses are at their minimum at the center of plate, while increate towards the side-wall and back-plate. The areas adjacent to the side-wall and the back-plate show local high stress loading. The area adjacent to the side-wall is selected for crack fatigue simulation and analysis.

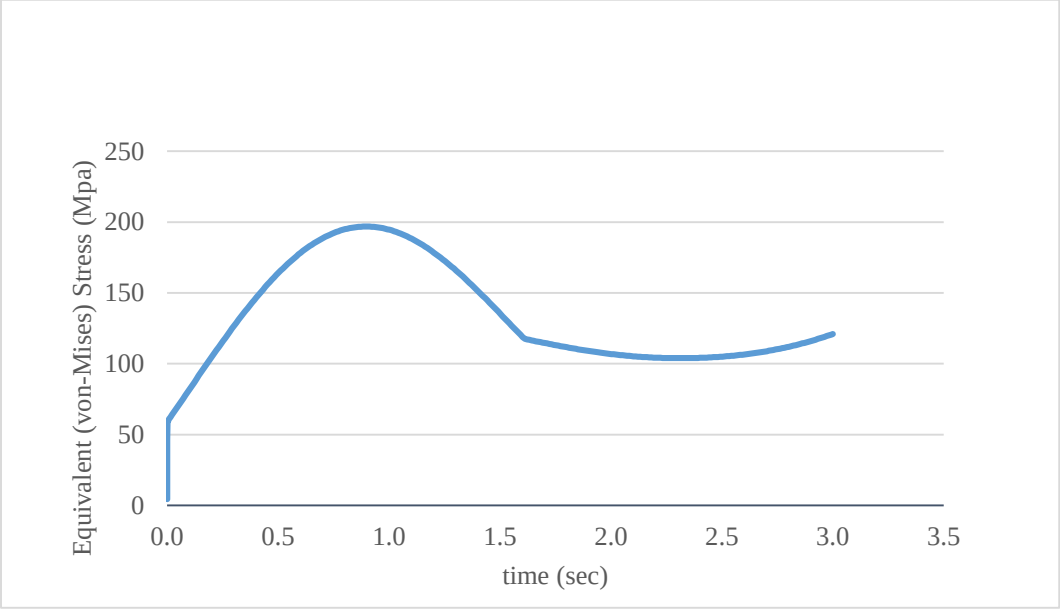

Figure 7.5. Equivalent stress (von-Mises) variation for dipper-teeth assembly

The dipper back-plate shows regions of high stress loading. On an actual dipper, the back-plate has a door for ore release. The door and door-trip mechanism are not modeled in this simplified dipper. Therefore, the back-plate high stress areas are not included in the fatigue fracture modeling.

The teeth also show areas of low and high stress loading. The stresses on the teeth are significantly lower than the rest of the dipper body. Despite, the lower stress values, the teeth are analyzed for fatigue fracture.

The stress profile of the dipper and its components is highly dependent on the force models for these components. The stress profiles agree with the force loading of the components. The side plate is subjected to side pressure due to payload following the passive earth pressure theory. The teeth are modeled as subjected to the tangential and normal cutting resistance forces only. These forces are significantly lower than the payload or dipper self-weight. Therefore, the stresses on the teeth are lighter than the dipper body.

These maximum equivalent (von-Mises) stresses need to be tested for the yield strengths of the steel. In the above figures, the maximum equivalent stress is 140Mpa which is lesser than the yield strength of high carbon steels (250MPa) and also lesser than the steel properties considered for the dipper material.

7.2.1. Impact of Material Density on Dipper's Stress Profile. Material density is one of the most important field variables for shovel excavation. A series of experimentation is performed to analyze the impact of material density on dipper stress profile. Dipper stress profile is measured for the full dipper body, the side-wall, and the bottom-plate. Material density is selected for the common excavated materials with large cable shovels including coal, copper ore, oil-sands, limestone, granite, iron, and soil. Figure 7.6 illustrates the equivalent (von-Mises) stresses computed for the dipper-teeth assembly for common material densities. The box plot in Figure 7.6 shows the interquartile region (3^{rd} quartile – 2^{nd} quartile or 75^{th} percentile – 25^{th} percentile) and the extreme equivalent stress values on the dipper-teeth assembly. The stress distribution represents the total stress variation over the 3-sec simulation period for all elements of the dipper-teeth assembly. The materials listed on the horizontal axis are in an ascending order in terms of density values. The data show that equivalent stress values increase with

material density. The stress distribution is positively skewed and the skewness increases with density. This can be interpreted as that a majority of the dipper-teeth assembly regions (nodes of finite element model) experience higher stress loading than the average stress when digging denser materials.

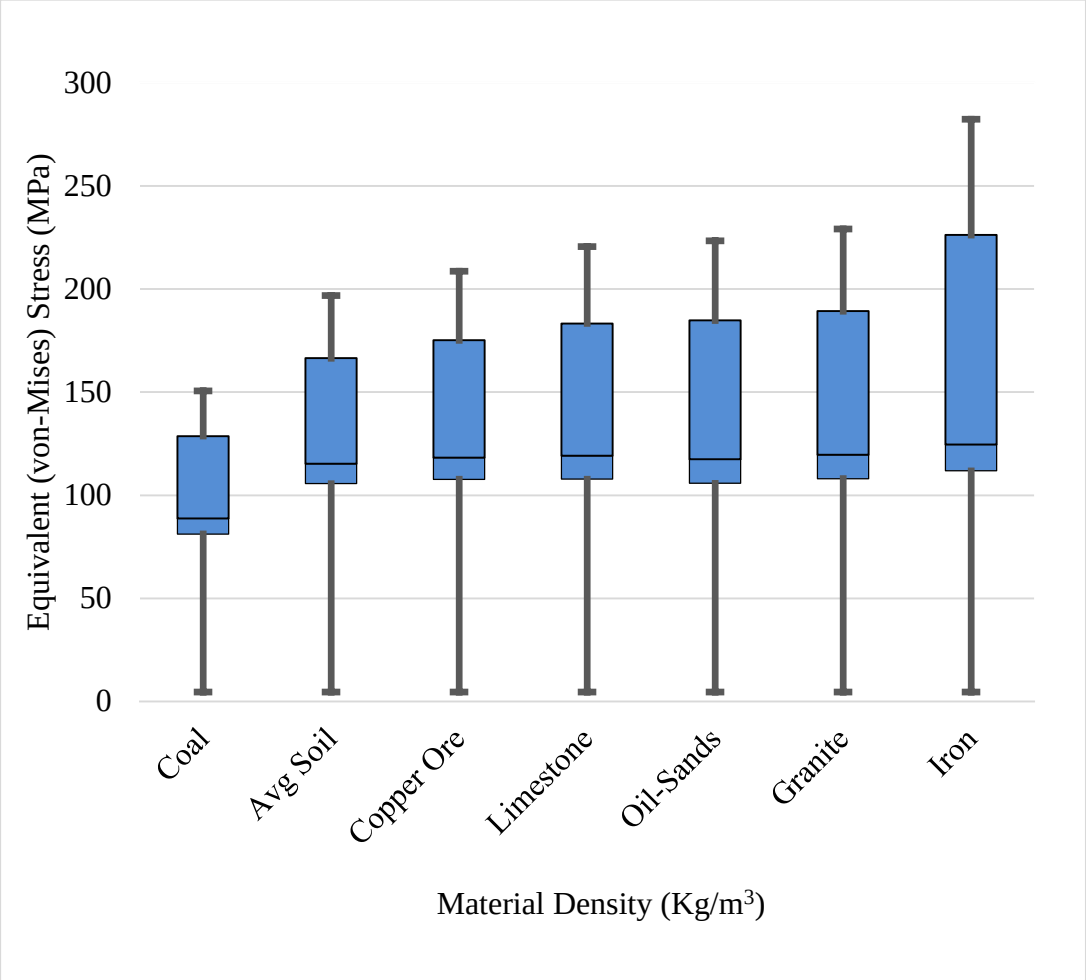

Figure 7.6. Equivalent stress (von-Mises) distributions for dipper-teeth assembly

The maximum stress values vary from 151MPa to 282MPa. These stress values are higher than the lower limits of yield strengths for low, medium, and high carbon steel

(Table 7.2). Permanent damage to the dipper components is possible, if the steel used has a lower yield strength than his very high stress on dipper body.

Table 7.2. Yield Strengths of Steel (matweb, 2014)

Steel	**Yield Strength (MPa)**
Low carbon steel	140-2400
Medium carbon steel	245-1740
High carbon steel	275-3340

A similar trend is observed for the dipper side-wall and bottom-plate stress profiles. Figure 7.7 illustrates the equivalent stress variations for dipper side-wall for the common material densities. It is observed that the dipper's side-wall shows a higher level of stress loading in the whole dipper-teeth assembly as compared with the other dipper plates and teeth. Further, it can be seen that the stress loading for the side-wall increases with material density. The side-wall shows similar stress distributions as shown by the full dipper-teeth assembly for the same material densities. A comparison of the stress distributions for dipper-teeth assembly and for side-wall shows that side-wall stresses actually define the stress profile of whole dipper-teeth assembly. This is due to the reason that the extreme and mean stress levels for dipper-teeth assembly match with that of the side-wall. The maximum stress values for side-wall range from 151 – 282MPa. Again, these values are higher than the lower limits of yield strength for low, medium, and high carbon steel.

The stress profiles for dipper bottom-plate are shown in Figure 7.8 for common material densities. An increasing trend in stress loading is observed with material density. The maximum stress values are lower than the dipper side-wall values. The distributions represent positive skewness. The maximum stress levels are almost two-third of that stress levels for dipper side-wall as can be seen in Figure 7.10.

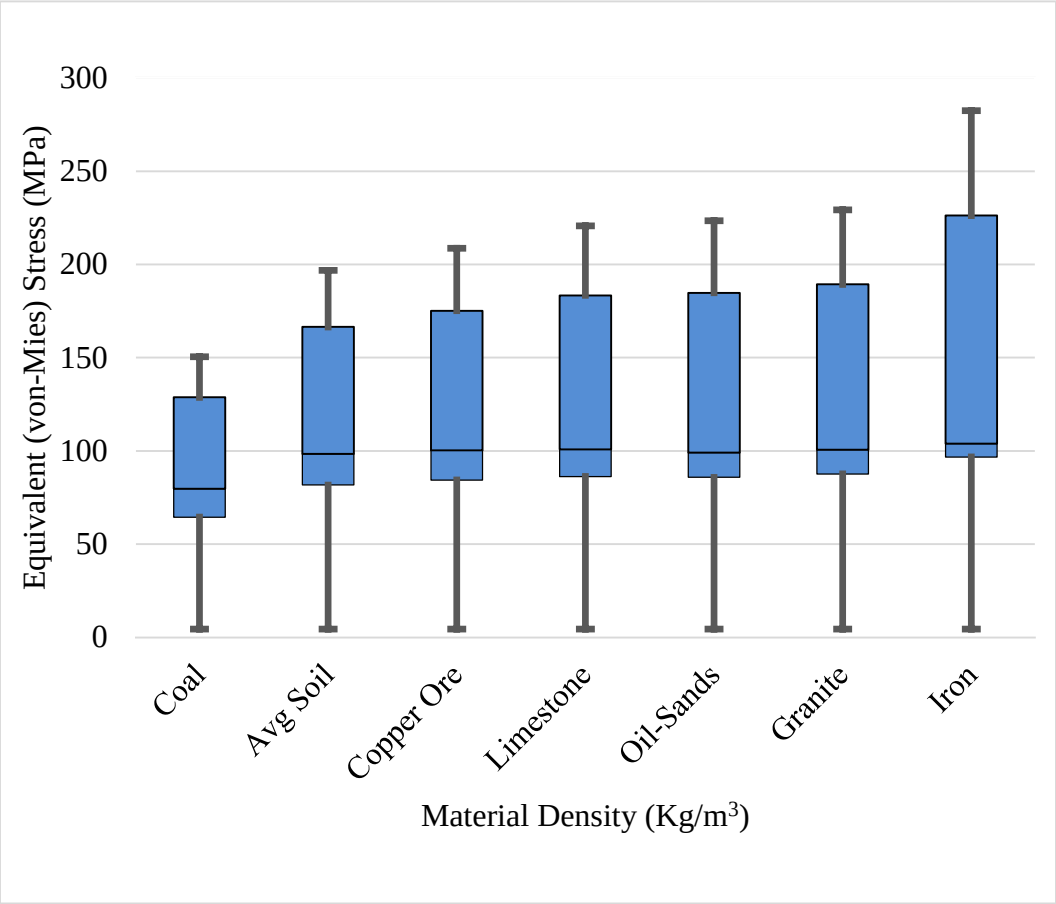

Figure 7.7. Equivalent stress (von-Mises) distributions for dipper side-wall

The maximum stress values for bottom-plate range from 97 MPa to 164MPa. The maximum stresses are higher than the lower limits for low carbon steel.

The stress profile distributions for the teeth are illustrated in Figure 7.9. The stress levels are lower. However, an increasing trend with material density is evident. The distributions are negatively skewed, suggesting that majority of the regions (nodes) experience lesser stress than the average stress value for teeth.

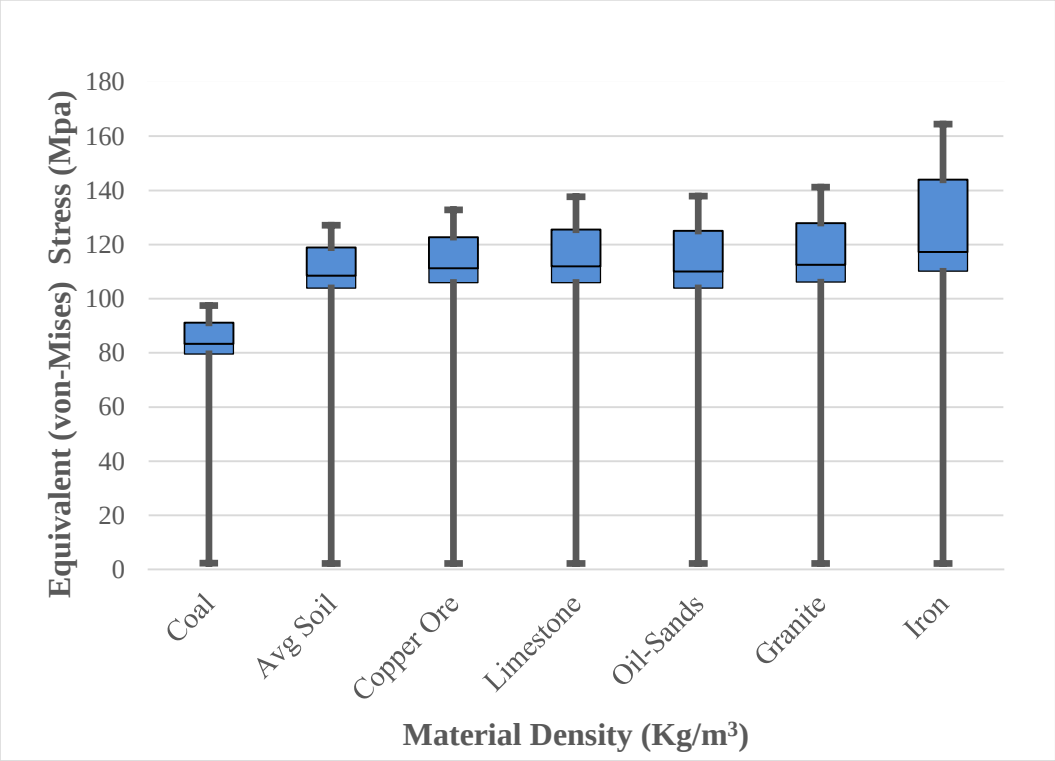

Figure 7.8. Equivalent stress (von-Mises) distributions for dipper bottom-plate

The maximum stress levels range from 1.2MPa to 4.5MPa. These stresses are very low and no yield is expected in the teeth material. The maximum stress values for all the dipper components is plotted against material densities in Figure 7.10. For dipper stress profile, the maximum stresses are most important to compute as they can cause the dipper failure if exceed the material yield strengths. It is observed that the maximum stress levels

increase with material density. For the dipper side-wall and the bottom-plate the relationship between the maximum stress level and material density is cubic. While, for dipper teeth the relationship is linear.

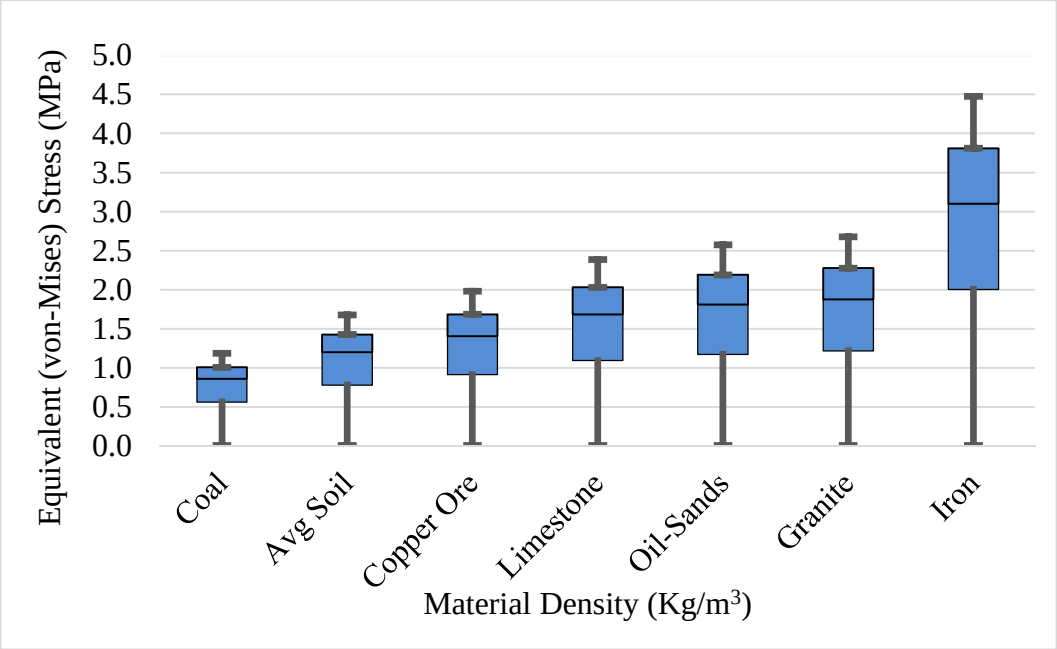

Figure 7.9. Equivalent stress (von-Mises) distributions for teeth

7.2.2. Impact of C_o on Dipper's Stress Profile. The empirical model of Zelenin et al. (1985) is used to model the cutting resistance on dipper-teeth assembly. An important parameter in this model is "C_o", which represents the number of blows of a penetrometer into the soil. Being the only formation related parameter; it plays a critical role for digging force computations. The values can vary from 1 to 30 for unfrozen soil and 30-360 for frozen soil. The unfrozen soils are further subdivided into four categories, based on the 'C_o" values. A reference value of 10 is selected to represent well blasted

material. During the experimentation, the values of C_o are varied from 5 to 20 to analyze the impact of this variable on dipper's stress profile.

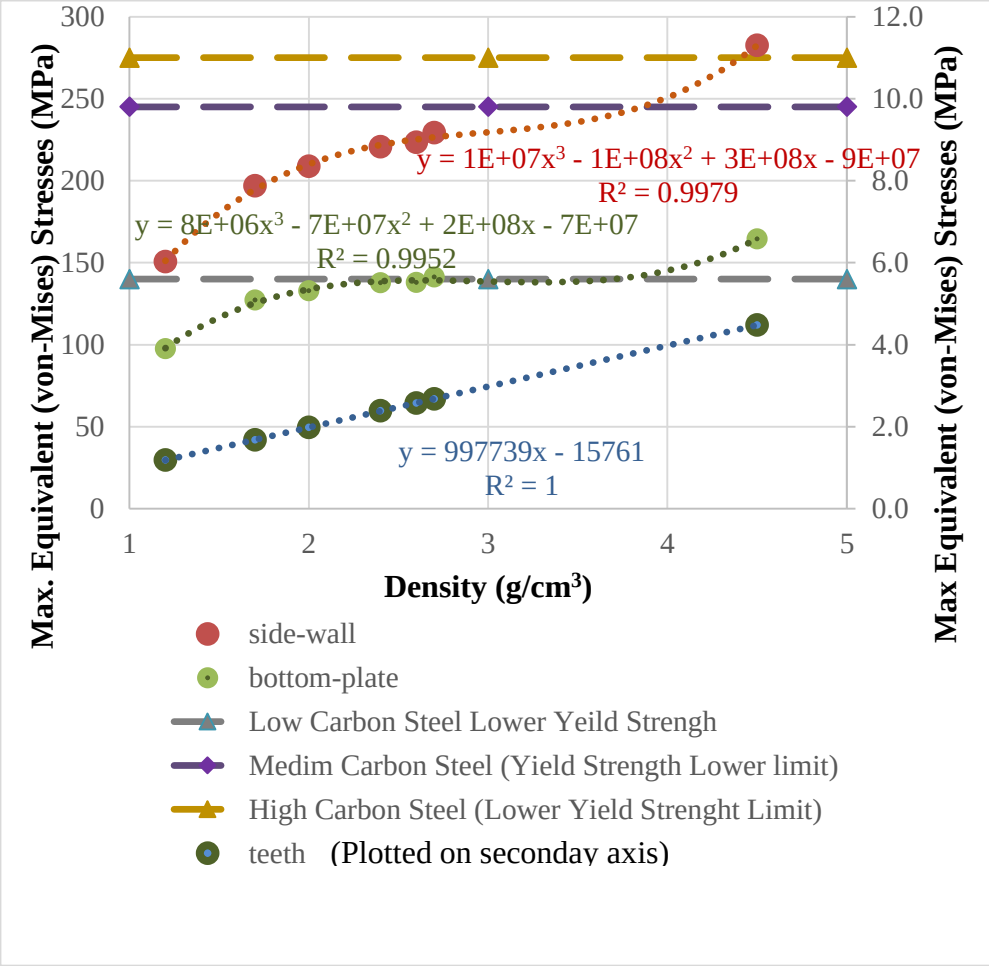

Figure 7.10. Maximum equivalent stress (von-Mises) levels

The maximum equivalent (von-Mises) stress values for the dipper-teeth assembly, dipper bottom-plate, and teeth are shown in Figure 7.11. The data show an increasing trend in the maximum stress values with C_o values. A linear relation between maximum stress values and C_o exists as shown in Figure 7.11. The regression coefficient values

indicate a better linear model fit for the stress levels on teeth as compared with the maximum stress levels of dipper-teeth assembly and dipper bottom-plate. The digging resistive forces are smaller in magnitude as compared with the material weight forces. Therefore, the impact of C_o values has a more profound impact on stress profile of the teeth. The stress distributions for teeth are shown in Figure 7.12. The stress distributions show an increase in the equivalent stress values with increase in C_o values. The distributions are negatively skewed and the spread increases with C_o values. The stress distributions for dipper-teeth assembly, side-wall, and bottom-plate are shown Figure 7.13, Figure 7.14, and Figure 7.8 respectively. Similar data trends are observed for stress variations with C_o as were observed for stress variation with material density.

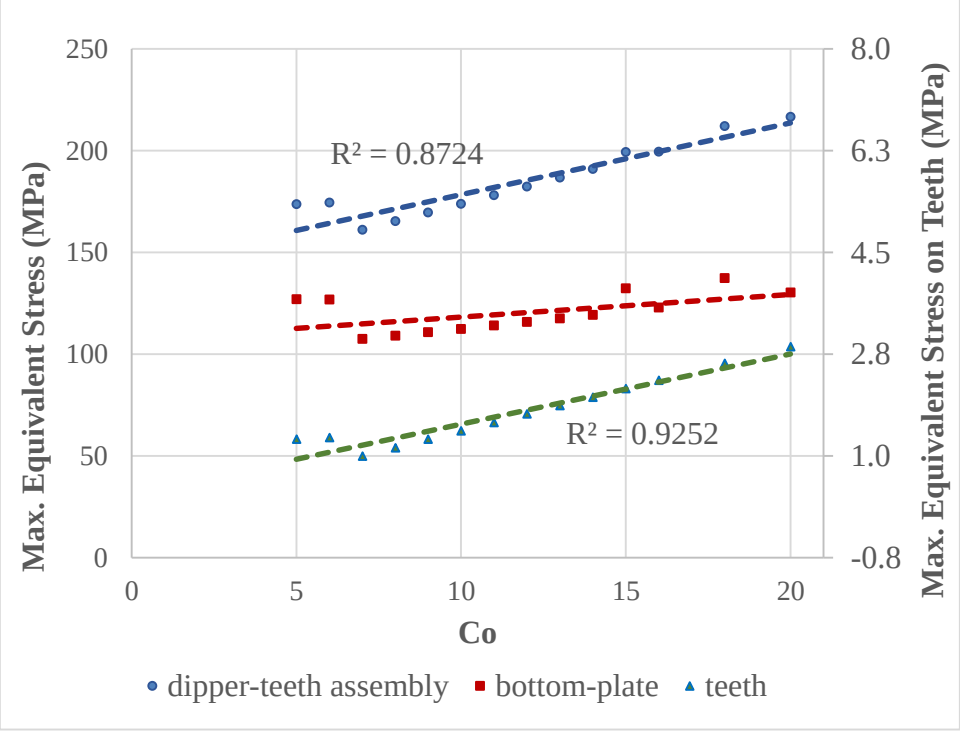

Figure 7.11.Maximum equivalent stress (von-Mises) for dipper components

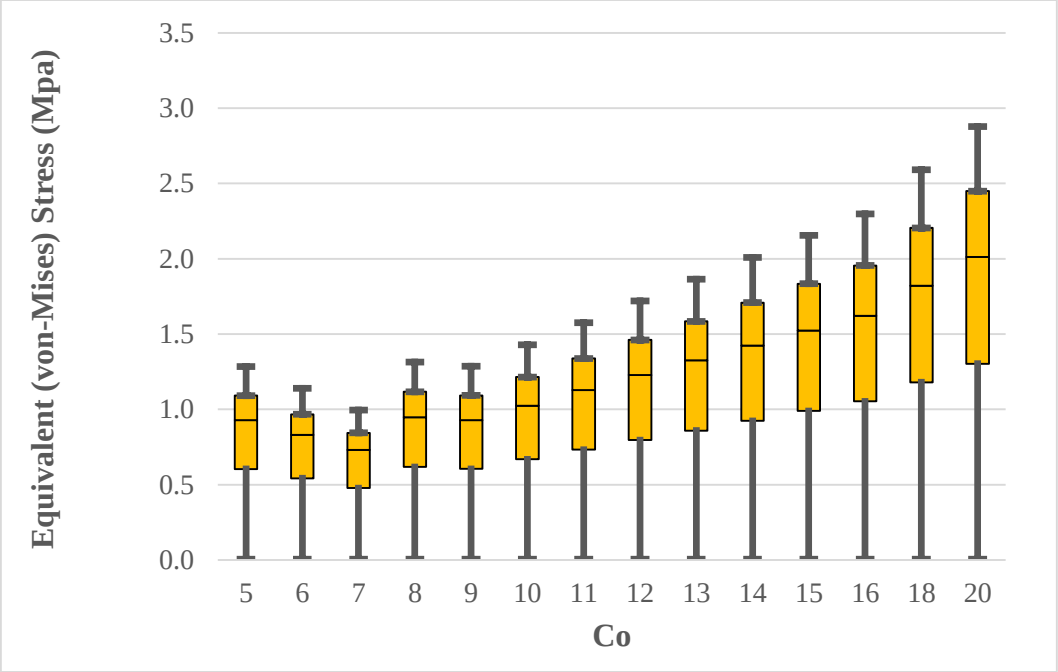

Figure 7.12. Equivalent stress (von-Mises) for dipper teeth

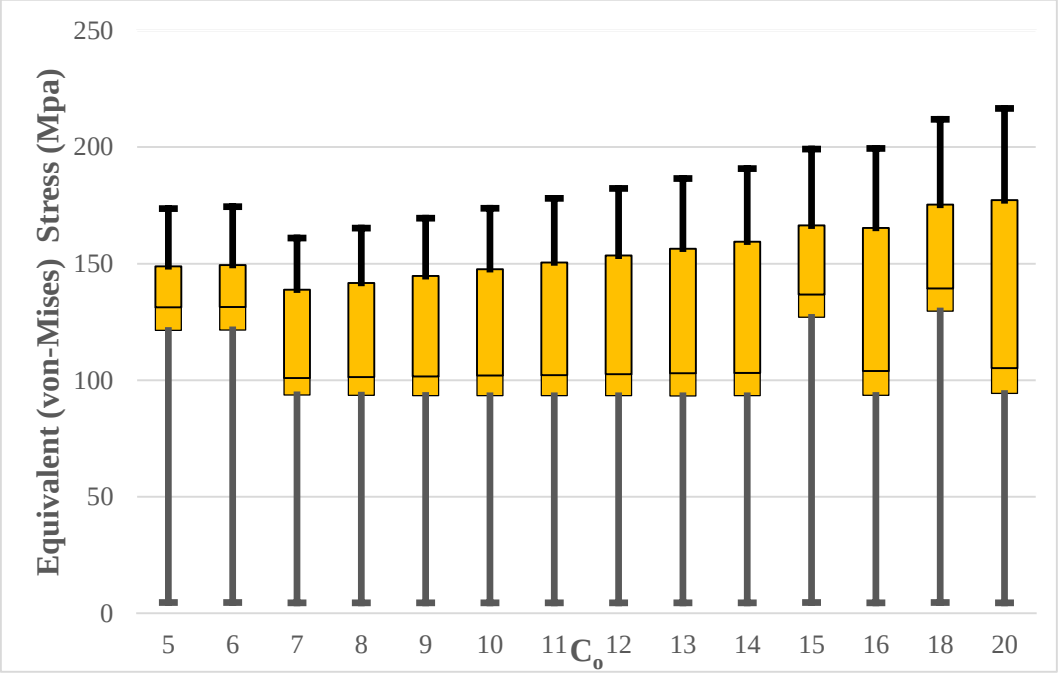

Figure 7.13.Equivalent stress (von-Mises) for dipper-teeth assembly

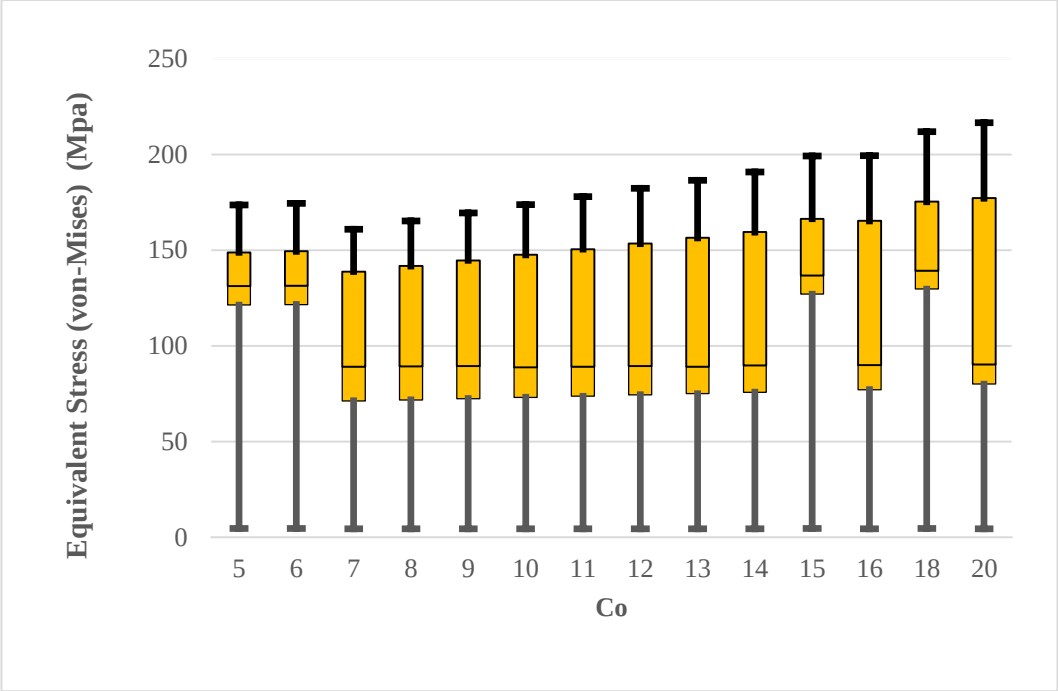

Figure 7.14. Equivalent stress (von-Mises) for dipper side-wall

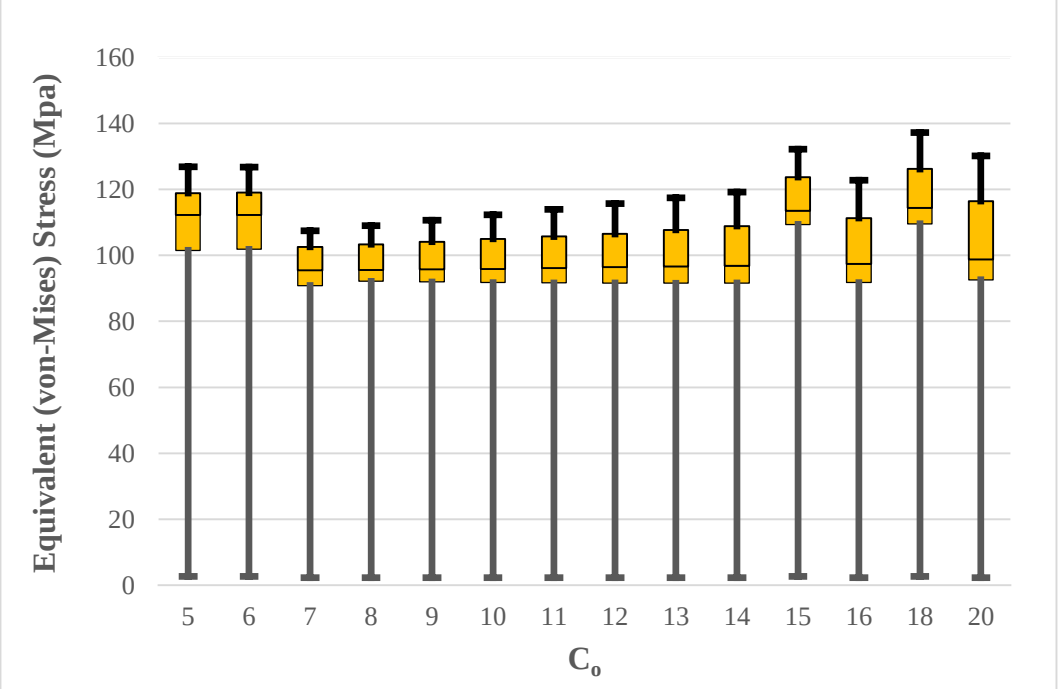

Figure 7.15. Equivalent stress (von-Mises) for dipper bottom-plate

7.3. FRACTURE MODELING AND LIFE EXPECTANCY

Before fracture mechanics evolved, high cycle fatigue using the S-N curves, was the only method considered for the metal fatigue failure. Structural failure due to fatigue cracking is now considered one of the major failure types in metal structure. The local stresses at the crack-tips of these cracks can be high enough to cause the crack to grow to critical extents. At critical extents the material behavior becomes plastic at the crack-tip and it leads to rapid, often brittle, failure. Before the critical length, the material behavior is elastic and linear elastic theories are applicable. According to the linear elastic fracture mechanics (LEFM) theory, computations of stress intensity factor (SIF) at the crack-tip is necessary to predict the crack growth. SIFs for many simple geometries and loading situations are available in published literature (Loadkimidis and Theocaris, 1978; Raju and Newman, 1997; Sih, 1973; Tada et al., 1973). For complex geometries and stress loading conditions, numerical methods are the only way to compute the reliable SIF values.

7.3.1. Finite Element Computation of SIFs. There are three approaches to compute the SIFs using finite element models. These approaches include the displacement methods, the stress methods, and the energy method.

The energy method is one of the most commonly used methods for SIFs. This method computes J-integrals over a closed path around the crack-tip to compute SIFs. The J-integral approach was introduced by Rice (1968a and 1968b). According to this method, the J-integral is computed, as in equation (7.1), over a closed path (contour Γ) around a crack-tip as illustrated in Figure 7.16.

$$J = \int_{\Gamma} \left(W \partial y - T \frac{\partial u}{\partial x} \partial x\right) \tag{7.1}$$

The strain-energy density function "W" for the infinitesimally small strain tensor (ϵ_{ij}) is defined as equation (7.2).

$$J = \int_0^{\in} (\sigma_{ij} \partial \varepsilon_{ij}) \tag{7.2}$$

Rice (1968a and 1968b) showed that the energy release rate, computed through this J-integral, is proportional to the mode-I (K1) SIF. For plain strain conditions the K_1 is defined as equation (7.3) and for plain strain conditions as equation (7.4).

$$K_1 = \sqrt{J \frac{E}{1 - \upsilon^2}} \tag{7.3}$$

$$K_1 = \sqrt{JE} \tag{7.4}$$

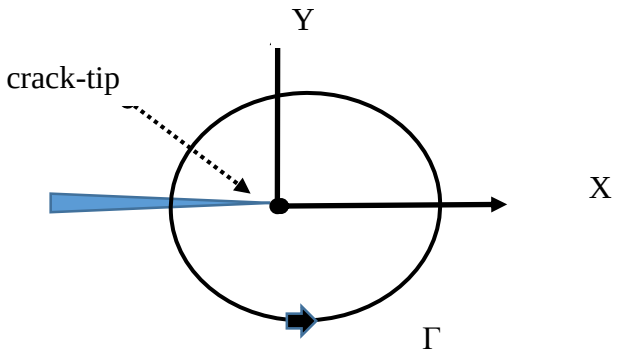

Figure 7.16. Computation of J-integral around a crack-tip

ANSYS R15 software is used to compute the J-integrals around the pre-defined crack-tips. As explained in Figure 6.5, contours are generated around the crack-front to represent the closed-paths for J-integral. There are six contours around every modeled

crack as illustrated in Figure 7.17. A very fine mesh size is generated around the crack-tip and J-integrals are computed for all of these contours. The first contour is very close to the tip and may represent erroneous results. Therefore, the J-integral values for the first contour are ignored on account of inaccuracy (ANSYS, 2014b).

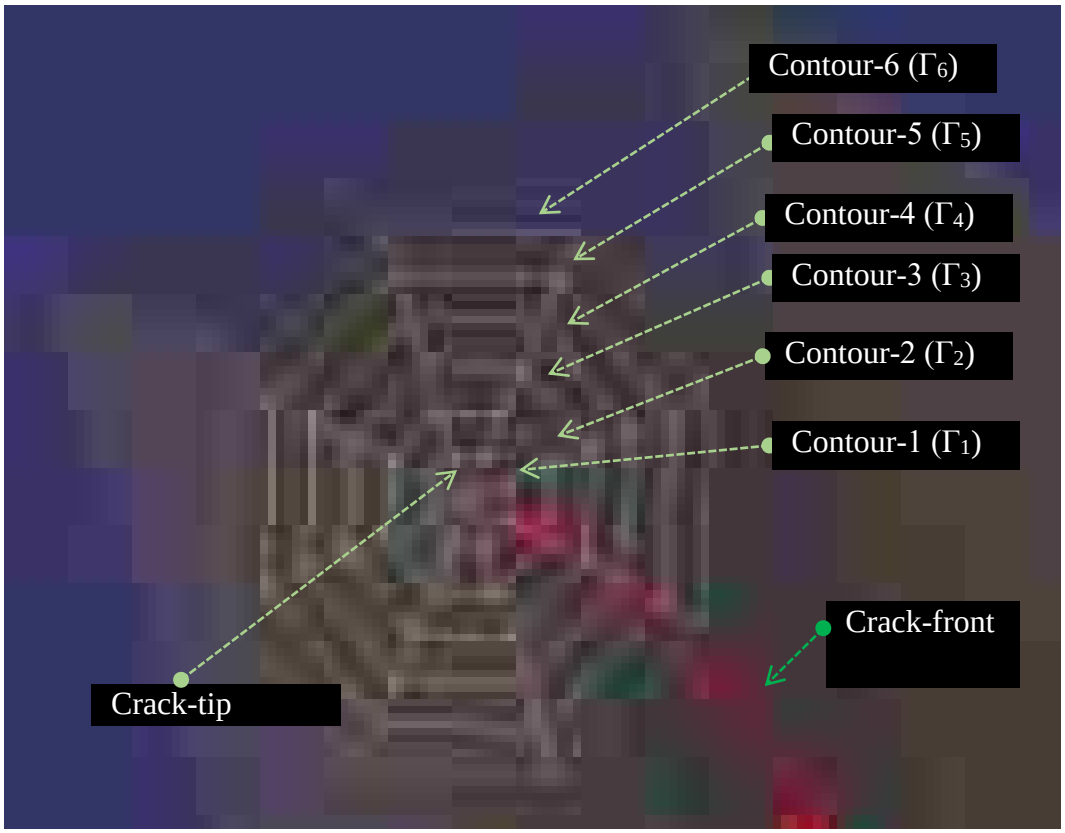

Figure 7.17. Integral contours in ANSYS for J-integral computations

SIFs are computed, using plane stress conditions for all the contours and an average value of five contours (contour 2 to 6) is used for further fatigue analysis. SIFs are computed, for all the cracks at the selected locations as identified in Figure 6.1. Crack lengths are incremented from a smaller to a larger crack size at these selected locations

and SIFs are computed for each of the crack-size. The results are later used to generate the crack-growth curves and for life-expectancy of dipper components.

The following descriptive nomenclature is used for the cracks at the selected locations of dipper-teeth assembly and is shown in Figure 7.18. These locations are selected to have a thorough understanding of the SIF variation with crack length for the side-wall, bottom-plate, and corner tooth.

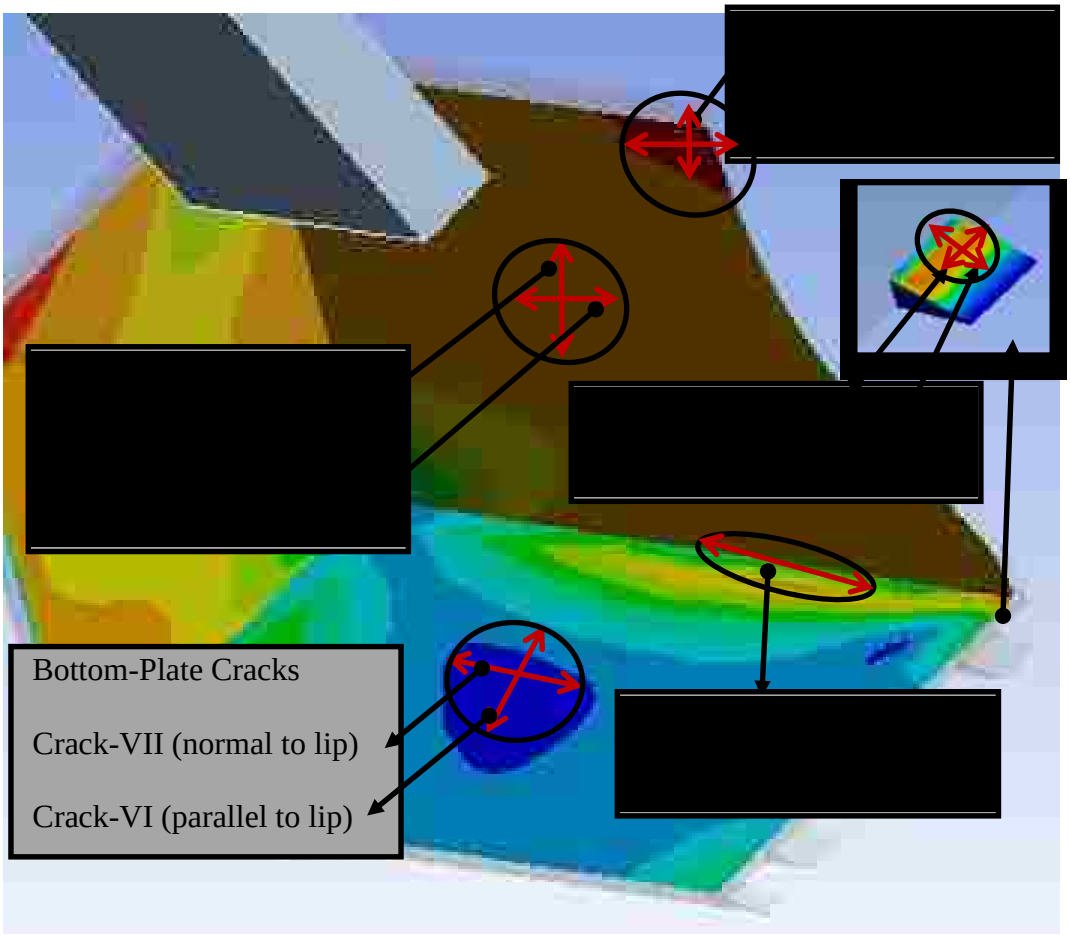

Figure 7.18. Crack numbering scheme

Two orthogonal directions are selected to model the crack orientation impact on SIF. For the bottom-plate the stress is minimum at the center and increases towards the back and side plates. It is at its maximum closer to the side-wall plate. The cracks are modeled at the center and at the maximum stress location. These two selected locations cover the full range of stress and orientation. Similarly, for the side-wall the crack locations are set at the center and at the high stress region. Cracks are designed in two orthogonal orientations. The stress profile for the teeth is very low. However, teeth are one important component of the dipper-teeth assembly. Therefore, two orthogonal directions are selected on teeth for completeness purpose.

The SIF variation curves, at each crack-tip, are obtained through a least square regression and curve fitting process. These variation curves for the simulated cracks at the center and at the top-corner locations of side-wall are shown Figure 7.19. The corner cracks (I and II) represent a higher and steeper increase in the SIFs as compared with the SIFs of cracks at the center of side-wall (cracks III and IV). This is because of the higher stress concentration at the corner locations. Further, both the vertical cracks show higher values than the horizontal cracks, indicating faster propagation rates for the vertical cracks. The SIFs are computed for the mean cases of C_o and material density only.

The SIF variation equations at the crack-tips, at selected locations, are given as equations (7.5) through (7.8).

$$SIF = 7.23E\text{-}04a^3 - 1.06E\text{-}01a^2 + 5.17a + 2.66E + 01 \quad (7.5)$$

$$SIF = 3.17E\text{-}04a^3 - 5.53E\text{-}2a^2 + 3.46E + 00a + 2.61E + 01 \quad (7.6)$$

$$SIF = 4.04E\text{-}04a^3 - 6.32E\text{-}02a^2 + 3.57E + 00a + 2.25E + 01 \quad (7.7)$$

$$SIF = 3.31E\text{-}04a^3 - 5.21E\text{-}02a^2 + 2.99E + 00a + 1.85E + 01 \quad (7.8)$$

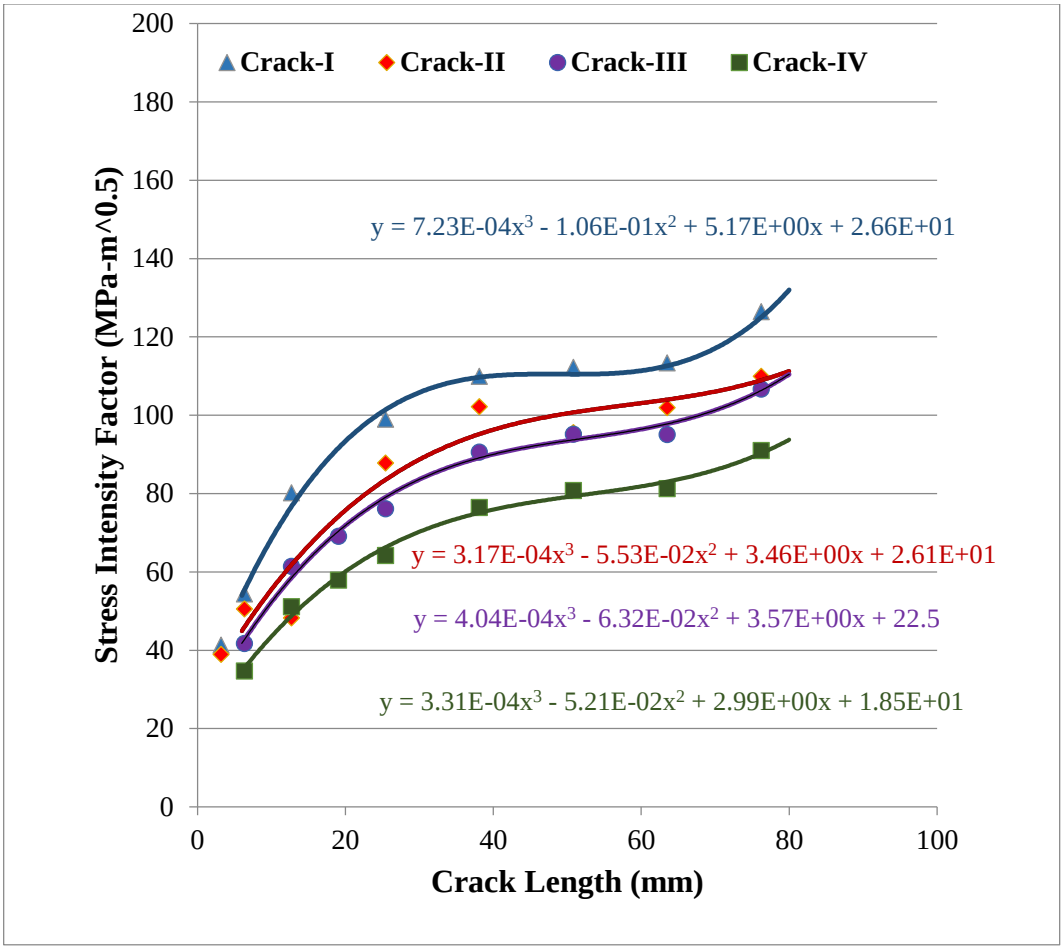

Figure 7.19. Stress intensity factors for side-wall crack-tips

The SIF variation curves for the bottom-plate crack-tips (V, VI and VII) are also obtained through a least square regression and curve fitting process and are plotted in Figure 7.20. The crack-V (at the bottom-plate side) is in a high stress region. Therefore, the SIFs are very high at crack-tips there. Further, the SIFs show a steep increase with crack size. It is expected that the cracks at this location will propagate rapidly. The SIFs for the two orthogonal crack-tips (VI and VII) are relatively lower than the SIFs of crack-V. However, out of the two cracks, the crack-VI (parallel to the dipper cutting lip) has higher SIFs, suggesting that these cracks will propagate faster than the crack-VII (normal

to the dipper lip). The corresponding SIF variation equations for all three cracks are given in equations (7.9) through (7.11).

$$SIF = 4.98E\text{-}04a^3 - 8.75E\text{-}02a^2 + 5.14a + 2.96E + 01 \quad (7.9)$$

$$SIF = 7.28E\text{-}04a^3 - 1.67E\text{-}2a^2 + 1.31E + 00a + 1.43E + 01 \quad (7.10)$$

$$SIF = 9.71E\text{-}05a^3 - 1.98E\text{-}02a^2 + 1.29E + 00a + 1.06E + 01 \quad (7.11)$$

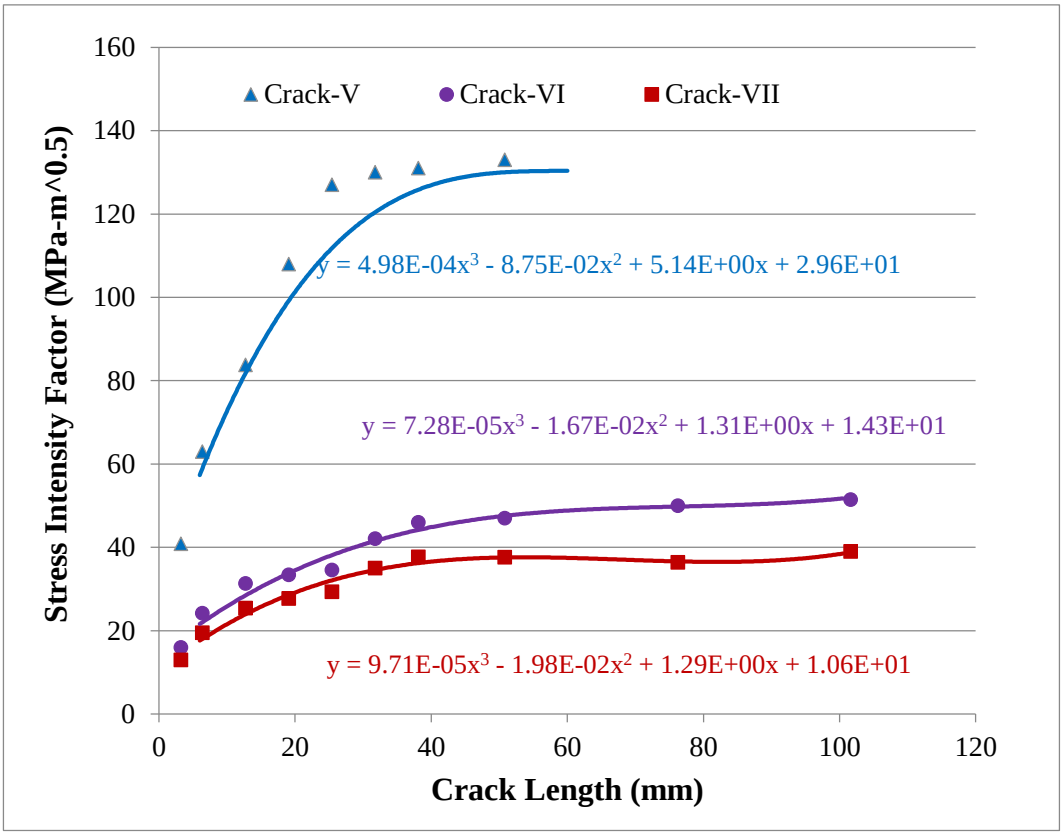

Figure 7.20. Stress intensity factors for the bottom-plate crack-tips

Two orthogonal cracks (VIII and IX) are simulated on the face of corner tooth. Crack-VIII is across the tooth while crack-IX is along the tooth direction. For this research, only cutting resistance forces for a well blasted material are imposed onto teeth.

These forces are smaller than the payload and dipper weight forces, and so are stresses on teeth. As a result, the SIFs for both these cracks are smaller than SIFs for crack-tips significantly large and can cause the SIFs to be quite high. The SIFs at the crack-tips for on dipper body. However, it must be noted that the impact forces on the teeth could be two orientations are shown in Figure 7.21. The crack-VIII shows higher SIFs than the crack-IX suggesting a comparatively higher crack growth rate for the crack-VIII. The corresponding SIF variation equations, obtained through a least square curve fitting process, are given as equations (7.12) and (7.13).

$$SIF = 1.17E\text{-}03a^3 - 1.06E\text{-}01a^2 + 3.19a + 8.97E + 00 \quad (7.12)$$

$$SIF = 4.88E\text{-}054a^3 - 1.55E\text{-}3a^2 + 2.25E\text{-}01a + 6.16E + 00 \quad (7.13)$$

7.3.2. Crack Propagation Curves. The fatigue crack propagation can be (‘c’ and ‘m’) are very important fatigue parameters and must be measured in laboratory modeled by integrating the Paris’ Law (Paris et al., 1961) given as equation (2.15). The equation has three important input parameters (c, m, and ΔK). The two material constants settings following the standard procedures. For common materials the values for these variables can also be found in literature such as Chapra and Canale (1985); Rolfe and Barson (1977). The ‘c’ values generally are between 3 and 4. Throop and Miller (1970) lists some ‘m’ values for common metals. For this research the material constants are taken from research conducted by Yin et al. (2007 and 2008). They estimated the crack-growth for the shovel boom cracks and measured the material constants (‘c’ and ‘m’) in laboratory settings following the ASTM standard E1820. For this research, it is assumed that the material properties for the dipper and teeth material are the same as for the steel used for the boom. With these parameters, equation (2.15) takes the form as equation (7.14).

Equation (7.14) involves the computation of ΔK for each value of a_i and a_f using the relationships established in the previous section. As the computations becomes complex, it is numerically solved using Gauss-Legendre quadrature in MATLAB.

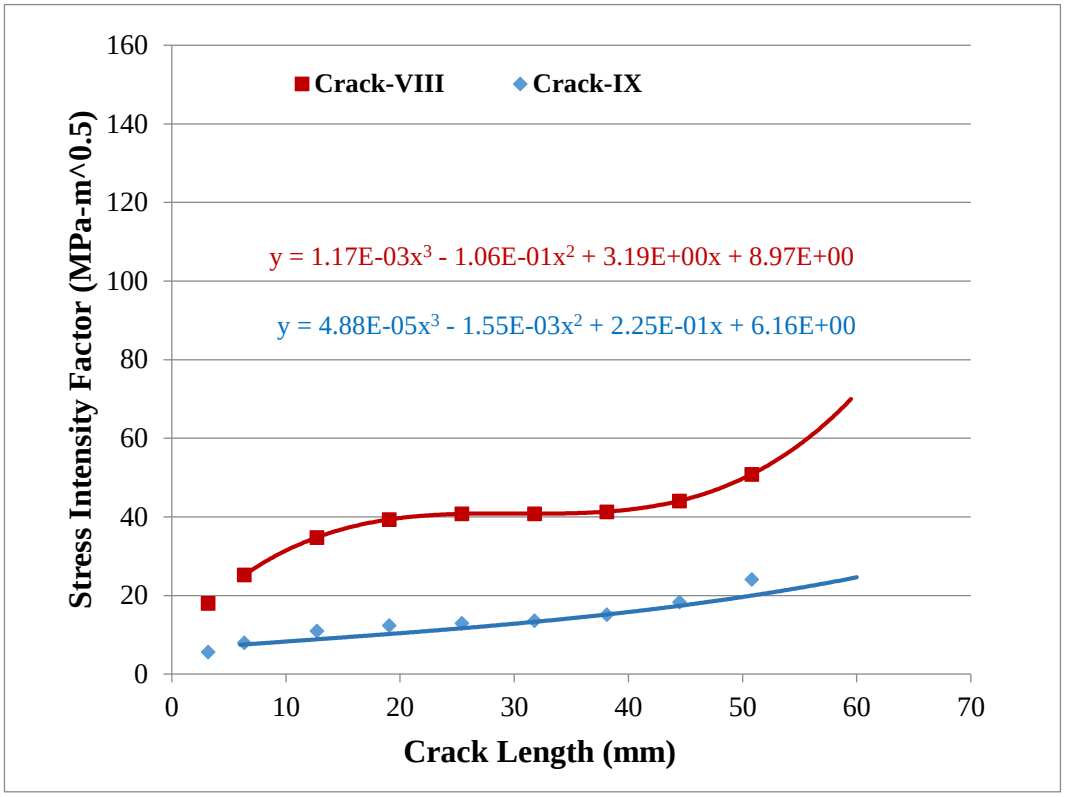

Figure 7.21. Stress intensity factors for the corner-tooth crack-tips

$$N_f = \int_{a_i}^{a_f} \frac{da}{5.89^{-12}(\Delta K)^{3.27}} \tag{7.14}$$

The output from the equation (7.14) include number of cycles (N_f) for a crack to propagate from an initial length (a_i) to a final length (a_f). The number of cycles is not a useful output for shovel digging operation. A more useful parameter for the field

operations is the number of days for crack-propagation, as this can be used to check and set safe maintenance intervals. Therefore, these number of cycles need to be converted into days.

For this purpose, it can be assumed that one digging cycle of shovel is equivalent to one fatigue cycle. Following the Palmgren-Miner's Rule (Miner, 1945) for equivalent damage, the total number of fatigue cycles per day are equal to the digging cycles of the shovel per day. The total numbers of cycles for a shovel per day are counted using the cycle time and the operational efficiency. The digging cycle for shovel is assumed to be 3 seconds for this research, however, a typical complete excavation cycle time for P&H4100XPC is about 30 seconds. The 3 second cycle time is chosen to be consistent with the numerical simulation results.

Using this cycle time and assuming a 95% shovel operational efficiency, the total number of digging cycles for shovel are calculated as 2730 cycles per day. This assumption is very close to field observations recorded by (Yin et al., 2007) where the researchers counted 2880 cycles per day for a cable shovel working continuously over a period of two weeks. For this research a middle-ground value of 2800 cycles per day is assumed to convert the cycles to days.

The SIFs (K1) variations at the crack tips are not uniform. For crack-I to crack-V the SIFs increase rapidly, while for the rest of the dipper crack tips, the SIFs are quite low. The SIF variations for the dipper tooth cracks are even lower. The crack growth is governed by the SIF values. The crack growth curves are grouped together based on their growth rates. Crack propagation curves for the crack-I to V are drawn in Figure 7.22. The crack-V shows the highest propagation rate, while the crack-IV shows the slowest. The

crack propagation curves for the cracks VI and VII are shown in Figure 7.23 and for teeth cracks VIII and IX are shown in Figure 7.24.

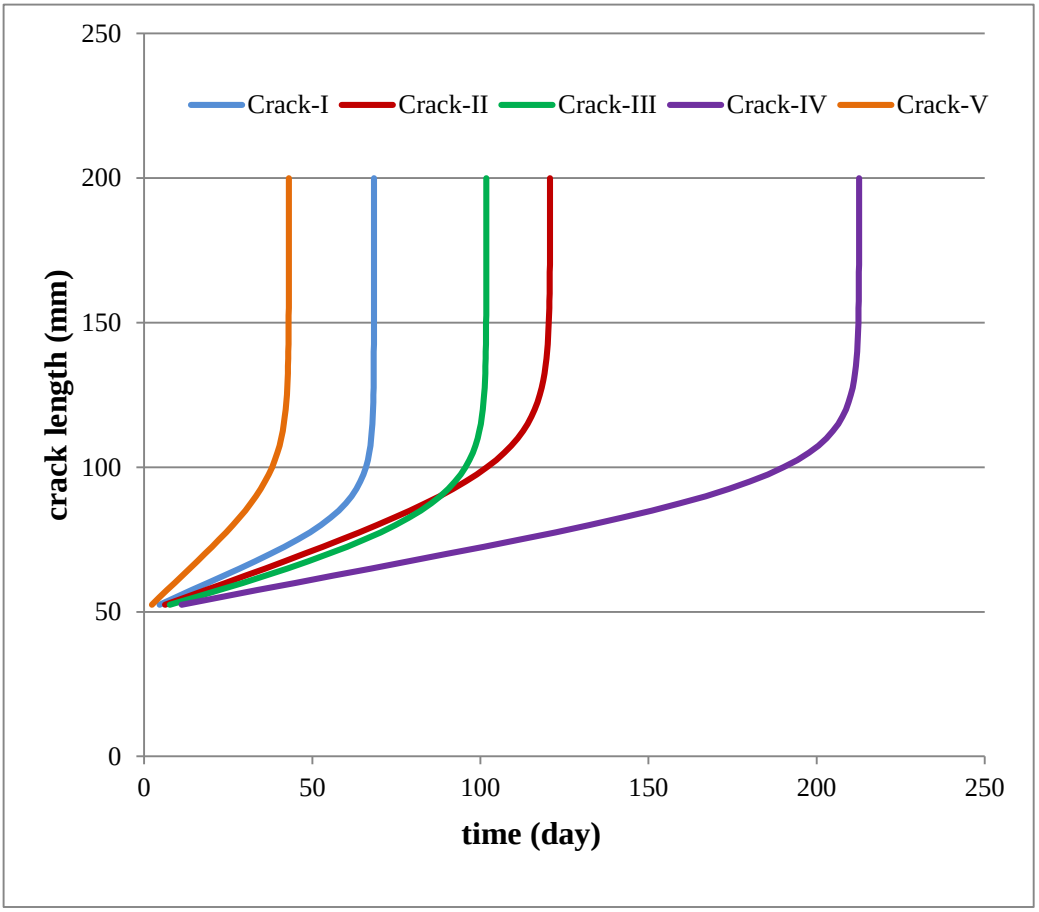

Figure 7.22. Crack propagation curves for the cracks I to V

The crack-V shows the highest crack growth rate. This is expected, as the crack is in the high stress region and is slected along the stress contour (Figure 7.18). The crack-I is also at a high stress region, however, that region is smaller as compared with the region for crack-V. the vertical cracks (I and III) show higher propagation rates as compared with their horizontal counter parts (cracks II and IV). The crack-IV, being

horizontal and at a low stress region shows the least propagation of the five cracks. Two important deductions can be made from these cracks. First, the cracks in the high stress region have higher propagation rates. Second, the vertical cracks in the side-wall have higher propagation rates than the horizontal cracks.

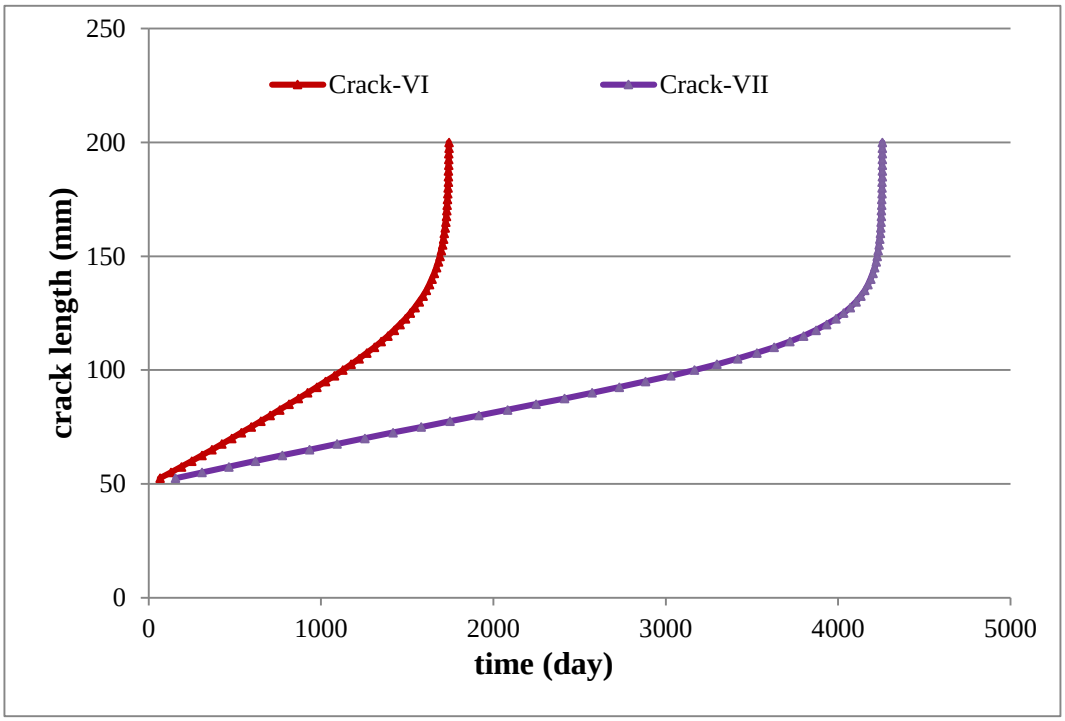

Figure 7.23. Crack growth curves for the crack-VI and VII

The crack propagation curves for the bottom plate central cracks (VI and VII) are shown in Figure 7.23. These cracks are modeled in a low stress region and, as a result, have very slow propagatio rates.

The crack propagation curves for the tooth-cracks (VIII and IX) are shown in Figure 7.24. The stress levels for teeth are very low. Therefore, the crack propagation

rates for teeth are very low as well. Out of these two cracks, the crack across the tooth has a higher propagation rate.

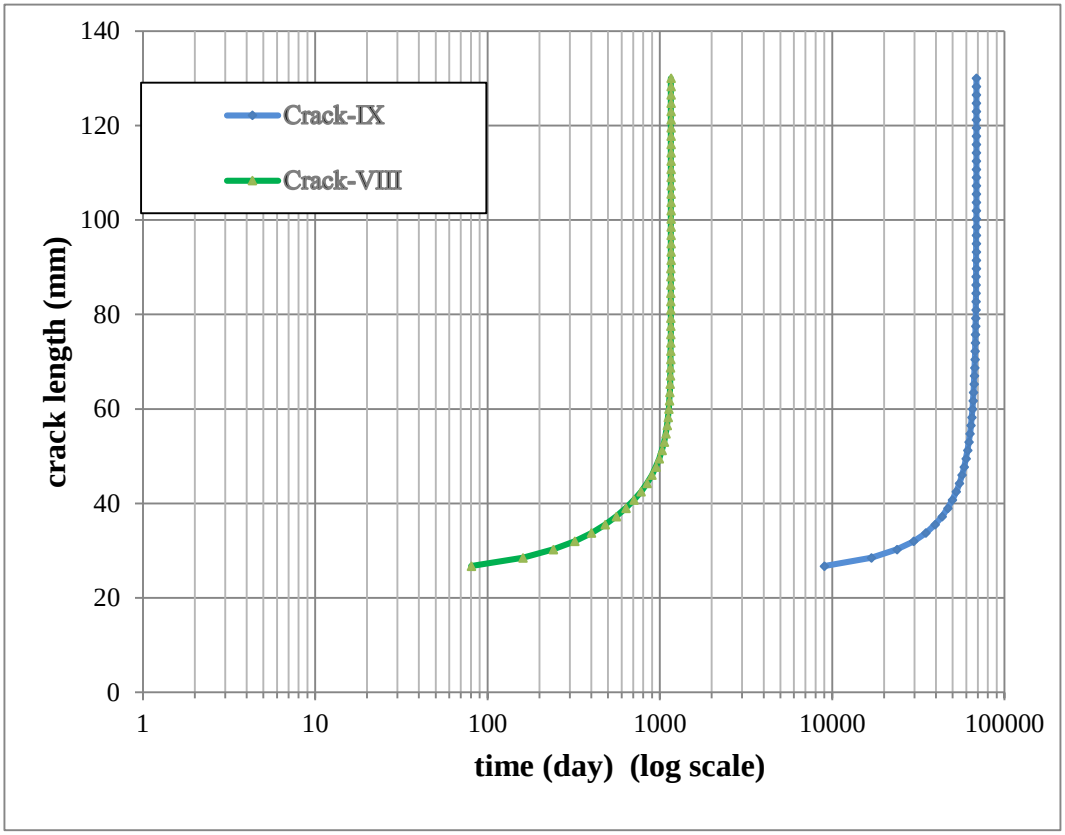

Figure 7.24. Crack growth curves for the teeth cracks VIII and IX

7.3.3. Remaining Life Expectancy of Dipper Components. The remaning useful life for the cracked components can be estimated, with a knowledge of critical crack lengths for dipper material. The critical crack-length is the length of the crack at which the material at the crack-tip starts behaving like a plastic material and the crack propagation becomes very rapid. It is represented as the boundary between the second and third zones for a fatigue crack as shown in Figure 2.2. The critical lengths for metals

are geneally measured using laboratory fatigue toughness tests following the standard procedures. A crtical length limit may also be implemented based on field operating conditions or using the crack-growth curves.

A maximum crack-length or crack-growth rate can be implemented for a shovel component in the field. This maximum crack-length limit could be based on the available crack measurement instrument or technique during the scheduled maintenance. Similarly, a maximum limit on crack propagation rate can be set based on the scheduled maintenance interval. This will ensure that no crack grows to a critical limit before the next scheduled maintenance. (Yin et al., 2007 and 2008) used a field limit of 4.0mm/day leading to a 204 mm crack length for a boom crack operating in oil-sands formations.

The crack growth curves for the dipper cracks are shown in Figure 7.22 through Figure 7.24. It is observed that the crack propagation rates become very high after a certain crack-length. A critical crack length limit can be set based on these propagation rates. For cracks I to V this critical length[1] may be set at around 100-mm length (Figure 7.25). A similar procedure can be adopted to set a limit for the cracks VI to IX. However, the crack propagation for these cracks is very slow and will take a very long time to reach to the critical lengths. These cracks can be considered as “benign” or non-critical cracks, for practical life expectancy purposes. Crack growth curves are more influenced by the initial crack length (a_i) than the final crack length (a_f). The estimated life for cracks, with initial crack of 50mm, is plotted on the Figure 7.25. The crack growth curves are not linear and the crack grows rapidly as the crack get longer. As illustrated in this figure, the

[1] Crack length in this text (and in literature) is always referred as half of the total length of crack. A critical length of 100 mm would be 200 mm total length of the crack.

estimated life for a 50mm crack (crack-V) is 38 days. However, once the crack grows to 75mm, the remaining life is 16 days only for the same crack.

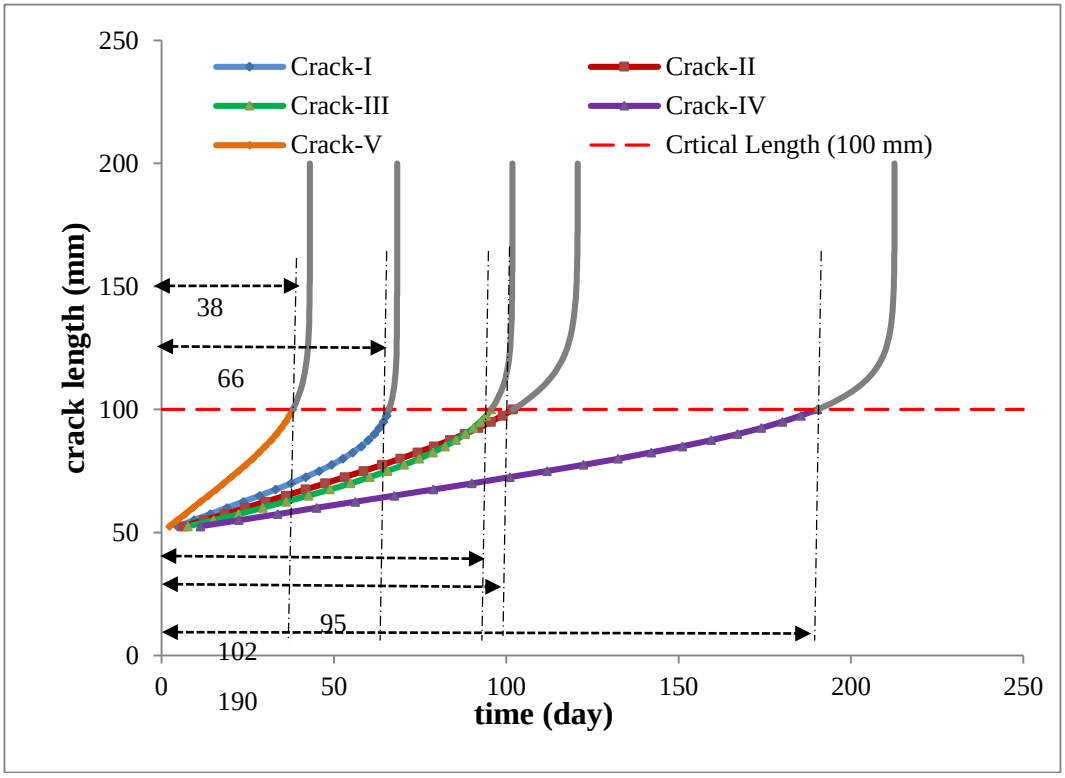

Figure 7.25. Critical crack length and remaining life expectancy for cracks withinitial length of 50mm

The crack propagation and life expectancy results show a similar trend as recorded by Yin et al., (2008) for the shovel boom. That are the only available published results, to the knowledge of author, on fatigue failure and life expectancy modeling related to shovel. The shovel stress loading profile is not reported in that report to compare the stresses. The researchers also found the SIF to have a cubic relationship with crack length as are modeled in this research. Frimpong & Li (2007) measured a maximum node stress

of 10.61 GPA on a shovel boom. The maximum dipper stress loading of the shovel boom. The maximum stresses on the dipper-teeth assembly are measured to be 282 MPa. The stresses on the boom must be greater than the dipper-teeth assembly as the dipper, payload, rigging, and crowd-arm weight all add to the stresses on the boom but not to the stresses on dipper-teeth assembly.

7.4. IMPORTANCE OF RESULTS ON SHOVEL PRACTICE

The results obtained in this section are very important and has a significant impact on shovel manufacturing and operations practices. These results are useful to enhance the shovel health and longevity by increasing the shovel reliability, maintainability, and availability. The results are critical to generate an optimized plan for shovel predictive and preventive maintenance.

7.4.1. Impact of Results on Shovel Operations. Shovel excavation is the center point of mining excavation operations. The efficiency of a mining operation depends on the efficiency of the shovel operation. Shovel breakdowns are expensive and influence the efficiency of the overall mining operation.

The knowledge of formation resistive forces is a key element for an efficient shovel operation. A shovel can be required to work in varying digging conditions. This variation results in a variation of cutting forces. A shovel must be able to provide the required hoist and crowd forces to overcome these resistive forces. The numerical simulator developed in this research can be used as a quick tool to estimate these forces in varying digging conditions.

This research finds the behavior of these cutting forces during the digging cycle. This knowledge is important for the shovel operators to understand the digging operation

better and can be linked with an operator's efficiency. The material resistive forces acting on a shovel dipper must be minimized during the excavation process. This can, in part, be achieved by selecting a proper bench geometry and dipper speed through the muck pile as these eliminate two of the resistive forces acting on the dipper. The simulator developed in this research can be used to optimize both the shovel operation and operator efficiency by varying the field variables.

The varying material conditions has a significant impact on the shovel stress profile. The research has found that the maximum stresses on the shovel dipper vary directly with the density of the material and the formation resistive forces. These are critical findings for a "healthy" shovel operation. The shovel operation needs to be adjusted for varying density and material conditions to avoid severe stress loading of dipper components. The stresses on the dipper-teeth assembly in dense materials can cross the yield strength limits for low and medium carbon steel, resulting in unscheduled shovel breakdowns.

The research has found that the cracks on the dipper components need to be carefully monitored. Given the huge size of the dipper, and the field operative conditions, it is easy to miss a small crack on the body of a dipper. The current practice of visually tracing the crack can cause unplanned and expensive repairs. This research has found that a 3-inch crack in a high stress region of dipper can reach the critical length in 16 days.

The preventive maintenance plans need to be made in accordance with stress loading conditions of the dipper-teeth assembly. In high stress loading conditions, more sophisticated crack detection and monitoring procedures should be adopted to trace cracks on dipper body. A scheduled preventive maintenance interval should be linked

directly with the crack monitoring procedures to increase the availability and maintainability of shovels.

7.4.2. Impact of Results on Shovel Manufacturing. The results of this research are useful for the manufacturing of next generation of dippers and shovels.

The research has found a direct link of shovel stress loading with the formation density and cutting resistance. Shovel dippers need to be manufactured in accordance with the operating conditions. For example, a successful shovel design for coal mining operation might fail for excavating taconite ore because of excessive resistive forces and higher density. Vice versa, the shovel dipper over design can be avoided for lighter digging and formation density conditions.

The research has found that crack propagation has directional preference i.e. the cracks grow rapidly in one direction than the other. This is an important research finding as the material anisotropy might be a parameter to restrict the crack growth in one particular direction. Further investigation is required to test this possibility.

Reliability of a machine is measured by its weakest link in the system. The dipper-teeth assembly consists of a number of smaller components e.g. small links, adapter, rivets, bolts, nuts. The stress variation with density and cutting force is an important finding to improve the reliability of smaller parts and components of the dipper mechanism.

7.5. SUMMARY OF RESULTS

The section details the important results obtained through numerical simulation virtual prototyping for P&H4100XPC shovel. The numerical simulation results show that the peak resistive forces act on the shovel at around 2.5 second of a 3-second simulation

time. This is the time when the shovel dipper-arm is fully extended and is horizontal. Similarly, the hoist torque is at its maximum at this instant of excavation as well.

The shovel stress profile is significantly dependent upon the material density variations. The material density variation controls the dipper payload, which is the most significant of resistive force. The stress profiles show a cubic relationship between maximum stress and material density for dipper side-wall and bottom plates. The relationship is linear for dipper teeth. The stress profile variations are positively skewed for density variation. The resistance model constant "Co" shows a linear relationship with maximum stress for the dipper teeth assembly. Co has a more profound impact on the teeth stress profile.

The SIFs vary cubically with the crack-lengths for the simulated cracks at the selected locations. SIFs for vertical cracks is significantly higher than the horizontal cracks in the side-wall. This suggests that the vertical cracks grow at a higher rate than the horizontal cracks and in any other direction. The SIFs at the bottom-plate side crack (which is at a high stress region) are very high. The crack-propagation curves are plotted using these SIFs and suggest that the cracks in the side-wall and the cracks at the high stress region of bottom-plate have high propagation rates. These cracks become critical at about 100mm length. A 50mm crack in the bottom plate will grow to critical length in 38 days, while a 75mm crack in the bottom-plate will grow to critical length in only 16 days. The cracks in the middle of bottom-plate and in the teeth have very long propagation times and can be considered benign for life expectancy purposes. For teeth, however, the impact forces can be very high and are not modeled for this research. These high impact forces can cause the SIFs to be very large leading to rapid crack propagations.

8. CONCLUSIONS AND RECOMMENDATIONS

8.1. SUMMARY

P&H 4100XPC shovel has 100+ tons per scoop of loading capacity (Caterpillar, 2012; P&H Mining, 2011). The 100+ tons payload, combined with the dipper weight and formation resistive forces, results in varying stress loading of the dipper-and-tooth assembly. Cracks get initiated on the dipper-teeth assembly due to internal flaws or harsh excavation conditions. The high stresses on a shovel can cause these cracks to propagate to critical lengths resulting in fatigue failure of dipper components. Majority of the shovel downtime is dipper related. Roy et al. (2001) reported the dipper related problems to be the most frequent and the second largest contributor for shovel breakdown times.

A kinematic and dynamic model of the shovel front-end is built for this research using the Newton-Euler iterative algorithm. The dynamic model incorporates the formation resistive and the payload forces. The forces are iteratively computed from the dipper-tip to the joint at the saddle block. A numerical simulator is designed in MATLAB/Simulink to solve the kinematic and dynamic model of the front-end assembly.

A virtual prototype for P&H 4100XPC shovel is built in ANSYS (R15) software. The resistive force functions (created from numerical simulation process) and the desired trajectory functions are used as inputs for this virtual prototype. The prototype is used to analyze the stress loading of the dipper-teeth assembly in varying density and digging conditions. Pre-defined cracks are simulated in the dipper-teeth assembly at selected locations and the crack propagation curves are generated. These crack propagation curves are used to estimate the life of dipper components.

8.2. CONCLUSIONS

All the stated research objectives, detailed in Section 1.4, are achieved within the study scope. Appropriate kinematic and dynamic models have been built for the shovel front-end assembly. The dynamic model includes the dynamic forces, including the dynamic payload force. The dynamic gravity center for the dipper payload is also established. A numerical simulation model is developed to solve the kinematic and dynamic models. A virtual prototype is created and the simulations are performed for the shovel dipper stress and fatigue crack analysis. The fatigue life for the dipper-teeth assembly is modeled, based on the stress profile of the dipper-teeth assembly in varying operating environments.

A kinematic and dynamic model of the shovel front-end assembly is developed for this research. The model is built using the Newton-Euler's iterative algorithm. The dynamic model computes the crowd force and hoist torque requirements to overcome the resistive forces. Previous models developed by Hendricks et al., (1993), Daneshmend et al., (193), Frimpong et al., (2005) either ignored the dynamic payload force or assumed this force at the tip of the teeth. Awuah-Offei et al., (2009) included the dynamic payload force in their model. The model used vector loop equations, where these vector loops do not necessarily represent the shovel components. Also the model does not provide information for individual links and joints. The dynamic model developed for this research is unique in the sense as it not only incorporates the dynamic payload and dipper weight forces, but also provides information (position, velocity, acceleration, and force) for the individual links and joints of the shovel dipper-teeth assembly. The model also includes the formation excavation resistive forces.

A numerical simulator is developed in MATLAB/Simulink environment to solve the kinematic and dynamic models. This simulation model calculates the positions, velocities, accelerations, forces, and torques for the shovel joints and links of dipper-teeth assembly. The simulator can be used to analyze the crowd-force and hoist requirements in varying digging environments for multiple dipper dimension and bench geometries. The flexibility of the simulator stems from the fact that it consists of sub-models, coded as separate MATLAB files, to quickly alter the input parameters. The following specific conclusions can be drawn from the numerical simulation of dynamic model:

1. Payload is the most significant resistive force for larger shovels like P&H 4100XPC.
2. Maximum cutting resistive forces act when the dipper is fully extended into the bench and the crowd-arm is nearly horizontal with the bench.
3. Maximum hoist-torque is required when the dipper is at the position described in 3.

A virtual P&H 4100 XPC shovel prototype has been constructed in AutoCAD and ANSYS Workbench (R15). This virtual prototype is used for stress profiling of dipper-teeth assembly. From the detailed stress analysis of dipper, the following conclusions can be drawn:

1. The payload is the dominant resistive force for stress loading of the dipper.
2. The equivalent (von-Mises) stresses are maximum at the dipper side-wall.
3. The dipper teeth have a very low stress profile in the dipper-teeth assembly.
4. The dipper stress profile varies directly with the density of the material. For the side-wall and the bottom-plate this variation is cubic, while for the dipper teeth, the variation is linear.

5. The maximum stresses on the dipper side-wall, bottom-plate, and teeth all vary linearly with the parameter “Co” of Zelenin et al. (1985) resistive force model.
6. The parameter “Co” has more impact on the stress profile for the teeth and lesser for the dipper body.
7. The maximum equivalent (von-Mises) stress values on dipper components, when digging dense materials, is above the lower yield strength limits for low and medium carbon steels.

The virtual prototype is also used for fatigue analysis and life-expectancy of dipper-teeth assembly. For this purpose, representative cracks are modeled at the selected locations of dipper side and bottom plates, and on corner tooth. The J-integrals are computed for each crack-tip to calculate stress intensity factors (SIFs). These cracks are incremented in small step sizes and the resulting SIFs are computed for each increment. The following specific conclusions can be drawn from the fatigue fracture analysis of the dipper-teeth assembly:

1. The SIFs have cubic relationship with the crack lengths
2. SIFs are dependent on the local stresses and crack orientations.
3. The side-wall cracks have higher crack-propagation rates than most of the cracks in other locations. Only the crack in the high stressed region of the bottom-plate has a higher propagation rate than these side-wall cracks.
4. Vertical cracks on the side-walls have higher growth rates than the horizontal cracks at the same location.
5. The crack propagation rates for the cracks in the bottom-plate and the teeth are very slow.

6. A 100 mm crack becomes critical for the dipper components. At 100mm the crack propagation rates become very high and material can be unstable.
7. Crack propagation rates are dependent upon initial crack length.
8. A 75mm (3-inch) crack, on dipper bottom-plate, can grow to critical length in about 16 days.

8.3. RESEARCH CONTRIBUTIONS

All the stated objectives of the research are achieved for this research. The following are the major contributions of this research:

1. A detailed kinematic and dynamic model of the cable shovel front-end has been built using Newton-Euler algorithms. The models incorporate the dynamic forces of payload and dipper weight. The dynamic point of application of these forces is also determined. The model is an improvement on the existing models as it incorporates the dynamic forces including the dynamic payload force.

2. A numerical simulator has been developed to solve the kinematic and dynamic model of shovel front-end. The simulator gives detailed information on positions, velocities, accelerations, and forces for individual links and joints during the digging cycle. This simulator is an improvement over the existing numerical simulators as it incorporates the dynamic payload force and provides a detailed information (position, velocity, acceleration, and force) on the individual links and joints. This simulator can be used as a quick way to measure the performance of shovel and operator in varying digging, and operating conditions.

3. A frame work for dipper stress profiling is proposed. This is the first ever attempt to model the stress profile of shovel dipper-teeth assembly. As a result of this

research, the critical high stressed regions of the dipper are identified. It is found that the dipper side-walls, and the areas of the bottom-plate closer to the side-wall, are the severely stressed regions.

4. This research is the first effort to establish a relationship between maximum stress and formation density for dipper-teeth assembly. The research established that maximum stresses vary cubically for the dipper side-wall and the bottom-plate, and linearly for the teeth with variation in formation density.

5. Similarly, the research found out that the maximum stress for dipper components vary linearly with Zelenin et al. (1985) "C_o" cutting force parameter. This parameter is the only formation related parameter in the cutting force model.

6. The research established relationship between the SIFs and the crack-length for cracks at various locations and in different orientations.

7. The research has developed the crack propagation rates for semi-elliptical cracks at various locations, and in orthogonal directions, for dipper components. This is a pioneer effort to have any information on crack-propagation rates for dipper components.

The research has found that a 100 mm crack can be considered as a critical crack-length for the dipper-teeth assembly. It is expected that this information, along with the crack propagation rates information, will help in establishing a crack detection and monitoring system for field shovel operations.

8.4. RECOMMENDATIONS

The dynamic simulator developed in this research can be used as a tool for the field engineers, shovel supervisors and operators for efficient shovel utilization. The force

and torque requirements for a shovel can be computed, fairly quickly, in various digging conditions. The results can be used to optimize the shovel performance for different bench geometries. Similarly, the impact of blast patterns and variations in the material properties can be quickly analyzed before introducing a shovel in unknown conditions.

The following could significantly improve the research in this area. Due to the proprietary concerns the virtual prototype is not based on the actual CAD model of the P&H4100 shovel. The details of the model could have significant impact on the stress modeling and analysis of shovel to increase the reliability of the front-end assembly. The design modifications can only be suggested if the actual model is available for research and comparisons. Similarly, the fatigue parameters (C, m, and fracture toughness) need to be measured in the laboratory settings for dipper-teeth components.

The dynamic model presented in this research, makes some simplifying assumptions on dipper trajectory and resistive force models. The existing resistive force models do not fully explain the dipper excavation for large dippers and also are not validated with field measurements. The impact forces on the dipper teeth are generally ignored in resistive models. These forces can be very large and should be part of a resistive force model. In the absence of such a detailed model, the exiting performance monitoring systems installed on shovels can be modified to estimate these forces. Modern shovels estimate the shovel performance using hoist motor voltage and armature current. This information can be used to estimate the shovel breakout forces in real-time and as an input to the simulator. The numerical simulator output then can be used as a feedback mechanism, to improve the shovel performance.

A detailed crack monitoring scheme needs to be adopted for field operations to validate the results of this research. Crack propagation rates vary with location, size and

orientation e.g. a 3-inch, vertical, corner crack has a higher propagation rate than a 3-inch crack at the middle of side plate. A knowledge of the stress profile of the shovel dipper-teeth assembly and the crack-propagation rates to the operators and supervisors can help minimize the breakdown times of shovels.

8.5. FUTURE RESEARCH

The crack propagation and life-expectancy models presented in this research require a close field monitoring for validation purposes. The monitoring scheme must be designed to make a complete record of crack-lengths, crack-depths, crack-locations, crack-orientations, and propagation rates. The crack-depth should be measured with a sophisticated instruments e.g. lasers, x-rays. The crack propagation must be recorded to compare the results with this research.

The framework developed in this research for shovel stress profiling and fatigue studies can be used to create a complete fatigue crack profile of the dipper-teeth assembly. The whole dipper-teeth assembly can be subdivided into regions with similar SIFs and crack-propagation rates. This information will help develop a “crack-propagation clock” (as developed by Yin et al., (2008) for a shovel boom) for the dipper-teeth assembly.

This research used the resistive force model suggested by Zelenin et. al., (1985). This resistive force model has an improvement potential for the fragmented or blasted rock material, and excavation for larger dippers. The critical C_o parameter of this model can be converted to numbers recorded by standard and modern penetration devices e.g. dynamic cone penetrometer. A new fragmented or blasted material classification can be made for this model.

This research included a force acting on the dipper side-wall. The force is modeled using the passive earth pressure theory. The existing literature on dipper forces does not show this force. The force is present as a hole in the side-wall will make the material to flow-out. The magnitude of this force should be verified using the field measurements.

A real dipper design wasn't available for this research due to propriety reasons. A real dipper-teeth assembly consists of a number of parts (e.g. adaptors, connectors, pulleys, bolts) and mechanisms (e.g. door trip mechanism) which were not included in this research. Design modifications and a complete life expectancy study is only possible if a real dipper design is available for investigation. A complete stress profile of all the dipper components, links, connectors, and door-trip mechanism should be made for a complete stress analysis of the dipper-teeth assembly. These components should also be included for fracture analysis and life-expectancy studies.

The teeth are connected to the dipper body via the adaptors. There can also be a relative movement between the teeth and the adaptor. The relative movement between the teeth and the adaptor can affect the stress profile of the teeth assembly. The stress profile for the adaptor should also be measured and tested for the yield and fracture properties.

The current research did not include the impact of vibrations on dipper-teeth assembly. The assumption can be true as the dipper movement is restricted during the digging trajectory. The vibrations can change the stress profile, especially, when the dipper is cleared off the crest. Further research should include the impact of vibrations on dipper-teeth assembly.

BIBLIOGRAPHY

Alekseeva, T. V., Artem'ev, K. A., Bromberg, A. A., Boitsekhouskii, R. I., & Ul'yanov, N. A. (1985). *Machines for Earthmoving Work, Theory and Calculations*: Amerind Publishing Co. Pvt. Ltd. New Delhi, India.

ANSYS. (2014a). ANSYS WORKBENCH (Version 15): ANSYS Inc.

ANSYS. (2014b). ANSYS Workbench Help Documentation: ANSYS Inc.

ASTM. (1969). Manual on Low Cycle Fatigue Testing *ASTM STP465* American Society of Testing and Materials, PA.

Autocad. (2012). (C) Autodesk Inc.

Awuah-Offei, K. (2005). *Dynamic Modeling of Cable Shovel-Formation Interactions for Efficient Oil Sands Excavation.* (PhD), Missouri S&T, Rolla, MO.

Awuah-Offei, K., & Frimpong, S. (2006). Numerical Simulation of Cable Shovel Resistive Forces in Oil Sands Excavation. *International Journal of Mining, Reclamation and Environment, 21*(1), 223-238.

Awuah-Offei, K., Frimpong, S., & Askari-Nasab, H. (2009). Formation Excavation Resistance Modeling for Shovel Dippers. *International Journal of Mining and Mineral Engineering, 1*(2), 127-146.

Balovnev, V., I. (1983). *New Methods for Calculating Resistance to Cutting of Soil*: Amerind Publishing, New Delhi, India.

Bannantine, J. A., Comer, J. J., & Handrock, J. L. (1989). *Fundamentals of Metal Fatigue*: Prentice Hall, Englewood Cliffs, New Jersey 07632.

Blouin, S., Hemami, A., & Lipsett, M. (2001). Review of Resistive Force Models for Earthmoving Processess. *Journal of Aerospace Engineering, 14*(3), 102-111.

Boccafogli, A., Busatti, G., Gherardi, F., Malaguti, F., & Paoluzzi, R. (1992). Experimental evaluation of cutting dynamic models in soil bin facility. *Journal of Terramechanics, 29*(1), 95-105. doi: http://dx.doi.org/10.1016/0022-4898(92)90017-E.

Caterpillar. (2012). Electric Rope Shovels. 2012, from https://mining.cat.com/products/surface-mining/electric-rope-shovels.

Chapra, S. C., & Canale, R. P. (1985). *Numerical Methods for Engineers: with Personal Coputer Applications*: McGraw-Hill, New York.

Coulomb, C. A. (1776). Essai Sur Une Application Des REgles Des Maximis et Minimis a Quelques Problems de Statique Relatifs a l'architechture. *Academic Royale des Sciences: Memories de Mathmatique et de Physique, presentes a l'Acaemie Royale des Sciences, par Divers Savants, et lus dans les Assemblees, Paris, 7*, 343-382.

Craig, J. J. (1996). *Introduction to Robotics: Mechanics and Control* (2nd ed.): Addison Wesley.

Cundall, P. A., & Strack, O. D. L. (1979). A Discrete Numerical Model for Granular Assemblies. *Géotechnique, 29*(1), 47-65.

Daneshmend, L., Hendricks, C., Wu, S., & Scoble, M. (1993). Design of a Mining Shovel Simulator. *Innovative mine design for the 21st century: Proceedings of the International Ccongress on Mine Design, Ontario, Canada*, 551-561.

Denavit, J., & Hartenberg, R. S. (1955). A Kinematic Notation for Lower-Pair Mechanisms Based on Matricies. *Trans. of ASME. Journal of Applied Mechanics, 22*, 215-221.

Dombrovskii, N. G., & Pankratov, S. A. (1961). *Zemleroinye Mashiny, Ch. 1 Odnokovshovye Ekskavatory (Earthmoving Machines, Part 1 Single-Bucket Shovels)*: Gosstroiizdat, Moscow.

Fowkes, R. S., Frisque, D. E., & Pariseau, W. G. (1973). Materials Handling Research: Penetration of Selected/Granular Materials by Wedgeshaped Tools *Rep. of Investigations 7739*: Bureau of Mines, U.S.D.I.

Frimpong, S., & Hu, Y. (2004). Parametric Simulation of Shovel-Oil Sands Interaction During Excavation. *International Journal of Surface Mining, Reclamation and Environment*, 205-219.

Frimpong, S., & Hu, Y. (2008). Intelligent Cable Shovel Excavation Modeling and Simulation. *International Journal of Geomechanics (c) ASCE, 8*(1), 2-10.

Frimpong, S., Hu, Y., & Awuah-Offei, K. (2005). Mechanics of Cable Shovel-fromation Interactions in Surface Mining Excavations. *Journal of Terramechanics, Elsevier Science Ltd.*, 15-33.

Frimpong, S., & Li, Y. (2007). Stress Loading of the Cable Shovel Boom under in-situ Digging Conditions. *Engineering Failure Analysis, Elsevier Science Ltd., 14*(4), 702-715.

Frimpong, S., Li, Y., & Awuah-Offei, K. (2008). Cable Shovel Health and Longevity and Operator Efficiency in Oil Sands Excavation. *International Journal of Mining and Mineral Engineering, 1*(1), 47-61.

Hemami, A. (1994). An Approximation of the Weight of the Loaded Material During the Scooping Operation of a Mechanical Loader. *Transactions of the Canadian Society of Mechanical Engineering, 18*(3), 191-205.

Hemami, A., & Hassani, F. (2003). *Procedure Design for Experiments Towards Modeling of the Cutting Force in Excavation of Bulk Media*. Paper presented at the 20th International Symposium on Automation and Robotics in Construction ISARC 2003. The Future Site. http://www.irbnet.de/daten/iconda/CIB13314.pdf.

Hendricks, C., Daneshmend, L., Wu, S., & Scoble, M. (1993). Design of a Simulator for Productivity Analysis of Electric Mining Shovels. *Proc. of 2nd International Symposium on Mine Mechanization and Automation, Lulea, Sweden*, 329-336.

Hendricks, C., & Scoble, M. (1990). *Post-Blast Evaluation Through Shovel Performance Monitoring.* Paper presented at the Proceedings of the Conference on Explosive and Blasting Technique, Canada Centre for Mineral and Energy Technology.

Hettiaratchi, D. R. P., & Reece, A. R. (1974). The calculation of passive soil resistance. *Géotechnique, 24*(3), 289-310.

HPC. (2014). High Performance Computing www.hpc.mst.edu. Retrieved 10/29/2014, from hpc.mst.edu.

Irwin, G. R. (1957). Analysis of Stresses and Strains Near the End of a Crack Transversing a Plate. *Trans. A.S.M.E., Journal of Applied Mechanics*, 361-364.

Koivo, A. J. (1989). *Fundamentals for Control of Robotic Manipulators*: Jhon Wiley & Sons, Inc.

Koivo, A. J. (1994). Kinematics of Excavators (Backhoes) for Transferring Surface Material. *Journal of Aerospace Engineering, 7*(1), 17-32.

Koivo, A. J., Thoma, M., Kocaoglan, E., & Andrade-Cetto, J. (1996). Modeling and Control of Excavator Dynamics During Digging Operation. *Journal of Aerospace Engineering, 9*(1), 10-18.

Li, Y., & Frimpong, S. (2008). Hybrid Virtual Prototype for analyzing Cable Shovel Component Stress. *Int Journal of Manufacturing Technology, 37*, 423-430.

Lipsett, M. G., & Moghaddam, Y. R. (2011). *Bifurcations, Instabilities and Degradation in Geomaterials, SSGG*. In R. Wei Wu, Borja. I (Series Ed.) Vol. VIII. W. M. Richard, Alsaleh, Labuz, Joe (Ed.) *Modeling Excavator-Soil Interaction* (pp. 347-366).

Loakimidis, N. I., & Theocaris, P. S. (1978). The Numerical Evaluation of a class of generalized stress intensity factors by use of the Lobatto-Jacobi numerical intergration rule. *Internation Journal of Fracture, 14*, 469-484.

Mak, J., Chen, Y., & Sadek, M. A. (2012). Determining parameters of a discrete element model for soil–tool interaction. *Soil and Tillage Research, 118*(0), 117-122. doi: http://dx.doi.org/10.1016/j.still.2011.10.019.

MathWorks, I. (2012). MATLAB (Version R12): MathWorks Inc.

matweb. (2014). Material Property Dataseet. Retrieved 12/2/2014 http://www.matweb.com/search/QuickText.aspx?SearchText=carbon%20steel.

McKyes, E. (1985). Soil Cutting and Tillage. *Elsevier Science Publishers, New York, USA*, 215.

Miner, M. A. (1945). Cummulative Damage in Fatigue. *Trans. ASME, Journal of Applied Mechanics, 67*.

Mohr, O. (1914). Die Elastizitatsgrenze und Bruch eines Materials. *Z. Ver. Dtsch. Ing., 44*, 1524.

Momozu, M., Oida, A., Yamazaki, M., & Koolen, A. J. (2003). Simulation of Soil Loosening Process by Means of Modified Distinct Element Method. *Journal of Terramechanics, PERGAMON, 39*, 207-220.

Oida, A., & Momozu, M. (2002). Simulation of Soil Behavior and Reaction by Machine Part by Means of DEM. *Agricultural Engineering International: The CIGR Journal of Scientific Research and Development, IV*.

Osman, M. S. (1964). The Mechanics of Soil Cutting Blades. *Journal of Agricultural Engineering Research, 9*(4), 313-328.

P&H. (2012). 4100XPC Electric Mining Shovel. Retrieved Sep, 30, 2012, from http://www.minepro.com/MinePro/Literature/Spec/4100XPC-AC.pdf.

P&H Mining. (2011). Electric Rope Shovels. Retrieved October 23, 2011, 2011, from http://www.phmining.com/en/PHMining/Mining-Equipment/Electric-Shovels.htm.

Paris, P. C., & Erdogan, F. (1963). A Critical Analysis of Crack Propagation Laws. *Trans.* of ASME. Journal of Basic Engineering, D85, 528-534.

Paris, P. C., Gomez, M. P., & Anderson, W. E. (1961). A rational analytic theory of fatigue. *The Trend in Engineering, 13*, 9-14.

parkerbaymining.com. Retrieved September 14, 2012, from http://parkerbaymining.com/mining-equipment/electric-shovels.htm.

Pearson, J. E., Hannen, W. R., & Soderberg, E. (2004). Development of fatigue monitoring system for a hydraulic excavator. *Practice Periodical on Structural Design and Construction, 9*(4), 221-226.

Raju, I. S., & Newman, J. C., Jr. (1997). Three Dimensional Fine-Element Analsysis of Finte-Thickness Fractue Specimens (pp. 42): NASA Langely Research Center; United States.

Reece, A. R. (1965). The Fundamental Equation of Earthmoving Mechanics. *Symposium on Earthmoving Machinery, Institute of Mechanical Engineers, 179*(Part-3F).

Rice, J. R. (1968a). Mathematical Analysis in the Mechanics of Fracture. In H. Liebowitz (Ed.), *Fracture: An Advanced Treatise* (Vol. 2, pp. 191-311): Acedemci Press, NY.

Rice, J. R. (1968b). A Path Independent Integral and the Approximation Analysis of Strain Concentration b Notches and Cracks. *Journal of A;;oied Mechanics. ASME*(35), 379-386.

Rolfe, S. T., & Barson, J. M. (1977). *Fracture and Fatigue Control in Structures*: Prentice-Hall, Englewood Cliffs, NJ.

Rowland, J. C. (1991). *Dragline Bucket Filling.* (PhD), University of Queensland.

Roy, S. K., Bhattacharyya, M. M., & Naikan, V. N. A. (2001). Maintainability and Reliability Analysis of a Fleet of Shovels. *Transactions of The Institution of Mining & Metallurgy*, A163-A171.

SAE. (1968). SAE Fatigue Design Handbook: Society of Automotive Engineers, Warendale, PA.

Seward, D., Bradley, D., & Bracewll, R. (1988). The Development of Research Models *for Automatic Excavation.* Paper presented at the Proc. The 5th International Symposium on Robotics in Construction, Tokyo, Japan.

Sih, G. C. (1973). *Handbook of stress-intensity factors*: Lehigh University, Institute of Fracture and Solid Mechanics.

Sommer III, H. J. (2011). POLYGEOM.m : Geomery of a Planar Polygon. Retrieved from http://www.mathworks.com/matlabcentral/fileexchange/319-polygeom-m.

SSAB. (2009). CSA Structural Steel Plate for Bridges. 2014, from http://www.ssab.com/Global/SSAB/SSAB_Americas/CSA%20Bridge%20Plates%202009%2007%2001.pdf.

Stavropoulou, M., Xiroudakis, G., & Exadaktylos, G. (2013). Analytical Model for Estimation of Digging Forces and Specific Energy of Cable Shovel. *Coupled Systems Mechanics, 2*(1), 23-51.

Swick, W. C., & Perumpral, J. V. (1988). A model for predicting soil-tool interaction. *Journal of Terramechanics, 25*(1), 43-56. doi: http://dx.doi.org/10.1016/0022-4898(88)90061-4.

Syncrude. (1996). At Face Slurrrying: Provisional Data: Syncrude Canada Ltd., Edmonton, Alberta.

Tada, H., Paris, P. C., & Irwin, G. R. (1973). *Stress Analysis of Cracks Handbook*: Del Research Corporation, Hellertown, PA.

Takahashi, H., Hasegawa, M., & Nakano, E. (1999). Analysis on the Resisitive Forces Acting on the Bucket of a Load-Hual-Dump Machine and a Wheel Loader in the Scooping Task. *Advanced Robotics, 13*(2), 97-114.

Tanaka, H., Momozu, M., Oida, A., & Yamazaki, M. (2000). Simulation of Soil Deformation and Resistance at Bar Penetration by the Distinct Element Method. *Journal of Terramechanics, PERGAMON, 37*, 41-56.

Terzaghi, K. (1943). *Theoretical Soil Mechanics*: John Wiley and Sons, New York, USA.

Thakur, T. C., & Godwin, R. J. (1990). The Mechanics of Soil Cutting by a Rotating Wire. *Journal of Terramechanics, Elsevier Science Ltd., 24*(7), 295-305.

Throop, J. F., & Miller, G. A. (1970). Optimum Fatigue Crack Resistance *Acheivment of High Fatigue Resistance in Metals and Alloys, ASTM STP 467*: Acmerican Society for Testing and Materials, Philadelphia.

Ting, J. M., Corkum, B. T., Kauffman, C. R., & Greco, C. (1989). Discrete Numerical Model for Soil Mechanics. *Journal of Geotechnical Engineering, 115*(3), 379-398.

Vaha, P. K., & Skibniewsky, M. J. (1993). Dynamic Model of Excavator. *Journal of Aerospace Engineering, 6*(2), 148-158.

Wilkinson, A., & DeGennaro, A. (2007). Digging and Pushing Lunar Regolith: Clasical Soil Mechanics and the Forces Needed for Excvation and Traction. *Journal of Terramechanics, 44*, 133-152.

Wu, H. (1995). *Modeling and Simulation of Electric Mining Shovels.* (PhD Theises), McGill University, Montreal, Quebec, Canada.

Yin, Y., Grondin, G. Y., Obaia, K. H., & Elwi, A. E. (2007). Fatigue life prediction of heavy mining equipment. Part 1: Fatigue load assessment and crack growth rate tests. *Journal of Constructional Steel Research, 63*(11), 1494-1505. doi: http://dx.doi.org/10.1016/j.jcsr.2007.01.008.

Yin, Y., Grondin, G. Y., Obaia, K. H., & Elwi, A. E. (2008). Fatigue life prediction of heavy mining equipment. Part 2: Behaviour of corner crack in steel welded box section and remaining fatigue life determination. *Journal of Constructional Steel Research, 64*(1), 62-71. doi: http://dx.doi.org/10.1016/j.jcsr.2007.04.003.

Yong, R. N., & Hanna, A. W. (1977). Finite Element Analysis of Plane Soil Cutting. *Journal of Terramechanics, 14*(3), 103-125.

Zelenin, A. N., Balovnev, V. I., & Kerov, I. P. (1985). *Machines for Moving the Earth*: Amerind Publishing New Delhi, India.

VITA

Muhammad Azeem Raza was born in Pakistan. He attended the University of Engineering and Technology (UET), Lahore, Pakistan from 1995 to 2000 for his BSc mining engineering degree. He received his MSc mining engineering and MSc computer science degrees from UET in 2006 and 2005 respectively. He joined the Department of Mining Engineering at UET, Lahore in 2004 as a lecturer and later was promoted to Assistant Professor in 2008. In August 2008, he moved to Missouri University of Science and Technology (S&T), Rolla, MO for his PhD studies in Mining Engineering, under the supervision of Dr. Samuel Frimpong.

In 2011, he did a summer internship at Gillete WY, for Peabody Energy (Inc.). He served as the elected president for council of graduate students (CGS) at S&T for the term 2011-2012. In 2012, he joined Michigan Technological University as an instructor for mining engineering. He also served as a course instructor and teaching assistant at Missouri S&T for multiple courses. He won the department outstanding teaching award in 2012. He also won the SME Syd. Peng Ground Control Award in 2012. He received his PhD mining engineering in May 2016.